NTNU
Norwegian University of
Science and Technology

Master's thesis

2020

Andreas Djupesland

Master's thesis

NTNU
Norwegian University of
Science and Technology
Faculty of Engineering
Department of Energy and Process Engineering

Andreas Djupesland

Numerical study of unsteady flow in slits and investigation of methods to reduce pressure pulsations in pipes

June 2020

NTNU
Norwegian University of
Science and Technology

NTNU
Norwegian University of
Science and Technology

Numerical study of unsteady flow in slits and investigation of methods to reduce pressure pulsations in pipes

Andreas Djupesland

Mechanical Engineering
Submission date: June 2020
Supervisor: Pål-Tore Selbo Storli

Norwegian University of Science and Technology
Department of Energy and Process Engineering

Andreas Djupesland

Numerical study of unsteady flow in slits and investigation of methods to reduce pressure pulsations in pipes

Thesis for the degree of Master of Science

Trondheim, June 2020

Norwegian University of Science and Technology
Faculty of Engineering Science and Technology
Department of Energy and Process Engineering

NTNU
Innovation and Creativity

Dedicated to

the Waterpower Lab

& no one else

Abstract

Some of the water in a Francis turbine leaks up above the runner towards the head cover. In order to avoid heating which leads to boiling of this water it is evacuated through some narrow slits in the head cover. Downstream the slits the water is further evacuated through a pipe system and into a cooling water basin. Vortex shedding occur when high speed rotational water pass through these slits causing pressure pulsations. Measurements were made by Norconsult at Torpa power plant in January 2014 and conducted into a report. These measurement measured some high pressure amplitudes in the volume above the head cover downstream the slit, and in the pipe system. Rainpower developed a hypothesis which suggests that vortex shedding in the slits cause some of these pressure pulsations. If these pressure amplitudes are not reduced or removed it is going to decrease the lifetime of the pipes.

The flow through the slits is investigated using CFD simulations in this thesis work. This is done to validate the hypothesis and develop a numerical model for the case. Rainpower wanted to investigate the effects of the slit design on the pressure pulsations. Since this is a transient case with a complicated flow field it was not possible to look at optimisation of the design in this report due to the time limitations related to CFD. The geometry from Torpa is used in this study trying to validate the CFD with the measurements done by Norconsult. Additional effort was put into finding alternative solutions to solve the problem at Torpa. As such the FFT plots from relevant measurement points were analysed in order to determine which frequencies had high amplitudes. A resonance study was also done based on comparing lengths in the pipe system and wave speeds to standing wave shapes. This was done to establish if resonance can be the source of the problem, or if it can occur after new changes are implemented.

The FFT plots showed that the highest amplitudes were at 36.5 Hz for most of the

runs. A measured amplitude at this frequency were used as an outlet boundary condition in the CFD. Von Karman vortex street is a comparable phenomenon which occur at a Strouhal number of 0.21. Suggesting a characteristic length of 93 mm and a free stream velocity of 40 m/s gives a frequency of approximately 90 Hz. Frequencies was also seen in the slit at 90 Hz in the CFD results. The CFD results did not indicate that the vortex shedding in the slit was the source of the 36.5 Hz amplitudes downstream. This is because there was no amplification of the 36.5 Hz amplitudes in the slit compared to the outlet, and the vortex shedding frequencies did not propagate downstream. However there are many sources of errors in the CFD simulations. As such specific suggestions are made to improve the CFD simulations in the further work.

Resonance calculations did not indicate that resonance was the source of any of the peak amplitudes in the measurement report. This is based on calculations assuming no air content in the pipe. Wave speeds are highly sensitive to air bubbles in the water, and most likely there is a small percentage of air in the water naturally. This could not be accounted for in these simulations. Better assumptions can be made if wave speeds are measured experimentally in the pipes at the plant. There is an accumulator installed at Torpa in the pipe system. This is an hydraulic component which can reduce pressure amplitudes. A reduction in pressure amplitude for the peaks at 36.5 Hz is seen at a measurement point downstream the accumulator. If the air content in the accumulator is increased this will further reduce the amplitudes in the downstream pipes. However, since there are some pipe sections upstream the accumulator, they will still be vulnerable for high pressure amplitudes. If accumulators are installed at all the inlets to this pipe system it will increase the lifetime of all the pipes.

sammendrag

Noe av vannet som strømmer gjennom en Francis turbin lekker opp over løpehjulet mot øvre lokk. Dette vannet evakueres gjennom små spalter i lokket, og ledes videre gjennom et rørsystem til et kjølevannsbasseng. Virvelavløsninger i disse spaltene skaper trykkpulsasjoner når høyhastighets vann passerer gjennom åpningen. Det ble gjort en vibrasjonsmåling av Norconsult på Torpa kraftverk i Januar 2014 som ble sammensatt til en rapport. Disse målingene viste høye trykkvibrasjoner på et målepunkt som er gjort i volumet nedstrøms spalten. Som følge av dette utviklet Rainpower en hypotese som foreslo at virvelavløsningene i spalten kan være årsaken til de høye trykkvibrasjonene. Hvis disse trykkpulsasjonene ikke dempes eller fjernes kan det redusere levetiden til rørene.

Strømningen gjennom spalten ble undersøkt ved bruk av CFD beregninger i denne rapporten. Dette gjøres for å validere hypotesen og også opprette en numerisk modell som fungerer til å løse dette problemet. Rainpower har ønsket å undersøke om designet på spalteåpningen kan gjøres om slik at trykkpulsasjonene fra virvelavløsningene reduseres. Siden dette er en transient case med et avansert strømningsfelt krever det mye tid og datakraft å løse. Dermed har ikke optimalisering av designet blitt vurdert i denne oppgaven på grunn av begrensninger relatert til CFD. Geometrien fra Torpa brukes i CFD simuleringene. Dette gjør det mulig å validere simuleringene mot målingene som allerede er gjort på Torpa. I tillegg ble det gjort arbeid for å finne andre måter å løse problemet på Torpa. Dette inkluderer en undersøkelse av rådataen fra målingene presentert i FFT plot og beregninger på resonans. Rådataen ble brukt til å identifisere hvilke frekvenser som det oppsto høye trykkvibrasjoner på. Resonansberegningene gikk ut på å sammenligne rørlengder og bølgehastigheter med en stående bølgeform som indikerer resonans. Dette ble gjort for å se om resonans kan være en årsak til de høye trykkverdiene eller om det kan bli det i fremtiden.

De høyeste trykkverdiene ble målt på 36.5 Hz på begge målepunktene som er analysert. Denne frekvensen ble brukt sammen med en målt trykkamplitude som grensebetingelse i CFD beregningene. Von Karman avløsninger, som er et nærliggende fenomen, skjer når Strouhal tallet er omtrent 0.21. Hvis man bruker spaltehøyden på 93 mm som karakteristisk lengde og omtrent 40 m/s som hastighet, får man en avløsningsfrekvens på 90 Hz. Det ble også produsert en frekvens på 90 Hz i spalten i CFD simuleringen. Resultatene fra CFD simuleringen indikerte ikke at virvelavløsninger i spalten er en sannsynlig årsak til trykkvibrasjonene på 36.5 Hz. Det var ingen forsterkning av 36.5 Hz frekvensene i spalten, og ingen av virvelavløsningsfrekvensene i spalten forplantet seg videre nedstrøms. Likevel er det mange feilkilder i CFD beregningene som ble gjort. Derfor er det foreslått spesifikke forbedringer som kan gjøres på CFDen som en del av det videre arbeidet.

Resonansberegningene indikerte ikke at resonans var kilden til noen av de høye målingene i vibrasjonsrapporten. Disse beregningene er basert på bølgehastighetsberegninger som antar null luftinnhold i vannet. Bølgeforplantningshastighetene er veldig sensitive til luftbobler i vannet, og det er sannsynligvis en liten andel luft i vannet naturlig. Dette kunne det ikke tas høyde for i disse beregningene. Bedre antakelser kan gjøres hvis denne hastigheten måles i rørene på anlegget. Det er en akkumulator som er installert i rørsystemet. Målingene viser en betydelig demping av trykkverdiene nedstrøms dette punktet. Dersom luftinnholdet i akkumulatoren økes kan denne effekten forsterkes og gi bedre beskyttelse til rørene nedstrøms. Siden det er rør oppstrøms akkumulatoren også er disse utsatt for de høye trykkverdiene i volumet over spalten. Det kan settes akkumulatorer på alle tre innløpene til disse rørsystemene, for å isolere trykkpulsasjonene i volumet over spalten, og dermed øke levetiden på hele rørsystemet.

Acknowledgements

This work would not be possible without the help and creative suggestions from supervisor Pål-Tore Storli. Thanks to Jan Tore Billdal who has been my main contact in Rainpower. Also thanks to the people involved from Eidsiva and Norconsult for providing information needed in this work. Thanks to Einar Kobro who did the measurements and has not only helped collect data, but also provided vital additional information that was helpful in analysing these results. Finally i want to thank Vidar Ahlberger in EDR Medeso who provided solid CFD support.

Contents

List of Tables

List of Figures

List of Symbols

Latin Symbols

A	Area	$[\mathrm{m}^2]$
a	Wave propagation speed/Speed of sound	[m/s]
Co	Courant number	$[-]$
D	Diameter	$[m]$
E	Young's Modulus	$[Pa]$
e	Pipe Thickness	$[m]$
f	Frequency	[Hz]
h	Depth/height	[m]
K	Bulk modulus	[Pa]
k	Turbulent kinetic energy	[]
l	Length	[m]
L	Characteristic Length	[m]
L	Pipe Length	[m]
M	Mach number	$[-]$
n	Number of vortices in a cavity	$[-]$
n	Odd number integer with value 3 or higher	

p	Pressure	[Pa]
Re	Reynolds number	$-$
ρ	Density	[kg/m^3]
S	Surface	[m^2]
St	Dimensionless frequency	[$-$]
t	Time	[s]
U	Velocity	[m/s]
u	Velocity in x-direction	[m/s]
V	Volume	[m^3]
v	Velocity in y-direction	[m/s]
w	Velocity in z-direction	[m/s]
x	General spacial distance, or distance in x-direction	[m]
y	General spacial distance, or distance in y-direction	[m]
z	General spacial distance, or distance in z-direction	[m]

Greek Symbols

Δ	Discretisation size	[$-$]
ϵ	Rate of dissipation of turbulent kinetic energy per unit mass	[]
λ	Wave Length	[m]
μ	Dynamic Viscosity	[kgm/s]
ν	Kinematic Viscosity	[m$^2/s$]
ω	Turbulent frequency (only for section 3.5 k-omega)	[]
ω	Angular Velocity	[rad/s]
∂	Partial derivative	
θ	Angle	[$^\circ$]

Abbreviation

AHC	Above Head Cover
BHC	Below Head Cover
BOM	Bill of material
CFD	Computational Fluid Dynamics
CFX	ANSYS CFX
DNS	Direct numerical simulation
FFT	Fast Fourier Transform
LES	Large Eddy Simulation
NTNU	Norwegian University of Science and Technology
P38	Measurement point above head cover. Figure 5.2
P41	Measurement point in slit pipe system. Figure 5.3
PDE	Partial Differential Equation
RMS	Root mean square
RANS	Reynolds Averaged Navier Stokes
RSI	Rotor Stator Interaction
SST	Shear Stress Transport
Torpa	Torpa Power Plant

Indices

0	Reference value
E	East
e	Entry
h	Hydraulic
∞	Free Stream Value
m	Mean
max	Maximum

min	Minimum
N	North
r	Resonance
S	South
θ	Tangential direction for cylinder coordinates
W	West

Chapter I

Introduction

■ This chapter introduces the case which is investigated in this master thesis study. It involves a background which explains the origin of the problem, motivations for solving the problem and what work has already been done on the issue. The problem description discusses specific tasks that is investigated in the study. Finally the scope introduces how these will be solves, setting boundaries for what this study focuses on. This section also provides some context to the reader about how some issues have been tackled in the report. The chapter ends with a practical description regarding how referencing is practised in this report to provide some clarity for the reader regarding referencing.

1.1 Background

Francis turbines has a protective layer of water between the runner and the head cover. This layer of water ensures that there is no friction between mechanical parts in this area of the turbine, which is necessary for the turbine to rotate. If this water was stationary it would lead to heating and ultimately boiling of the water layer. Therefore the turbine is designed such that a small percentage of the water leaving the guide vanes leaks into the area above the runner. This water flows through a set of labyrinth seals and into a cavity below the head cover. From here it is evacuated through some narrow slits in the head cover and through a system of pipes into a pool of cooling water. At some hydropower plants there have been measured high pressure vibrations in some of the pipes downstream the slit. This can cause the pipes to break. One hydropower plant where high vibrational values have been measured in these pipes is Torpa power plant, hereafter mentioned as Torpa, which will be investigated in this work.

In January 2014 measurements where made on pressure vibrations in several components at Torpa by Norconsult. Measurements were done at different output efficiencies both with and without the use of an air intake. When air is induced in the system it has a large effect on reducing the amplitude of pressure pulsations. Most of the results in this report were satisfactory, but there were some concerns regarding the lifetime the pipes in the slit water system due to high pressure amplitudes in the pipes. The concernes were only raised in the cases where the air intake was not used. The recommendation from Norconsult in the report was that the air intake should be utilised in the future in order to increase the lifetime of the pipe system.

However air from the air intake to not flow through the slit water system automatically. The problem is that the slit water system is upstream the runner which means it is on the pressure side of the turbine. That means that there is no natural suction in this area, which there would be in the draft tube which is another component of the pipe where air is commonly used to dampen pressure vibrations. Because of this the power plant would need to have a compressor running constantly to push the air through the slit water system. This has high costs due to the energy consumption of the compressor and is therefore only used as an emergency solution at the current time.

The most efficient solution would be to find an alternative way to reduce the pressure vibrations in these pipes. Rainpower which is a technology developer for hydro power plants has developed a hypothesis which suggests that pressure pulsations occurs due to vortex shedding in the slits in the head cover. This hypothesis is based on the high pressure vibration values measured in the volume downstream the slits. It also considers similarities between the flow properties in these slits and vortex shedding phenomenons like cavity tone and von Karman vortex streets. They want to investigate whether the design of the slits can be changed such that the pressure amplitudes in the pipes can be reduced. It would also be beneficial to investigate other possible sources to the high pressure amplitudes in the pipes. Resonance in the pipe system downstream the slits is one alternative possible explanation for the high pressure amplitudes. The pipe system has a lot of different components like 90 degree bends, branches, expansions and contractions which leads to partial reflections of pressure waves. As such there are several pipe sections where resonance can occur. Changes can be made to the pipe system in order to eliminate the resonance.

1.2 Problem Description

The master thesis work conducted in this report is done in cooperation with HydroCen and Rainpower. Effects from the design of the slits in the head cover will be investigated numerically. This is done to test the hypothesis that these contribute to the high pressure pulsations in the downstream pipe.

Other solutions to problems regarding fatigue on the downstream pipes will also be investigated. This includes a mapping of the lengths in the pipe systems where pressure waves will be reflected and calculate resonance frequencies by hand for these pipe lengths. Finally these frequencies will be compared to the raw data from the slit water system measurement point in the vibration measurements. The purpose of this study is to identify whether there is resonance present in the slit water system and possibly in which pipe sections resonance occurs. This data will also make it possible to identify an approximate amplitude and frequency of the pressure wave in the pipe section in the numerical model used in the CFD.

The following assignments will be considered in this study:

1. Perform a literature study recapping relevant theory from the preliminary study in the project thesis, and add additional findings.
2. Develop a numerical model for unsteady flow in slits and simulate the current case from Torpa.
3. Map the pipe system at Torpa and identify relevant lengths for pipe sections to be used when investigating resonance.
4. Use experimental data from the vibrational measurements at Torpa in 2014 to identify frequencies and amplitudes in the case. Calculate possible resonance.
5. Investigate other possible solutions to the problem based on the measurements.

1.3 Scope

The goal of this master thesis is to work on solving the issue with pressure pulsations that causes fatigue in pipes in the slit water system at Torpa. It is also beneficial if a solution also can be implemented in similar cases at other hydropower plants. Several possible solutions exist if there is resonance present in any of the pipe sections in the slit water system. It can be eliminated by either making permanent changes to the length of the pipe or utilising an accumulator. The accumulator can be used to dampen high pressure amplitudes and will also lead to a partial reflection of the pressure. Magnitudes of the dampening and reflections are decided by the volume of air or gas in the accumulator.

Resonance in a pipe implies that there is a standing wave present with nodes inside the pipe. This means that resonance can only be achieved at specific wavelengths related to the total pipe length. As such the resonance frequency in a pipe is only dependent on the length of a pipe section and the wave speed. It can be established whether resonance is present by measuring the wave speed and frequency and compare it to specific resonance frequencies. This solution would be specific for the case at Torpa, but could represent a simple method of solving similar issues in other systems of pipes at other hydropower plants.

Another possible solution which Rainpower want to investigate is to change the design of the slits in the head cover. This assumes that the hypothesis that vortex shedding in these slits are cause pressure pulsations that propagate into the pipes downstream. As such this hypothesis needs to be properly validated for the current case at Torpa before new designs can be considered. This includes establishing a numerical model based on known properties from Torpa. A domain needs to be established with an acceptable mesh and boundary conditions. Due to limitations in time and computational power, efforts has to be put into simplifying the case, domain and mesh.

A large part of the work in this study is gathering information on the case from different sources. This include Rainpower that wants to investigate the problem, Eidsiva who owns the power plant and Norconsult who performed the measurements that are used in the assignment. Different information has been available at different times in the study, and there has also been misunderstandings that has been clarified in later stages of the study. Some of this information has become available at a late stage and was not included when important assumptions were made for the CFD analysis. To account for this the report is structured such that the CFD setup is presented with the information that was available at the time of the simulations, and additional important information is introduced when discussing the results. This is done interpret how this information influence the results.

1.4 Referencing

The theory section in this report will include entire sections or paragraphs that is extracted from the same reference. These paragraphs will be referenced at the end of the paragraph. When the same reference is used in an entire section the reference brackets will appear in front of the first sentence in the section. Specific references that relates only to one or two sentences is referenced in the text at the end of the sentence. Figures are referenced directly in the captions when they originate from another source.

Chapter II

Literature Study

■ This chapter covers the fluid mechanics theory used in this study. There was not many articles that investigated this specific phenomenon after searches in the library database and Google Scholar. As such this chapter is based mostly on theory from similar phenomenons in textbooks, with the results from a few research papers on hydropower plant also being considered. The first section compare other vortex shedding phenomenons to this case and lists key characteristics. This includes Cavity Tone and von Karman vortex shedding. The rest of the chapter studies theory related to pressure propagation. Resonance has been investigated, where it is established that resonance occurs with a standing wave form. Frequencies at resonance conditions can be calculated from pipe lengths and wave speeds. Accumulators have also been investigated. The wave propagation section investigates wave speeds, how they can be calculated and what factors they are influenced by. Equation of state relates to compressibility, how it can be accounted for, and how much it has influenced the results in similar cases. Finally fast fourier transforms are introduced, which is going to be vital when investigating the results from the measurements and the CFD simularions.

2.1 Vortex Shedding

2.1.1 Cavity Tone

[1] The theory that unsteady flow in the head cover slits is a source for high pressure vibrations in downstream pipes implies that some sort of flow induced vibration is occurring. A well documented phenomenon with similarities to this case is cavity tone. This phenomenon describes how high speed flows passing over a cavity

generates vortex shedding. When the shear layer of the flow interacts with the trailing edge of a cavity it reflects a sound wave upstream towards the leading edge interacting with the flow. This creates a periodic vortex on the shear layer as illustrated in figure 2.1.

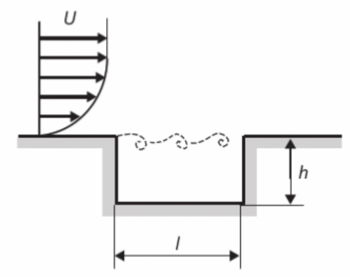

Figure 2.1: Flow over two dimensional cavity. [1] figure 5.48 p.261

The effect from the length height ratio, l/h, on the non-dimensional frequency Strouhal number, $St = \frac{fL}{U}$, on a two-dimensional square cavity is investigated in chapter 5 of [1]. It shows experimentally that St converge for a given number of vortices in the cavity, n, with increasing length height ratio.

Effects on rounded off edges on acoustic resonance in side branches was investigated in [1] reference [164] chapter 5. The studies showed that increased upstream edges had minor effects on the amplitude of pressure pulsations in the cavity, while it increased the free stream velocity needed to reach peak acoustic resonance. According to equations in the source, this implies that the frequency decreases with increased upstream round off edges. Interestingly rounding off downstream edges has a different effect reducing the amplitude of pressure pulsations while leaving the frequency relatively changed. If vortex shedding in the head cover slits are found to be the reason for the high vibrations in the downstream pipes at Torpa, rounding off edges of the slits might be used to tune the pressure wave such that high amplitudes and resonance are avoided.

2.1.2 von Karman vortex street

[2] Another phenomenon describing oscillating flow is the vortex street investigated by Theodore von Karman. This describes when water in a steady stream hits a blunt body creating an array of alternating vortices in the stream. Oscillating flow properties depend on non dimensional frequency, St, and the Reynolds number $Re_L = \frac{UL}{\nu}$, and this condition occurs at approximately $10^{-2} < Re < 10^{-7}$ and $St = 0.21$. Resonance can occur if the frequency of the alternating vortices corresponds with structural vibration frequencies or other oscillating frequencies in

the flow.

For the case at Torpa there is no alternating flow pattern. As such cavity tone seems like a more comparable flow phenomenon than von Karman vortex streets. However the phenomenon might occur at similar frequencies as they are both based on vortex shedding. A Strouhal number of 0.21 equals a frequency of 62 Hz using the slit length as the characteristic length, and a velocity of 40 m/s which is approximately the rotational velocity at the radial position of the slit. Using the slit maximum height as the characteristic length gives a frequency of 90 Hz. Slit dimensions are listed in a later chapter in figure 4.3.

2.2 Pressure propagation

2.2.1 Resonance

[5] Resonance is a condition in oscillating motion that leads to an amplification of the pressure in a system. In large diameter frictionless pipes the condition for resonance appears to be a standing wave. This condition implies that two interacting pressure waves of the same frequency creates points of zero fluctuation. These points are called nodes. The reason these points are fixed is that the pressure value of one wave equals the negative displacement of the other wave at all times. However this leads to an amplification between the nodes. The largest amplification occurs in the middle, where the displacement of the wave is always equal between the two waves. Waves will pass these points at the same time doubling the resulting pressure amplitude. This is something that can happen in pipe systems when a pressure wave is reflected at a constant head reservoir.

The standing wave condition is only present at certain wave periods. Assuming a sinusoidal displacement, a fundamental period occurs at a period of $\frac{4L}{a}$ where L is the length of the pipe and a is the wave propagation speed. Other periods called harmonic periods occurs at $\frac{1}{n}$ fractions of the fundamental period. This means the second harmonic is $\frac{1}{2}$ of the fundamental period, the third harmonic is $\frac{1}{3}$ and so on. As such the harmonics of a pipe is present at certain ratios of wave lengths λ and pipe lengths. These wave lengths can be represented by (2.1) with n equaling any integer representing which harmonic it corresponds with.

$$\lambda = \frac{4L}{n} \tag{2.1}$$

Keeping one end fixed, oscillatory motion is only present at the free end for odd harmonic periods $3, 5, 7, 9, ...$ meaning resonance occurs at these wave lengths. A fixed end means that one end of the pipe is kept at constant head and that is the case at Torpa for the outlet to the cooling water basin. As such the resonance frequency in a pipe section is calculated from (2.2).

$$f_r = \frac{a}{\lambda} = \frac{a}{4L/n}(n = 3, 5, 7, ...) \tag{2.2}$$

For more complex pipe systems partial reflections can affect resonance conditions. Such reflections can occur from changes in pipe characteristics, for instance a sharp increase or decrease in diameter or a sharp bend and from introduction of hydraulic elements such as an accumulator. Branched and parallel systems complicates the case as well making it difficult to find theoretic periods for the systems. However fundamental periods can always be found in any system with the use of free vibrational theory. Higher harmonic resonance is also possible for complex system, with dead end frictional pipes displaying high pressure fluctuations at dead ends for the odd harmonic cases.

An accumulator is a type of hydraulic element that can be installed in the flow and used to reduce pressure pulsations. It works by installing a volume as a side branch on the pipe partially filled with water and partially filled with air or gas. The volume of air in the accumulator can be adjusted to reduce the maximum pressure values to a predetermined value. It can work by having an air compressor or gas supply that adjusts the volume or by having a flexible membrane or piston that separates the fluid and the gas. The accumulator will reflect a partial pressure, while letting the remaining amplitude pass depending on the air or gas volume.

2.2.2 Wave propagation

The sound speed of water in a certain case is regularly assumed to be constant in literature. [6] This is the acoustic wave propagation speed which typically range from $1200 - 1400$ m/s for high pressure water in small pipes. Assuming water with no free gas particles a closer estimate can be obtained from only fluid properties and pipe parameters (2.3), where K is bulk modulus of the fluid, E is Young's modulus for the pipe material and e is the pipe thickness. [2]

$$a = \sqrt{\frac{K}{\rho(1 + KD/Ee)}} \tag{2.3}$$

An increase in air content in the water will rapidly decrease the wave propagation speed for a given pressure. However if the pressure is increased enough it will return to its former high value. This is because the wave propagation speed varies very little with pressure after reaching a certain threshold as shown in figure 2.2.

As such the assumption of no free gas in the fluid can be used to find the maximum acoustic wave speed for flow in a given pipe. [2]

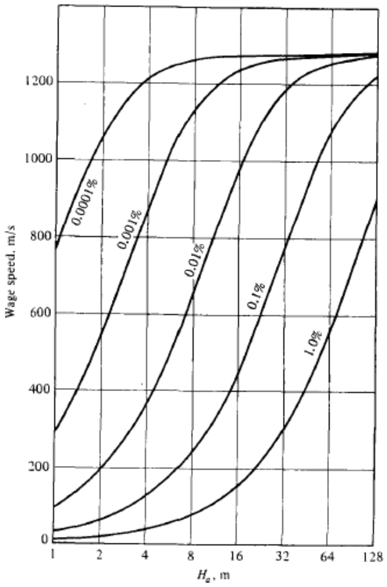

Figure 2.2: Wave speeds in water for different air contents for a specific pipe. Data for a pipe with (K/E)(D/e)=0.263. [2] figure 8-3 p.140

2.2.3 Equation of State

[6] In most cases it is a fair assumption to consider water as an incompressible fluid. However in reality water is compressible and that can have an effect in some cases. The effects are not seen as often due to low mach numbers in water applications, but for transient phenomenons compressibility is a key factor. Research done on a pump turbine case show that introduction of compressibility in simulations affects the frequency and amplitude of pressure pulsations. It showed that compressible simulation had larger pressure fluctuations which corresponded better with experimental results. Without considering compressibility low frequency components of pressure waves could not be determined.

The assumption that the sound speed is constant in systems is regularly used when determining an equation of state for water. There is no commonly used equation to determine changes in density with other variables for water because it cannot be considered as an ideal gas. If the water is assumed to be isothermal, a relationship can be determined such that density only varies with pressure in the fluid (2.4).

$$\frac{\partial p}{\partial \rho} = a^2 \tag{2.4}$$

Usually it is accurate to assume that water in a drain pipe system is isothermal because water has high heat capacity. In the case at Torpa there might be some heating due to high friction in the water between the rotating runner and stationary head cover, but since it is upstream the area of interest its effect on the density changes is negligible. Assuming changes in density are small, which they would be for cases with small Mach numbers, a linear relationship can be used (2.5).

$$(p - p_0) = a^2(\rho - \rho_0) \tag{2.5}$$

A study done HydroCen at NTNU investigated the effect of compressibility in simulations in a high head Francis turbine. Specifically the effect of Rotor Stator Interaction (RSI) in the system were investigated. The study showed that compressible model had higher accuracy than the incompressible, where the incompressible model predicted lower pressure amplitudes. The strong effect of RSI in labyrinth seals could not be predicted by the incompressible model. [7]

The flow in the high head Francis turbine case and the pump-turbine case investigated in [6] has similarities to the flow field in the slit water system at Torpa due to the high rotational velocities in a confined space. Compressibility might be as important in order to accurately predict amplitudes in the slits. However these cases only stated that the accuracy was higher when considering compressibility in simulations and did not state that incompressible models was unable to recreate such flow phenomenons.

2.2.4 Fast Fourier Transform

[8] A fast fourier transform, abbreviated FFT, is a mathematical transformation that can be used to interpret sine wave signals with noise or several frequencies. After performing a FFT the result can be manipulated and used in a plot of amplitudes vs frequencies for a signal. There are some mathematical limitations to the frequency resolution of the FFT plot. The energy from the signal is divided between bins at specific frequencies and the frequency resolution is the distance between the bins. This resolution is restricted to the sampling frequency divided by the size of the signal, which can be an issue when used on CFD simulations which run for a short time compared to an experimental measurement.

Chapter III

CFD theory

■ This chapter contains an introduction to all the CFD theory that is used in the CFD simulations. Information is presented at the level of what is needed to know by a CFD user. The chapter starts by introducing the CFD software that is used which is ANSYS CFX followed by a short description of the governing equations which are solved numerically in the simulations. The next section is about meshing including information on mesh refinement, mesh quality and mesh types. More in depth explanations about mesh quality can be found in appendix A.2 for readers that are not familiar with the parameters. Numerical Schemes are presented with an introduction of different categories of schemes, and the equations they solve. It also discusses stability where the Courant number is a key performance indicator. Turbulence models are included only with discussions related to the performance in different areas of the simulations. y_+ is a non dimensional distance which is also introduced in this section. The y_+ value for the closest grid point to the wall is the main performance indicator used for turbulence models in this study. Finally verification and validation methods are introduced, which can be used to control the solution in the simulations.

3.1 CFD Introduction

The numerical calculations in this study will consist of CFD-simulations. ANSYS CFX will be used to perform these simulations. This software has preferable properties regarding rotating bodies, and as such it is widely used for simulations on turbomachinery applications. In this case the most complicated feature is rotating walls so this study could also be performed using ANSYS Fluent. For simplicity this study will only consider CFX, but both softwares are equally suited. ANSYS provides a collection of commercial softwares meaning that the source code from CFX will be unavailable. All information on the software is gathered from the manual [9]. It is going to be assumed in this thesis that ANSYS CFX is a trustworthy software due to it being widely used in other research project, and the code does not need to be controlled by the user. This chapter will present information that is needed to know from a user perspective.

3.2 Finite Volume method

Fluid mechanics are governed by three conservation laws. These laws are conservation of mass, momentum and energy. Conservation of mass, also known as the continuity equation (3.1), states that mass cannot be created or destroyed at any point. Conservation of momentum governs the force balance in the fluid and is represented by the commonly known Navier Stokes equation (3.2). Conservation of energy states that energy cannot be created or destroyed it can only change form.

In most cases these partial differential equations cannot be solved analytically without doing specific simplifications to the problem. A common way to solve these equations is to discretise a domain and solving the governing equations using finite differences and boundary conditions. This is called the finite volume method and it is the method used in CFD calculations. Continuity and Navier Stokes can be written on differential form as (3.1) and (3.2) respectively.

$$\frac{\partial \rho}{\partial t} + \frac{\partial(\rho u)}{\partial x} + \frac{\partial(\rho v)}{\partial y} + \frac{\partial(\rho w)}{\partial z} = 0 \tag{3.1}$$

$$\frac{\partial(\rho u_i)}{\partial t} + \frac{\partial(\rho u_i u_j)}{\partial x_j} = -\frac{\partial p}{\partial x_i} + \frac{1}{Re}(\frac{\partial \tau_{x_i x_j}}{\partial x_j}) \tag{3.2}$$

Conservation of energy is simplified in this case using (2.5) as the equation of state for compressible simulations. The speed of sound needs to be specified in that case, and it can be calculated from (2.3) or measured experimentally. Incompressible simulations means that the density is assumed to be constant. This implies that $\frac{\partial \rho}{\partial t} = 0$ in the continuity equation (3.1).

3.3 Mesh

3.3.1 Mesh Refinement

The discretisation of the domain in finite volume method is done by defining grid points in the geometry. In CFD this grid is called a mesh. The finite difference schemes has an error in the order of the spacial discretisation, Δx_i or Δx_i^2, of the mesh. As such the accuracy of a CFD simulation usually increase with number of cells, which leads to a decreased distance between the grid points.

When describing a complex flow field or flow in a complex geometry however, the accuracy also depends on other factors. If there are large changes in flow properties over a short distance, the resolution needs to be high in this area in order to capture all the details. In other areas the changes might be smaller and good accuracy can be achieved with a lower resolution. There are limitations in computational power and computational time increase rapidly with the number of cells in the mesh. As such it is beneficial to refine the mesh, which means that cell sizes are specified locally such that high accuracy can be achieved with a lower number of cells.

3.3.2 Mesh Quality

Mesh refinement comes at a cost though, and carelessness when refining a mesh can lead to inaccuracy due to poor mesh quality. Several parameters exist to account for errors that occur due to poor quality. When talking about mesh refinement the main issues occur due to poor smoothness or poor aspect ratio. Smoothness measures the difference in spacial discretisation from one cell to the next. Numerical losses can occur if flow passes through an area with a large jump in cell size in the flow direction. The best performance is achieved with a smoothness value of 1, but 0.8-1.2 is acceptable [9]. In ANSYS the solver governs smoothness with the growth rate setting.

Aspect Ratio is another mesh quality parameter which can become an issue when refining a mesh. It states that the highest accuracy is achieved if the sides in a cell is equal in all directions. This can become an issue, especially when refining the inflation layers close to the wall in order to rapidly increase the resolution of the boundary layer. Skewness and orthogonality are mesh quality parameters that might become an issue when dealing with complex geometry. Poor skewness occurs when the smallest angle of cells are too sharp, which makes it difficult for the solver to resolve the cells in the area. Orthogonality is a measurement of errors that occur due to a difference between a point where the flux between two cells is estimated and the point where its value is calculated. These mesh quality parameters are described in more detail in appendix A.2. The goal is to achieve a mesh independent solution which means that the result does not change significantly with an increase in mesh size.

3.3.3 Mesh types

[10] The grid points in a mesh can be arranged in several different ways. A mesh which is only consisting of cubic cells in 3D is called a structured mesh. These cells are often referred to as hexahedral cells which indicates that it has six sides. A mesh with these properties can be indexed using i, j and k in different directions in order to easily identify neighbours. The quality of a structured mesh is reduced if there are points where less or more than 4 corners meet. One example where this issue can occur is a circular pipe which cannot consist of only hexahedral cells and have 4 cells meet in all corners at the same time.

More complex geometries can be easier to capture using differently shaped cells. This type of mesh is called an unstructured mesh. Tetrahedral cells with four faces in 3D are commonly used in these meshes, but other shapes are also possible. In this case neighbouring cells will need to be identified using an indexing table which is more complicated, but in softwares like ANSYS this is taken care of automatically. Since a tetrahedral cell with the same face area as a hexahedral cell only covers half the volume, double the amount of cells of the same size is needed in order to capture the same geometry. Double the amount of cells means it takes roughly twice as long for the simulation to finish. Hybrid meshes are a third option which consist of multiple types of cells.

3.4 Numerical Schemes

3.4.1 Implicit and Explicit Schemes

In CFD calculations the governing equations is solved for all the discrete points in the mesh using numerical schemes. Different schemes exist in order to solve different types of equations. The two main categories are explicit and implicit schemes. Explicit schemes solves the equations using known values from previous timesteps, while implicit schemes solve several unknowns at the same time utilising matrice calculations.

The most important property to be aware of for a CFD user is the stability criterion. An important tool in order to investigate and predict stability in a simulation is the Courant number, $Co = a\frac{\Delta t}{\Delta x}$, which depends on the discretisation step in time and space as well as the velocity, a, in the cell. For explicit schemes this value can never be higher than 1. This condition states that no information can travel further than one cell length during one timestep. The reason this is not possible is that cells only communicate with the closest neighboring cells in all directions. As such a cell cannot capture information from cells that are not neighboring for a given timestep. [11]

Implicit schemes can be stable for Courant numbers higher than 1 in some cases. The specific stability criteria varies between different implicit schemes. These schemes are more difficult to implement for the user, but when they are implemented in commercial software like ANSYS it can be used at a computational cost.

3.4.2 Advection Schemes

The left side of the Navier Stokes equation (3.2) represent an advection equation with a non-linear element, $u_i \frac{\partial u_j}{\partial x_j}$, where the subscripts i and j represent the directions in space. Advection equations describes the transport of a substance or quantity. In CFX there are several options for schemes that solve this equation with the main ones being the upwind scheme and high resolution.

First order upwind scheme is first order accurate in time and space, which means that the error from one timestep to another is in the order of the discretisation steps in time and space. It is an explicit scheme meaning it is stable for $Co < 1$. If this criteria is fulfilled it converges very well compared to high resolution, but it is far less accurate due to a high value of numerical viscosity. Numerical viscosity means that the scheme includes a numerical link to the viscosity as an unwanted side effect. This means that the upwind scheme flattens gradients causing large errors in sections with sharp change in flow properties. As such the upwind scheme is best suited for initialisation. There is also higher order upwind schemes that perform better, but the CFX pre user guide confirms that the "upwind" selection is the first order one. [11]

The other option, high resolution, use a blend factor to change between first and second order schemes in different areas. High resolution utilises a program controlled blend factor which automatically changes the scheme based on gradients from former time steps. [9] First order schemes converge faster and can be used with decent accuracy for areas with low gradients at a lower computational cost. Areas with sharp gradients can be resolved more accurately using second order schemes in the area. Another option is to manually control the blend factor, but that option is complicated and require more experience. The user manual does not state clearly which second order schemes are used, and therefore it is unclear whether or not the advection schemes are implicit. As such it is safest to assume that the schemes are stable for $Co < 1$.

3.4.3 Transient Scheme

CFX utilises several different schemes to solve different parts of the governing equations. Transients schemes are used to progress the simulation from one timestep to the next. The main schemes which are used in CFX are First- and Second order Backward Euler. The properties are comparable to the advection schemes, where the first order one have errors related to numerical diffusion but converge faster, but the second order is more accurate. Both backward Euler schemes are implicit. High resolution is also an option for transient schemes with program controlled change between first and second order schemes in different areas. The solver look at the time gradient when determining what order of scheme to use. [9]

3.5 Turbulence Models

3.5.1 Reynolds Averaged Navier-Stokes

It is computationally expensive to resolve turbulence directly. As such most CFD simulations require some sort of turbulence modeling. Direct Numerical Simulation, known as DNS, and Large Eddy Simulations, known as LES, are the most accurate ways to resolve turbulent effects. However it is unrealistic to be able to model the turbulence with either DNS and LES in this study due to limitations in time and computational power. The remaining option is Reynolds Averaged Navier-Stokes, known as RANS, which is the only option which will be considered for this thesis.

RANS accurately models the effects from turbulence on the mean properties of the flow, but has some weaknesses regarding solving detailed turbulent fluctuations. Resolving such fluctuations accurately are not considered to be necessary for most engineering purposes. In RANS the turbulence is defined as a sum of a mean and a fluctuating part of the flow. The fluctuating part is resolved using classical turbulence models, with some examples being $k - \omega$, $k - \epsilon$ and $k - \omega$ SST. This part will not include detailed descriptions of how the different turbulence models solve the different equations, but rather describe key advantages and disadvantages related to the different turbulence models considered for this CFD study. [12]

3.5.2 Y plus

Y plus is a tool that can be used in order to determine which turbulence model will perform most efficiently in different areas. It is a non-dimensional length property, $y_+ = \frac{yu_\infty}{\nu}$, that determines at which part of the boundary layer a grid point is located based on the free stream velocity as shown in figure 3.1, u_∞, and the kinematic viscosity ν. High cell resolution close to the wall is needed in order to properly resolve the boundary layer effects. y_+ values of the closest grid point to the wall is commonly used as a performance indicator for the chosen turbulence model. Since the free stream velocity can be hard to predict at all points in the flow field, it is a good strategy to run a steady state simulation with one mesh checking y_+ at the walls and then refine the mesh accordingly.

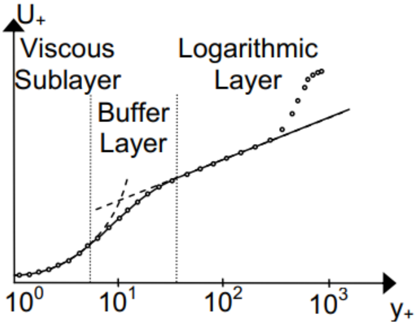

Figure 3.1: Plot of non-dimensional velocity, u_+, against y_+ indicating the different zones within a boundary layer. [3] figure 4-1 b) p.26

3.5.3 $k - \epsilon$ Model

$k - \epsilon$ is a two equation model which is based on capturing details of the fluctuations in the instantaneous kinetic energy k and rate of dissipation for turbulent energy per unit mass . [12] It is widely used as a turbulence model in RANS calculations. The model performs most efficiently in the free stream and struggles to capture the most detailed effects in the boundary layer. This means it performs best in the logarithmic layer as shown in figure 3.1, and the y_+ value of the closest cell to the wall should be somewhere between 30 and 100. [3] This model performs best with an inflation layer containing 5 to 10 cells within the boundary layer.

3.5.4 $k - \omega$ Model

$k - \omega$ is another two equation model which utilises turbulent frequency, $\omega = \frac{\epsilon}{k}$, in order to define turbulent eddy viscosity. [12] This model resolves the viscous sublayer well compared to $k - \epsilon$, but struggle with stability issues in the free stream. These stability issues makes it hard to rely on $k - \omega$ in the entire domain and it is better used only in certain areas. [13] This turbulence model performs best at very high cell resolution in the boundary layer, meaning the y_+ value closest to the wall should be around 1. [3] 10 to 20 cells in the boundary layer is needed in order to solve the boundary layer effects properly.

3.5.5 Shear Stress Transport

In order to combine the free stream stability from $k - \epsilon$ with the boundary layer accuracy from $k - \omega$ there is a turbulence model combining the two models. This model is known as $k - \omega$ SST in literature and is called Shear Stress Transport in ANSYS CFX. $k - \omega$ SST utilise a blending function switching from $k - \omega$ inside the boundary layer to $k - \epsilon$ outside. In ANSYS the change is program controlled and is monitored by the calculated y_+ values from previous iterations. Because boundary layer effects are assumed to be important in this study Shear Stress Transport will be used in the simulations.

3.6 Verification and Validation

3.6.1 Verification

[4] CFD-analyses are complex in many cases and it is difficult to accurately predict the accuracy of a simulation. Verification is a way of controlling the quality of the numerical model and quantify errors in the simulations relating to the transition from the physical model. This relates to residual convergence, mesh convergence, errors in the code and consistency checks like mass conservation for instance.

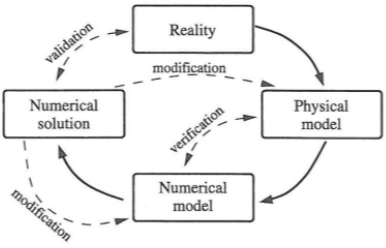

Figure 3.2: Illustration of the relation between different steps in CFD analysis. [4] figure 13.1 p.281

Residual convergence is when the residuals are negligible. They measure the change in flow properties from one iteration to the next. For steady state simulations residuals decrease with the number of iterations until a convergence limit is reached. In transient simulations they will usually increase with the jump from one timestep to the next, and more iterations could be made at a timestep in order to reduce the residuals to the convergence limit. However a converged simulation does not necessarily mean it is an accurate one. Therefore it is vital to also have mesh convergence. That means that the change in results of a simulation is negligible with an increase in mesh size. This convergence study is done by running the same boundary conditions on different meshes and comparing the results. Usually it can be assumed that higher resolution means higher accuracy, but that will not be the case if the mesh quality is reduced.

Since CFX is assumed to be reliable the code does not need to be checked, but it is always good practice to check the program inputs for mistakes by the user. Consistency checks means checking the results against known properties. For instance mass conservation where the mass in should equal the mass out in any volume in a steady state simulation. [14] Another option is to check for known fluxes that are not directly defined in the program for example the flux through the slit at Torpa which is assumed to be known.

3.6.2 Validation

[4] Even if a simulation is verified and the numerical model corresponds perfectly with the physical model, the results still may contain significant errors compared to reality. Errors and simplifications that are done when establishing the physical model can still have a significant effect on the results. These errors are controlled and quantified by performing a validation. This means that the results are compared to other results that are more reliable like experimental results. Simulations of higher accuracy like DNS simulations are also acceptable as validation if they have been properly verified and validated. In some cases where simulations are done on structures that are inaccessible or have not been built yet, validation can be challenging. The solutions in these cases are to break down the case into smaller known cases and validate these individually.

Chapter IV

CFD setup

■ This chapter contains a detailed description of how the CFD simulations were set up, with discussions on choices that were made in the process. The goal is to explain it at a detailed level such that another person has all the information needed to perform the same simulation on another computer. This will make it easier to improve upon the decisions made in the further work. The chapter starts by introducing a detailed domain which is close to the real geometry. Many figures are included in this section to give the reader a better picture of the geometry without having to study the mechanical drawings in detail. The boundary conditions of the initial domain is also explained in detail. Some of these are still used after the simplifications were made, and will be repeated in less detail at the end of the chapter. The simplifications that were considered is presented in the next section, discussing if they can be made or not, and how they will influence the simulations. Meshing is explained in detail with all mesh refinement parameters listed in tables. This section also includes a mesh dependency study with seven meshes which serves as part of the verification. Finally the mesh quality is analysed for the final mesh which is named Mesh 4 in this chapter. The setup in CFX pre is discussed in the final section. Many of these points are discussed earlier in the chapter and is presented in less detail in this section. The outlet conditions requires some assumptions which are discussed in detail. This section also contains some analysis of the residual plots from the final transient simulation.

4.1 Initial Domain

A domain was developed for the CFD-simulations in the prior project thesis work based on the geometry at Torpa power plant, and further developed during the first period of the master thesis work. The inlet is located at the final labyrinth seal sending a beam of high speed water through a narrow gap into the volume upstream the slit. Both volumes below and above the head cover and the slit is included in detail as interpreted from the machine drawings in appendix B.1. Finally the outlet is set in the pipe leading to the slit water system.

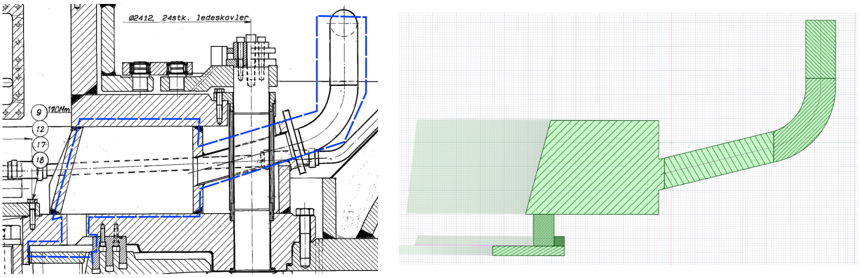

(a) Outtake of the mechanical drawing in figure B.2 with the domain marked in blue.

(b) Cross sectional view of detailed CFX model created in SpaceClaim.

Figure 4.1: Comparison between mechanical drawing a) and CFX model b).

The head cover at Torpa has three slits placed axisymmetrically at 120° and three drainpipes evacuating the water at the same angles. As such a symmetry condition can be created including only a third of the volume and assuming that the flow in the three sections are identical. It is a good assumption because the geometry is identical and the CFD solver has no way to separate between identical sections with equal boundary conditions. The symmetrical section is displayed in figure 4.2.

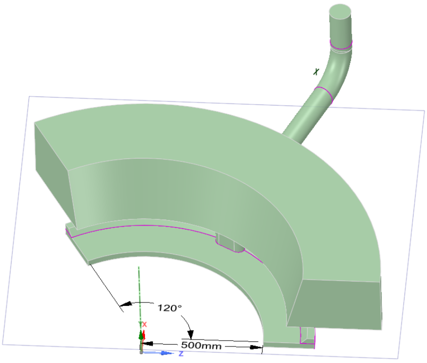

Figure 4.2: SpaceClaim model displaying the rotational symmetric domain for a slit at Torpa.

The main area of focus for the CFD part of this study is the slit in the head cover. A long term the goal in the study is to establish the effects from the geometry on downstream pressure pulsations caused by vortex shedding in the area. The slit consists of a rectangular $75x30$ mm mid section with two half circles of 30 mm radius on the ends. The slit is 93 mm deep, and goes through a section where the head cover thickness changes to 65 mm along a 45° angle. Due to the geometry being slightly curved in SpaceClaim it is hard to get accurate length measurements, but the differences are negligible. The location and dimensions of the slit is displayed in figure 4.3. The volumetric flow rate through the slit is defined as constant at 48 L/s which corresponds to a $0,3\%$ leak from the best water flow at 1600 L/s through the machine. It is assumed that the volumetric flow rate through the slit is constant also when the flow through the machine is reduced.

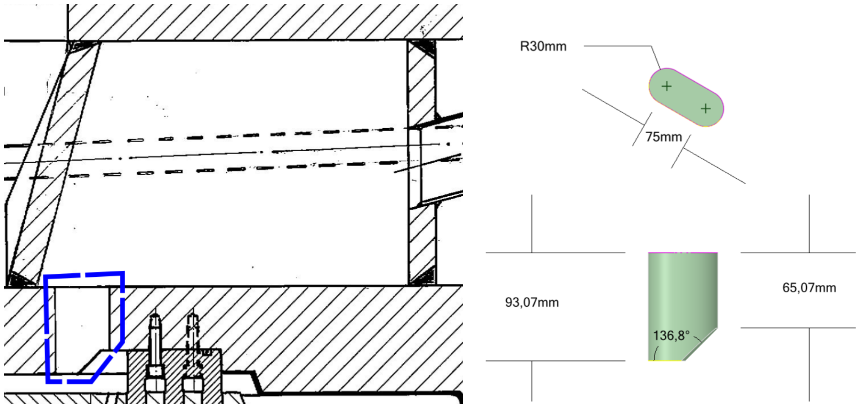

(a) Outtake of the mechanical drawing in figure B.2 with the slit marked in blue.

(b) Spaceclaim model of the slit displaying relevant dimensions.

Figure 4.3: Indication of the slit location from the mechanical drawing a) and Spaceclaim model of the slit displaying dimensions b).

4.2 Initial Boundaries

4.2.1 Inlet

The inlet of the domain was initially defined as the exit of the final labyrinth seal which is displayed in figure 4.4. This is a 0.75 mm gap which is placed at approximately 709 mm from the center of rotation around the entire domain. All the 48 L/s that pass through each slit has to enter the domain through this gap. As such the axial velocity of the water is very high at approximately 43 m/s.

The inlet condition is complicated further by the innermost wall which is rotating with the turbine at 600 rpm which equals $62,83$ rad/s and a tangential velocity of $44,55$ m/s, while the outermost wall is stationary. To accurately resolve the flow in this seal there would need to be 10-20 cells within the boundary layers and also a high resolution in between causing the mesh size to increase by hundreds of million cells.

This would lead to a case where the, by far, smallest cells are in the same area as the highest velocities in the entire domain. It would require an extremely small timestep to satisfy the stability conditions discussed in section 3.4. The inlet condition was initially simplified to having a depth of one cell where the width and depth of the inlet was $0,75$ mm. The side walls were defined as free slip walls allowing uniform flow to enter the domain from the inlet at an axial velocity of 43 m/s and a tangential velocity of $44,55$ m/s.

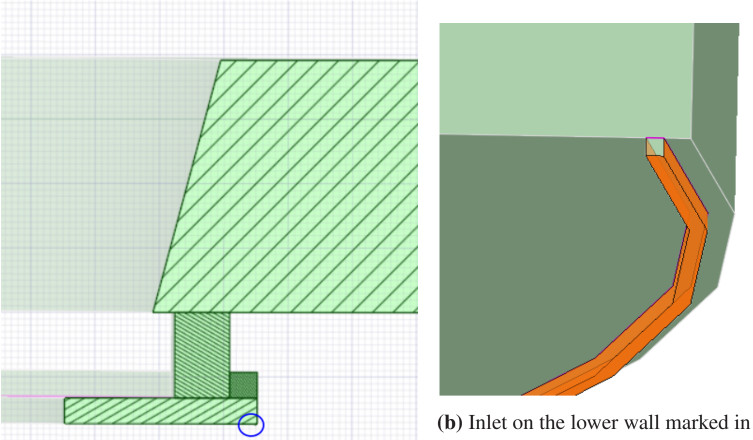

(a) Location of the inlet marked on the cross section view in figure 4.1 b)

(b) Inlet on the lower wall marked in orange. The side walls, also marked in orange, are defined as free slip walls.

Figure 4.4: Inlet boundary location.

4.2.2 Outlet

The outlet of the domain is placed inside the pipe downstream the slits. From the slit to the pipe entrance there is a distance of approximately 360 mm. The first section of the pipe is a 345 mm straight section at an angle of $14°$. The pipe continues through a bend at 180 mm radius of curvature for 240 mm. Finally the outlet is located 195 mm downstream the bent pipe.

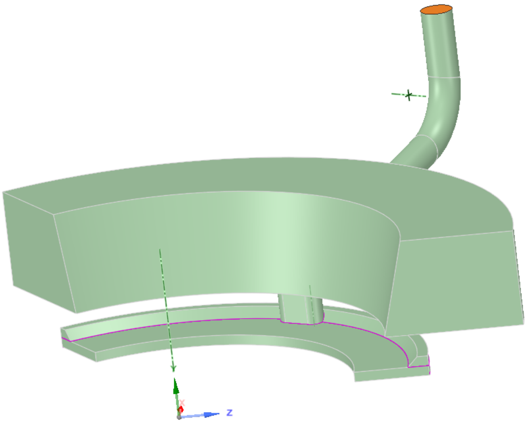

Figure 4.5: SpaceClaim model with the outlet boundary marked in orange.

In order to accurately predict effects from a certain geometric element the outlet needs to placed sufficiently downstream this geometry. Normal practise is to define a characteristic length for the case based on this geometry. The length of this pipe section was measured roughly with a ruler and protractor by hand based on figure B.4 as 780 mm. Using the max slit height, $h = 93$ mm, as the characteristic length this gives a distance from the slit outlet to the CFD outlet of $12,26h$.

It depends on the specific case how large the distance needs to be to the outlet. There has not been done any studies regarding how far turbulent details propagate in the flow at Torpa. Reynolds numbers are high in this case and might cause turbulent effects from the slit to propagate further downstream than the distance to the outlet. For the pipe the Reynolds number $Re_D = \frac{Du_m}{\nu}$ is in the range of $800,000$ assuming a volumetric flow rate of 48 L/s. This might cause some errors because these effects are difficult to account for when creating the boundary condition.

The outlet was placed at this location because it is at a 90 degree bend where a partial reflection would occur, meaning it would reflect pressure waves if the pressure is fixed in the simulations. However this is not something that came into play when assumptions were made for the final simulations. It is a more important factor that this is the final point of symmetry for these three pipes. This means all three slits and pipes would need to be included in the CFD if the outlet is placed further downstream these pipes. Following this point the pipes continue until they meet at a manifold. These three pipe sections have different lengths, and are displayed in more detail later in section 5.4.

4.2.3 Moving walls

The lower wall in the volume upstream the slit is in contact with the turbine causing it to rotate at 600 rpm like the inner wall of the labyrinth seal. This can be modeled by introducing a moving wall boundary rotating at $62,83$ rad/s about the y-axis. This boundary is displayed in figure 4.6. The rotation is defined in the positive direction about the y-axis which is counterclockwise. It is not known whether this is the same rotational direction as the real case, but it will not affect the simulations due to symmetry. From the mechanical drawings it does not look like the entire lower surface is rotating, but it is defined to do so in the simulations for simplicity. The moving wall has a no-slip condition accounting for the friction. This means that the velocity adjacent to the wall is equal to the velocity of the wall.

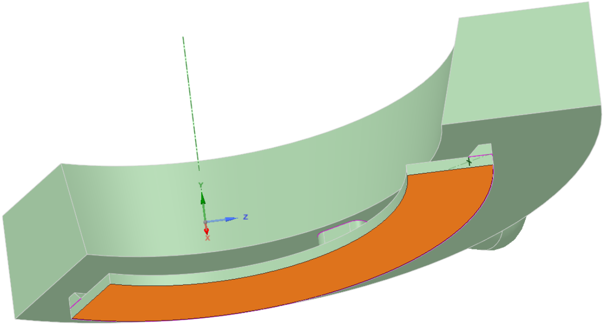

Figure 4.6: SpaceClaim model with the moving wall boundary marked in orange.

4.2.4 Rotational Symmetry

A symmetry condition needs by applied to some boundaries order to reduce the size of the domain to a third as previously discussed in section 4.1.1. Normally a symmetry condition mirrors the flow along the boundary, but that is not the correct boundary condition in this case. Instead a condition called rotational periodicity is used. This boundary ensures that the outflow on one boundary equals the inflow on the connected boundary, and the other way around. It is called a boundary interface which means two boundaries are connected. There are two such interfaces in this domain. One below the head cover upstream the slit, and another downstream the slit above the head cover. These boundaries are displayed in figure 4.7.

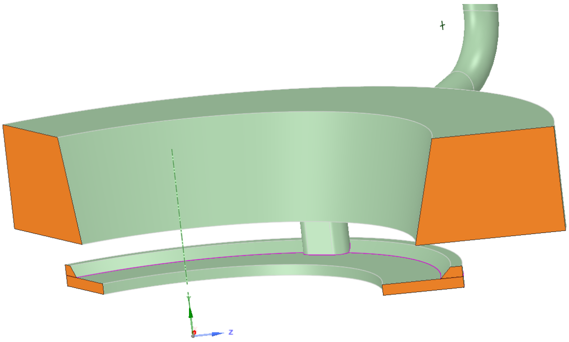

Figure 4.7: SpaceClaim model with the symmetry boundary marked in orange.

4.2.5 Stationary Walls

All the remaining boundaries in the domain are stationary walls. Most of these have a no-slip condition like the moving walls. Stationary boundaries with no-slip are displayed in figure 4.8. This means that the local velocity is zero adjacent to the wall. The side walls on the inlet displayed in figure 4.4 have a free slip condition. This is only an imaginary condition made to ensure uniform flow exits the inlet. Alternatively these could be removed by defining the inlet directly on the lower surface of the upstream volume.

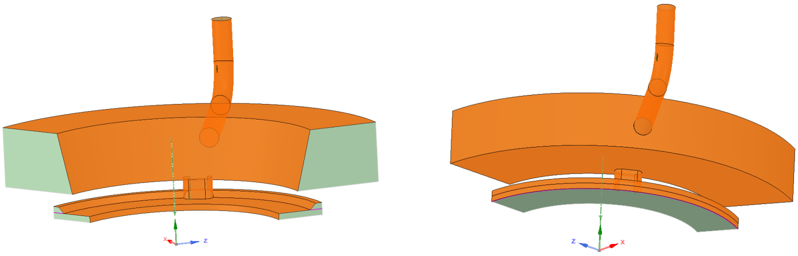

Figure 4.8: SpaceClaim model with stationary wall boundaries marked in orange.

4.3 Simplifications

It is going to be difficult to simulate this case accurately using both the real geometry and realistic boundary conditions. This is because of the complex flow field with very high velocities in confined space causing high Reynolds numbers, which means the flow is highly turbulent. These complex flow fields require a large spacial resolution to simulate accurately. This would take a long time to simulate, maybe even longer than the 20 weeks available in this study. As such it is vital to make good simplifications to the domain in order to optimise the ratio between accuracy and simulation time. The target will be to run simulations that takes 2-3 weeks or less, and everything above that is assumed to be unrealistic in this study. This target is set so that it is possible to redo simulations when mistakes are made.

4.3.1 Volume reduction

Below head cover

The first simplification that was considered in this study is to further reduce the $120°$ slice that is included in the domain as displayed in figure 4.9. This would lead to a reduction in volume in the domain leading to a large reduction in number of cells. Finally this simplification would lead to faster simulations without losing accuracy. Firstly this simplification was investigated on the volume below the head cover. The argument for the simplification on this volume is that the interesting effects happens near the slit and the rotating flow in the rest of the volume is nearly constant. This could be accounted for in ANSYS by introducing a delay in the rotation translation boundary corresponding with the time the water travels this distance.

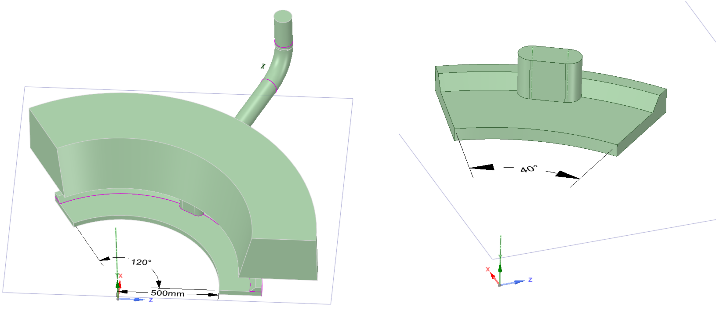

(a) Figure 4.2

(b) Illustration of suggested reduction in volume below the head cover.

Figure 4.9: Comparison between original domain and suggested simplification. $40°$ is only used as an example for the reduction.

However there is one major concern regarding this simplification on the area below the head cover. This is the fact that the inlet from the labyrinth seal is stretched around the entire volume. A reduction from $120°$ to $40°$ would mean that the inlet area is reduced to a third, meaning that the velocity will be tripled on the inlet in order to maintain the same flow rate. Another option is to have $\frac{2}{3}$ of the flux enter on the rotational boundary but that is considered to change the flow field drastically and will not be considered.

The only possibility of introducing this simplification on this volume is if the water does not enter the inlet uniformly. If instead most of the water enter near the slit a smaller part of the flux could be introduced on the rotational boundary. In order to test this possibility a CFX simulation was done as a pre study on a coarse mesh. An incompressible simulation was run in steady state from the inlet to the outlet of the slit as shown in figure 4.10. The inlet was set to constant total pressure based on the rotational velocities at the inlet. The outlet was set at a constant mass flow rate of $29,94$ kg/s equaling 30 L/s with a constant density of 998 kg/m^3.

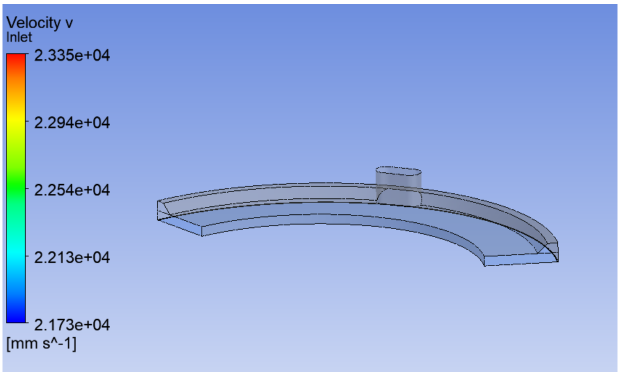

Figure 4.10: Display of the domain from the first pre study simulation with local velocity scale on the inlet displayed on the left.

This simulation converged well with residuals below $5e-5$ for all variables as shown in figure C.28. The goal is to investigate the distribution of fluxes on the inlet. This is done by looking at the velocity distribution on the inlet boundary. Plotting local fluxes on the boundary is harder as they cannot be defined in singular points. Since the area is constant, flux distributions can be investigated by only looking at velocities. This study was done at an early stage when 30 L/s was thought to be the flow rate, but the difference in flow rates is assumed to only have a negligible effect on the inlet flow distribution. The results show that the differences in inlet velocities are small on the boundary ranging from 21.7 m/s to

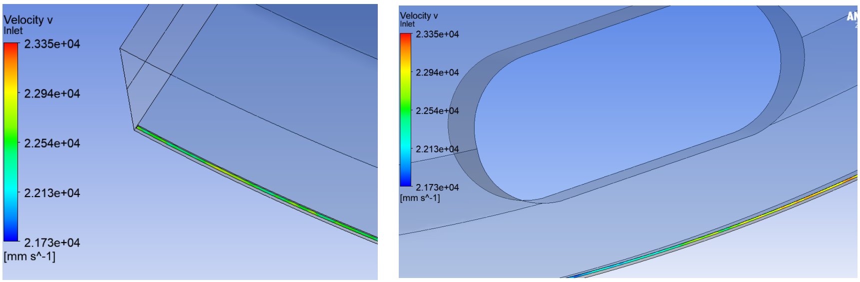

Figure 4.11: Display of velocities on the inlet boundary at the edge and center below the slit.

23.4 m/s with both low and high peak values appearing in the middle as shown in figure 4.11. This means that the volume reduction simplification is not possible for the area below the slit.

Above head cover

It was also considered to reduce the volume downstream the slit in the volume above the head cover as displayed in figure 4.12. All walls are stationary in this area and thus no external forces are influencing the flow field. Another pre study was done in this volume in order to determine if there are circulations through the entire volume, or if the flow is just proceeding the shortest route to the outlet.

The pre study was done in CFX on the entire initial domain with the outlet placed 200 mm down the pipe. Inlet and outlet conditions are the same as for the pre study below the head cover. Planes were constructed in CFD post at every 10 degrees of the volume from one rotational boundary to the other as displayed in figure 4.13. The goal is to measure the flux in all these planes to see if there is a rotational movement throughout the domain, and see how large portion of the volume that would need to be included in the final simulations. Another goal is to get a rough estimate of the size of these fluxes in order to determine whether they can be neglected or not. Table 4.1 lists the measured volumetric flow rates through these planes.

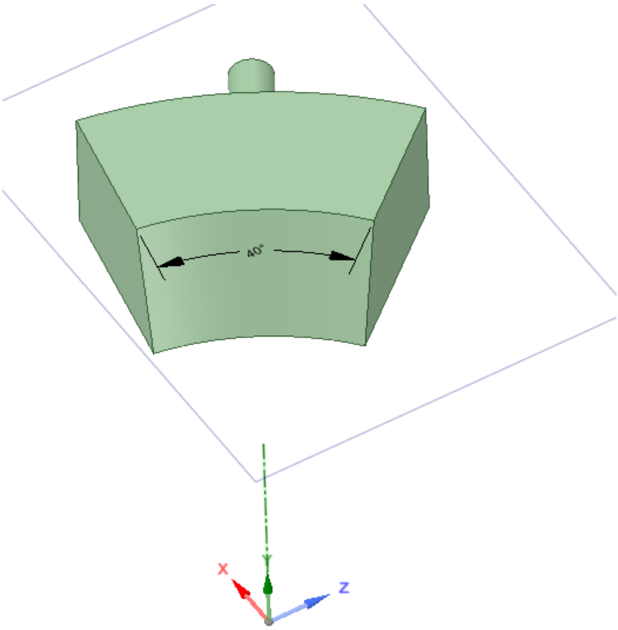

Figure 4.12: Display of suggested volume reduction above the head cover. 40° is again only used as an example.

Degrees	**Area** $[e^{-2}m^2]$	**Average Velocity** [m/s]	**Volumetric Flow Rate** [L/s]
0°	9.68	0.124	12.0
10°	9.68	0.123	11.9
20°	9.68	0.123	11.9
30°	9.68	0.123	11.9
40°	9.68	0.123	11.9
50°	9.68	0.123	11.9
60°	9.73	0.276	26.9
70°	9.68	0.123	11.9
80°	9.68	0.123	11.9
90°	9.68	0.123	11.9
100°	9.68	0.123	11.9
110°	9.68	0.123	11.9

Table 4.1: Flux through the planes from the simplification pre study above the head cover.

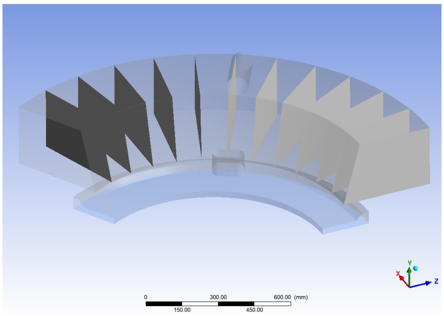

Figure 4.13: Display of the planes used in the pre study.

The total flux is approximately constant for all planes except the middle plane where the activity is higher. This indicates that a significant part of the fluid is circulating through the volume. The average velocities is similar, but it is still hard to make this simplification. This is because it is only the mean of the flow that is equal through these planes. A more detailed look at the velocities indicates that there are a lot of small local circulations in this volume. The effect of these circulations can be lost by adding a time delay on the rotational interface based on the average velocity. Figure 4.14 compares the flow field in the planes at 30 and 90 degrees which would be the symmetry interface if 30 degrees was removed at each end. Some differences between the planes can be seen. For example the velocities near the walls are higher at 90 degrees. These differences would disappear if this simplification was made. Because of this the volume above the head cover was not reduced.

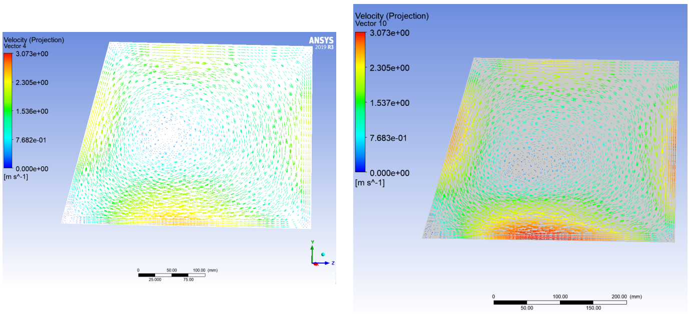

Figure 4.14: Vector plot of tangential velocities in planes at 30 degrees and 90 degrees respectively. The planes are used as examples.

4.3.2 Inlet simplification

After determining that volume reduction in the tangential direction would not be possible for this case, some attempts were made to simulate on this domain. They were unsuccessful largely due to instabilities when running the compressible model discussed in section 2.2.3. There were several possible reasons for these problems and several more drastic simplification needed to be made in order to compensate for these issues.

The first and most drastic change to the model is to remove the inlet from the $0,75$ mm gap in the labyrinth seal and rather have the water enter from the entire bottom surface. This will change the inlet velocity in the axial direction normal to the surface from 43 m/s to $0,18$ m/s. It also means that the small cell size of $0,75$ mm on the inlet is no longer necessary. Both of these effects helps reduce the Courant number and thereby increase stability.

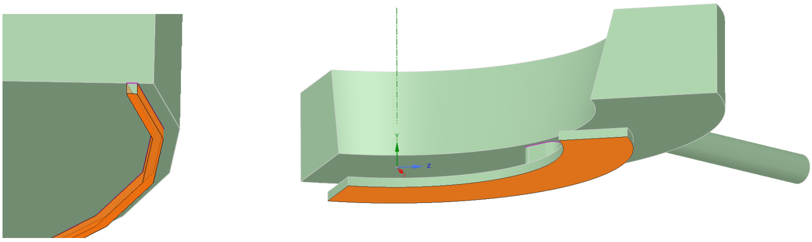

(a) Figure 4.4 b)

(b) Location of the inlet boundary marked in orange on the simplified domain.

Figure 4.15: Display of inlet boundary before and after simplifications.

This simplification also has a positive effect on reducing the mesh size. Figures 4.16 and 4.17 display the mesh before and after simplifying the inlet. With comparable local face sizes being used in both meshes the mesh size is reduced by around 30% after the simplifications were made. This number also includes the other simplifications to come later in this section. Later in the study it became apparent that the mesh size needed to be increased substantially from these two examples, but the mesh size in the simplified domain will still be reduced by a similar percentage for finer meshes if all local face sizes are reduced by the same factor.

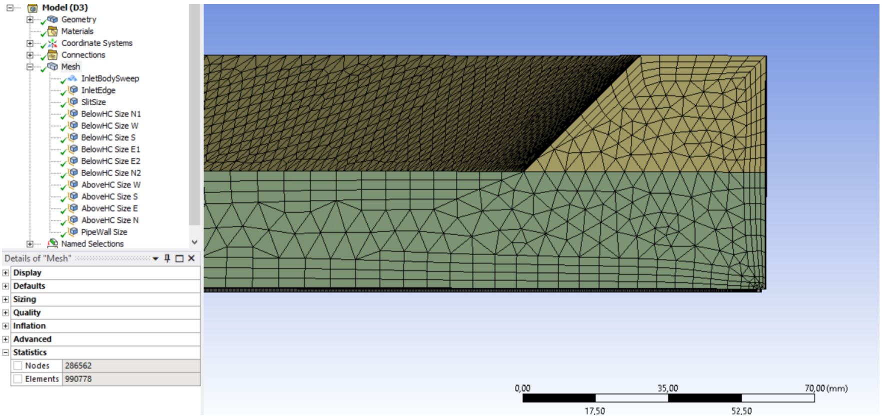

Nodes 286562
Elements 990778

Figure 4.16: Display of mesh near the inlet before simplification with number of cells shown as 990.778 in the lower left corner.

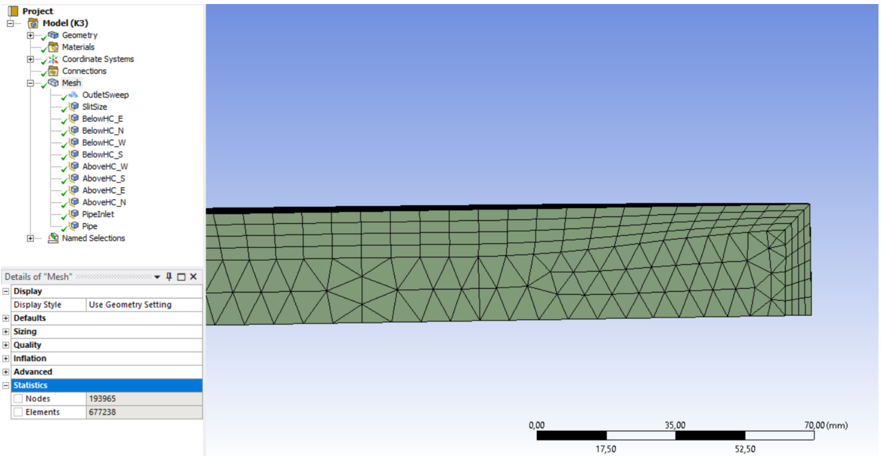

Display Style: Use Geometry Setting
Nodes 193965
Elements 677238

Figure 4.17: Display of mesh near the inlet after the simplification with number of cells shown as 677.238 in the lower left corner.

This simplification means that the domain does not include a moving wall boundary on the lower surface but instead have a tangential inlet velocity at the same angular velocity as the moving wall. A change in velocity profile occurs with this change in boundary condition. For a turbulent internal flow the velocity profiles will be of the form displayed in figure 4.18. In addition the high velocities of the flow exiting the slit is eliminated with this simplification. This is a significant change to the flow field upstream the slit, and might have an effect on the results. As such the focus of the simulations will be the establish the effects from the rotating flow.

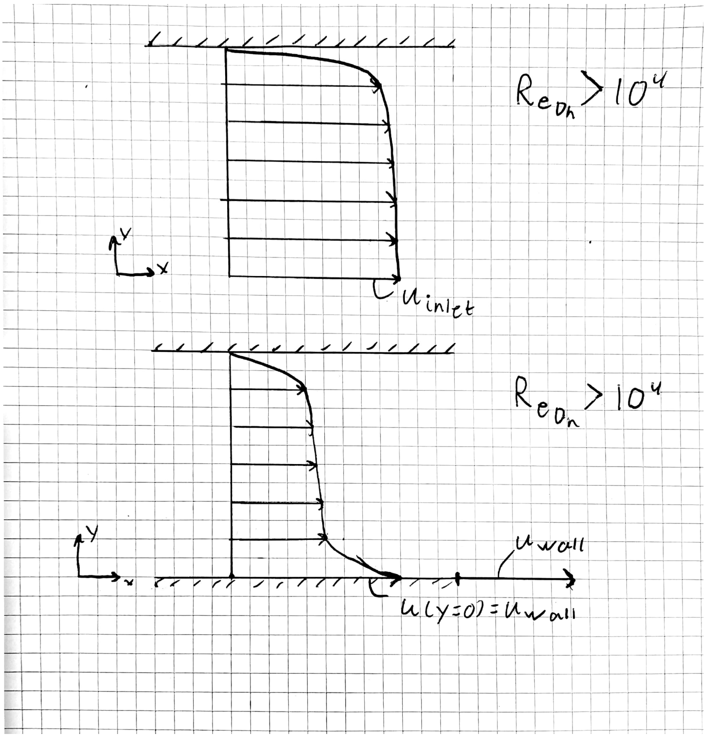

Figure 4.18: Hand drawing of the difference between the velocity profiles below the head cover before and after simplifications were made. The upper case is with the simplified inlet, and the lower is before the simplifications.

4.3.3 Constant height below the head cover

Another simplification that has been made is to remove the section with increased height from the volume below the head cover as displayed in figure 4.19. This area is not believed to influence the flow through the slit as much after the change in the inlet, because the inlet is spread throughout the domain. Additionally there has been some issues in this area in relation to the meshing. A lot of highly skewed cells appeared in this area as shown in figure 4.20. It is not beneficial to have many low quality cells in the same area as that will lead to local instabilities. The average quality of the cells upstream the slits increase after this simplification.

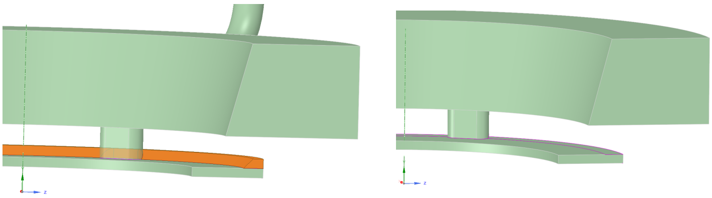

Figure 4.19: Display of domain before and after the increased height section was removed. The removed part is marked in orange on the left figure.

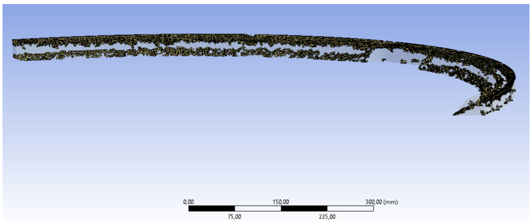

Figure 4.20: Cells with higher than 0.5 skewness from mesh in figure 4.16

4.3.4 Straightening the outlet pipe

The final simplification in this chapter was to straighten the outlet pipe as shown in figure 4.21. This done mainly because of issues with the mesh like in 4.3.3. The pipe geometry is simple compared to other sections of the domain. As such it is the only section that is considered to be sweepable which means that hexahedral cells can be used and repeated in the same pattern trough the entire volume. This is beneficial because hexahedral cells both score higher on the mesh quality parameters and reduce the required number of cells as previously discussed in section 3.3.3.

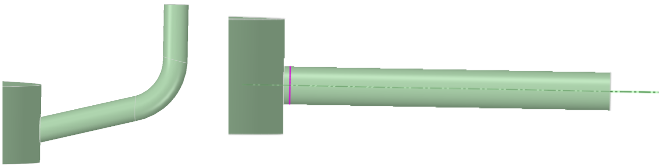

Figure 4.21: Display of outlet pipe before and after simplification.

However the bend is not sweepable and another cell structure needs to be applied to this section of the mesh. In the attempts to create a mesh on the initial domain this lead to poor quality on the cells in the bend section of the pipe. Like in the previous section, this part of the mesh contains a lot of cells with high skewness. Figure 4.22 shows all cells in the outlet pipe with skewness over $0,5$. Interestingly no such cells exist in the other sections of the outlet pipe where the sweep function was used.

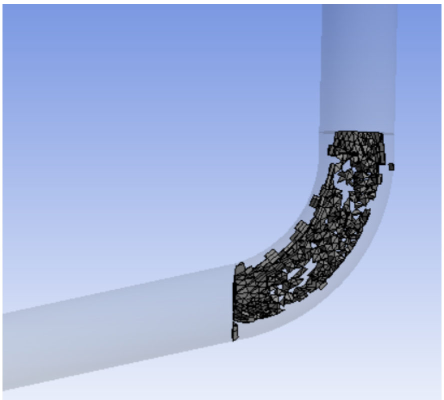

Figure 4.22: Cells with higher than 0.5 skewness from the curved pipe

There are also concerns regarding the smoothness in the transition between the bend and the vertical pipe, where the cells get rapidly smaller near the border, and then increase just as rapidly as shown in figure 4.23. This is happening in the flow direction meaning that it will have a large effect on the accuracy of the flow passing through this region. The bend in the pipe can have an effect on pressure pulsations in the pipe, because bends are elements that induce partial reflections. However this bend has a large radius of $180mm$ and is not going to affect the flow much. It is likely that the poor mesh elements in the area are going to affect the accuracy more than the simplification will.

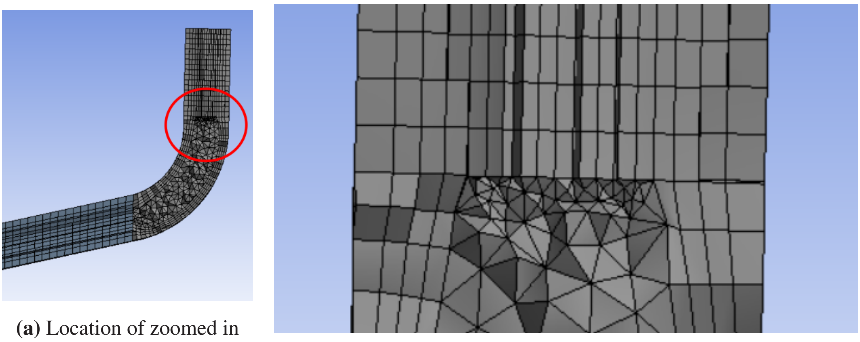

(a) Location of zoomed in section marked in red circle.

(b) Zoomed in view of section with smoothness issues.

Figure 4.23: Display of section of pipe outlet with poor smoothness values for the mesh.

The domain after all simplifications were made is displayed in figure 4.24. This domain will be used for all subsequent simulations.

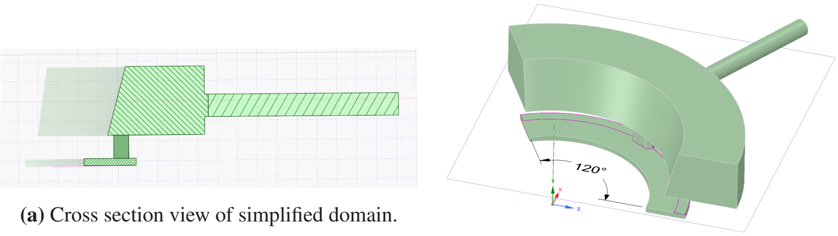

(a) Cross section view of simplified domain.

(b) 3D view of simplified domain.

Figure 4.24: Display of the SpaceClaim model after all simplifications were made.

4.4 Mesh

4.4.1 Mesh Refinement

During this study seven different meshes were made on the final simplified domain. These meshes has been numbered based on which order they were made, and their refinement properties will be tabulated in this section. Transient simulations were only done on two of these meshes, and the remaining meshes have been used as a part of a mesh convergence study. Transient simulations were run on one of the courser meshes, but there were some issues that lead to poor accuracy. Several meshes were made with improvements based on the experience acquired from the first simulations. Finally a mesh was chosen based on having the ratio between from the seven options convergence and simulation time.

Local Sizing

ANSYS meshing will create the mesh based on instructions from the user, but it is hard to control all the details of the mesh. As previously mentioned in section 4.3.4 only the straight outlet pipe is sweepable and the rest needs to be constructed using an unstructured mesh. One way to refine the mesh is to apply local sizing at different faces of the domain. This means that a length scale is defined as a preferred size on the face of the wall for the cells in contact with this boundary. The faces with local size instructions are displayed and numbered in figure 4.25. Faces below the head cover are referenced as BHC, while above the head cover is AHC. N, E, S, W subscripts define which side of the volume a face is on, and east is defined as the direction the outlet pipe is pointing.

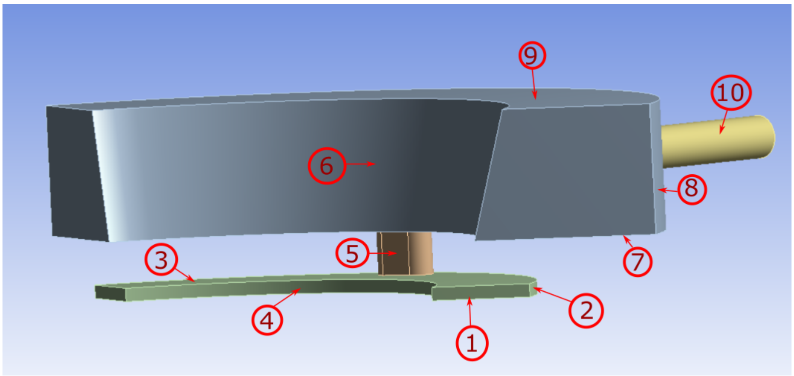

Figure 4.25: Numbered faces used for refinement of the mesh.

The local sizing helps control the cells near the boundaries, but does not affect the cells in the volume inside as much. Growth rate is used to govern how fast the cells grow inside the volume and is related to the smoothness parameter discussed in chapter 3.3.2. This value can be defined as part of the local sizing on the wall, as well as within the entire domain. There is a global sizing on the entire domain which is in the region of the maximum local wall size. A restrictive growth rate is used to ensure that the global size is only reached in intended parts of the mesh. The local growth rate is used to ensure a smooth increase in cell size from a wall with a smaller local cell size, to a larger local cell size.

Face No.	**Mesh 1** [mm]	**Mesh 2** [mm]	**Mesh 3-5** [mm]	**Mesh 6** [mm]	**Mesh 7** [mm]
1. BHC_S	11	7.5	5	7.5	5
2. BHC_E	7.5	5	3	4.5	3
3. BHC_N	11	7.5	5	7.5	5
4. BHC_W	15	10	7	10.5	7
5. $Slit$	6	4	2	3	2
6. AHC_W	22.5	15	7.5	11	5
7. AHC_S	30	20	10	15	7.5
8. AHC_E	37.5	25	12.5	19	10
9. AHC_N	30	20	10	15	7.5
10. $Pipe$	12	10	5	7.5	5
Global	37.5	20	12.5	19	7.5

Table 4.2: Cell size restrictions in the seven different meshes.

Face No. 6. AHC_W	1. BHC_S 7. AHC_S	2. BHC_E 8. AHC_E	3. BHC_N 9. AHC_N	4. BHC_W 10. $Pipe$	5. $Slit$ Global
Growth Rate	1.01	1.05	1.01	1.05	1.05
1.05	1.02	1.05	1.02	1.05	1.05

Table 4.3: Growth rates on the meshes. All meshes have the same settings for growth rates.

Bodies

Sometimes several mesh instructions conflict with each other. The user can influence which instructions are prioritised by dividing the domain into different bodies. A worksheet can be defined such that the user can decide on which order the mesh software should produce the mesh. This means that if the slit is defined as a body, it can be meshed first without being interrupted by instructions that apply to other bodies. Then the mesh around the shared faces between bodies adapts to the restrictions put on the body that was meshed first. The domain was divided into four bodies for this simulation which is displayed in figure 4.26. Worksheets were only used for mesh 1 and 2, while the meshing order was program controlled for the remaining meshes. The domain was divided into two bodies in mesh 3-7 with the outlet pipe being separated from the rest of the domain. This allows the use of hexahedral cells in the pipe which increase the cell quality in the area. The skewness of the cells on the outlet pipe for mesh 4 is displayed in figure 4.27. These values are very good compared to the skewness of the rest of the mesh which is displayed in appendix C.5 figure C.86.

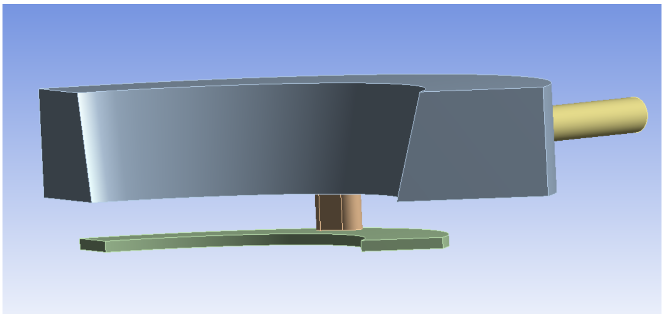

Figure 4.26: Display of the four bodies divided into different colors. In prioritised order the slit is orange, below head cover is green, outlet pipe is yellow and above head cover is blue.

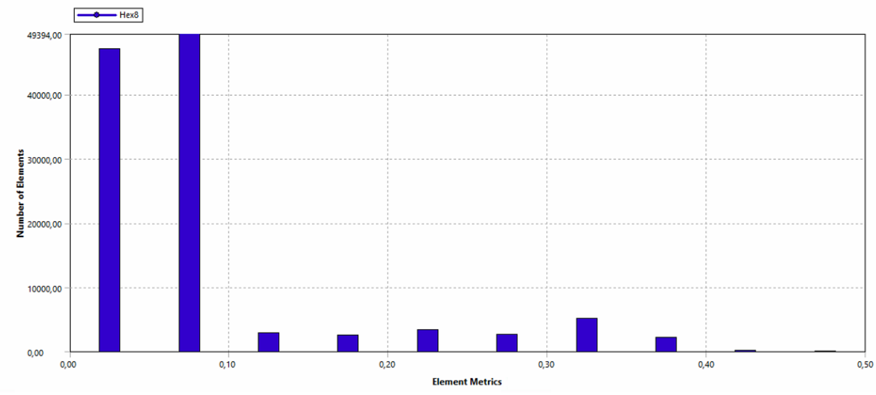

Figure 4.27: Skewness values of the cells on the outlet pipe using data from mesh 4.

Inflation Layer

The final mesh refinement tool that is used is inflation layers. Inflation layers increase the resolution and change the shape of the cells closest to the wall. This tool can be used to control how many cells are in the boundary layer, and the location of the closest cell to the wall which can be used to tune yPlus values. For the initial simulations program controlled inflation layers were defined using Smooth Transition with maximum layers and growth rate. The yplus values was checked by running a steady state simulation on Mesh 2 plotting yPlus on the walls as displayed in figure 4.28.

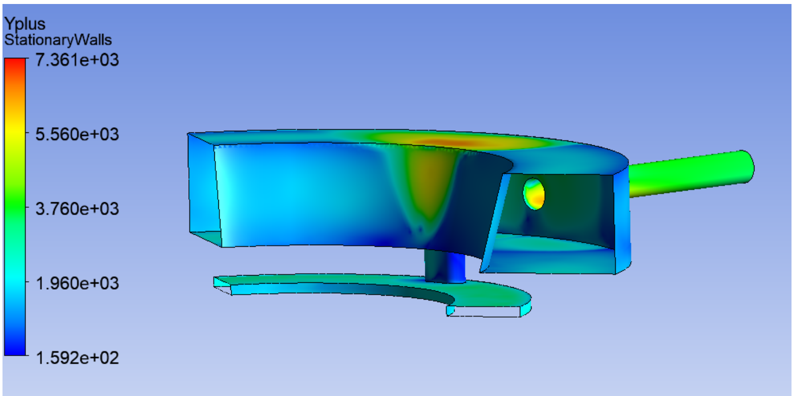

Figure 4.28: Yplus plot on the walls for steady state simulation of mesh 2.

These yPlus values are very high ranging from 150-7000, which means that the entire boundary layer is resolved within one cell for most of the walls. That is not satisfactory, and this mesh will not be able to capture the vortex shedding in the slit. As such the inflation layer resolution was increased drastically, and first layer thickness was used to define the size of the cells closest to the wall in subsequent meshes. The growth rate within the inflation layer is set to 1.2, which is the maximum smoothness limit as discussed in section 3.3.2. This means that the outer cells in the inflation layer is as close to the free stream mesh in size as possible, minimizing the smoothness issues in this area.

There was some issues that occurred when the mesh program created the inflation layers for all seven meshes. The issue occurs when trying to apply an inflation layer around a sharp edge as shown in figure 4.29. A diagonal cut occurs near sharp edges, and these location has cells with very sharp angles. This is especially a problem for the finer meshes (Mesh 3-7) where the inflation layer resolution is very high. These cells will have skewness values close to 1 which is the maximum and that is not acceptable. In fact this was such a large stability issue for the initialisation of the mesh displayed in figure 4.29 that the simulation crashed after only a few iterations.

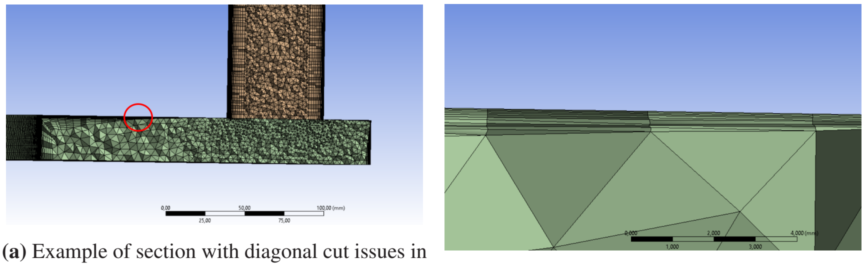

(a) Example of section with diagonal cut issues in the inflation layer marked in red.

(b) Zoomed in view of the cells in the area.

Figure 4.29: Location of diagonal cut issues. This is not one of the final seven meshes.

If a worksheet is used to define the meshing order, additional issues occur related to the inflation layer. In figure 4.30 a case where the slit was meshed first is displayed. That lead to the inflation layer being created as planned in the slit, but the other bodies get diagonal cuts. This is not satisfactory either due to high skewness in the cells bordering the inflation layer cells. Due to this issue worksheets were not used to control the meshing for mesh 3-7.

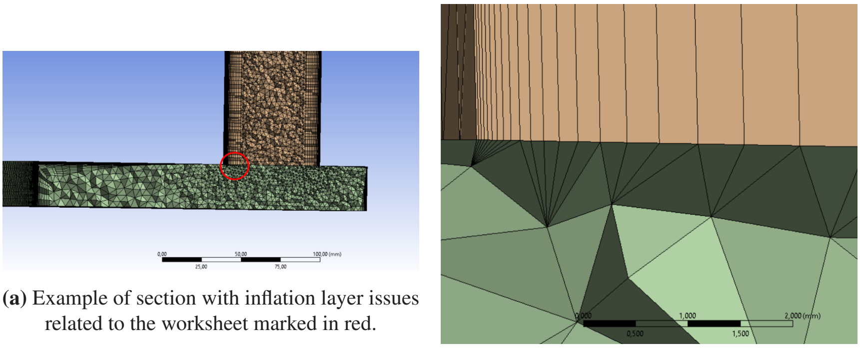

(a) Example of section with inflation layer issues related to the worksheet marked in red.

(b) Zoomed in view of the cells in the area.

Figure 4.30: Location of worksheet issues in the inflation layer.

In order to work around these issues another simplification was made to the geometry. A rounded of edge was created at the bottom and top of the slit. The inflation layer was created as intended in between the AHC volume and the outlet pipe initially, so the simplification is not applied here. This feature is not a part of the real geometry, and is only present to aid the meshing software. As such it is desired to have as small of a round of radius as possible. This is especially important because of the effects rounded off edges can have on the frequencies and amplitude of the vortex shedding as discussed in section 2.1.1. The effects of the round of radius on the inflation layers is displayed in figure 4.31.

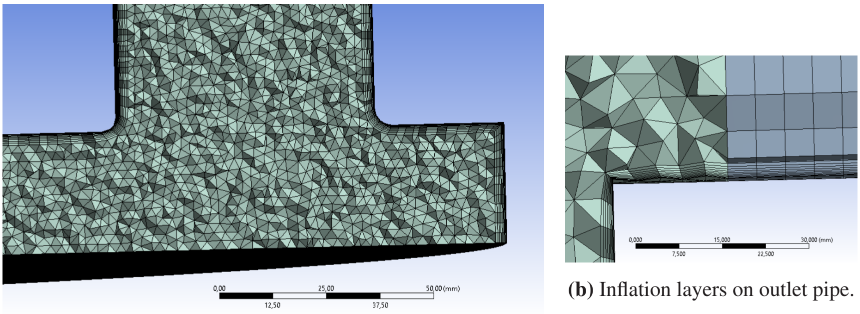

(a) Inflation layers on the slit inlet from Mesh 3.

(b) Inflation layers on outlet pipe.

Figure 4.31: Inflation layers around edges in the geometry. Mesh 3 is used as an example, but the same shape is used for Mesh 3-7.

However this after this simplification another meshing parameter had a substantial impact. That was the curvature minimum size. This parameter decides how small cells should be used to capture curved geometry. Initially a round of radius of 1 mm was suggested, which is smaller than the cells in the area. This means that the cell size in the slit openings was forced down in order to capture the curve leading to a mesh with well over 100 million cells. As such the round of radius was increased to 4 mm so that the curvature min size could be set around 2 mm which is the same as the cell size on the faces in the area. 2 mm is not enough to get a smooth round of radius, but that is not considered to be important as this is only an imaginary geometric feature. The only thing to keep in mind is that the low curve resolution does not lead to roughness along the circumference of the slit openings. This did not happen for curvature min sizes of 2 mm or less.

All mesh properties related to the inflation layers is tabulated in 4.4. Inflation layers are defined globally for all meshes to ensure a smooth transition between the different sections in the geometry. This might cause smoothness issues between the outer cells in the inflation layer and first cells in the free stream due to a large jump in size in some directions. However this jump is perpendicular to the flow direction close to the wall so there is not expected to be any large velocity components through this transition region in the mesh.

Mesh No.	**IO**	**TR**	**FLT** [mm]	**Max layers**	**GR**	**CS** [mm]
Mesh 1	ST	0.4	-	2	1.05	-
Mesh 2	ST	0.4	-	4	1.05	-
Mesh 3	FLT	-	0.1	10	1.2	2
Mesh 4	FLT	-	0.1	10	1.2	1.5
Mesh 5	FLT	-	0.1	10	1.2	2.5
Mesh 6	FLT	-	0.2	8	1.2	3
Mesh 7	FLT	-	0.1	15	1.2	1.25

Table 4.4: Mesh settings related to inflation layers. Abbreviations have been made for the table to fit on the page. IO=Inflation option, TR=Transition Ratio, FLT=First Layer Thickness, GR=Growth Rate, CS=Curvature minimum size, ST=Smooth Transition.

4.4.2 Mesh convergence study

A mesh convergence study, also known as a mesh dependency study, was performed as a part of the process in creating a mesh for the CFD simulation. It is also used as a part of the verification process which was discussed previously in section 3.6.1. This study looks at the how values of different properties change with the mesh size. Mesh sizes are tabulated using the number of cells in table 4.5. The number of cells is not the only important factor when considering mesh dependency. It is also important where the increase in cells is done, and which effects it has on the mesh quality parameters. Information on which changes has been done to increase the number of cells is found in the tables from the previous subsection. If the mesh quality is comparable it is safe to assume that the accuracy of the numerical model increase with increasing cell size.

Mesh No.	Mesh 1	Mesh 2	Mesh 6
Mesh 5	Mesh 3	Mesh 4	Mesh 7
No. of cells	$387,612$	$677,238$	$6,069,852$
$9,321,491$	$12,182,953$	$17,503,142$	$22,172,198$

Table 4.5: Number of cells in the different meshes ordered by mesh size from smallest to largest.

Simulating all seven meshes with transient boundary conditions is too time consuming. As such it is decided that the mesh convergence study will be performed in steady state. According to the hypothesis from Rainpower, which was presented in section 1.1, it is expected that transient effects will occur in the slit. This will make steady state convergence complicated for meshes that are able to capture these effects.

Monitor points, which monitor the gauge pressure, have been defined and used on the different steps of the CFD study. The locations of these points are presented in appendix C.1. Some of these were used to monitor the difference between the steady state values of the seven different meshes. Convergence was investigated for the maximum measured pressure in the slit at point 3, minimum measured pressure in the slit at point 12, maximum measured pressure in the pipe at point 13 and minimum measured pressure in the pipe at point 14. These monitor points were chosen because pressure is the most important parameter in this study, and these points covers the convergence at the maximum and minimum pressures.

The convergence of monitor point 3 is displayed in figure 4.32. This point converge well with increasing mesh size. However the pressure oscillate with the number of iterations for the five meshes with highest mesh size. This is seen consistently for all monitor points in the slit for mesh 3-7. The raw data from the 500 last iterations of all monitor points is displayed in appendix C.4. This does not indicate that mesh 3-7 converge poorly compared to mesh 1-2. Residual convergence is comparable for all seven meshes. However the average convergence for the 500 last iterations seems to improve with the number of cells looking at the monitor point plots. It seems like the mean of the oscillations change less per iteration, than the measurements from the coarse meshes. The residuals are comparable because they are measured based on the oscillating values, which change at a comparable rate to the non oscillating values for mesh 1 and 2.

One possible reason that the oscillations occur is that the transient effects from vortex shedding in the slits appear with the increased cell resolution in the boundary layer. The amplitude of the oscillations is also in a realistic region compared to measured values from the Norconsult report, which will be presented in more detail in chapter 5. It also seems likely that the oscillations are caused by transients as the cell resolution is highest in the slit, and mesh quality is satisfactory in this region for mesh 3-7.

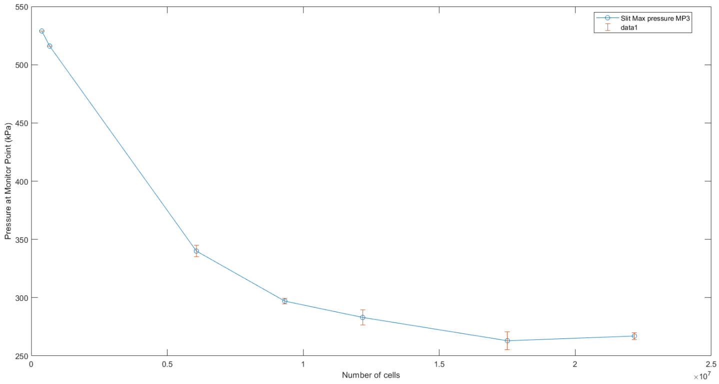

Figure 4.32: Mesh convergence for monitor point 3 which is the maximum pressure in the slit, from the points displayed in figure C.1. Amplitudes of the oscillations are presented with error bars.

The convergence of the minimum pressure point in the slit is presented in figure 4.33. The mean of this pressure value are converging well, but there is an outlayer for Mesh 3 at approximately 12 million cells. This is the point in the slit with the highest oscillating amplitude compared to the other 11 monitor points. The mesh quality in the region of the point does not indicate that there should be any large numerical errors here. Maximum pressure in the outlet pipe does not change much between the different meshes, and the minimum pressure converge well for mesh 5-7. These results are displayed in figure 4.34. The results in this region does not oscillate which is to be expected when the outlet boundary is at a fixed pressure.

Based on the results from this study the mesh dependency is satisfactory for Mesh 4 and Mesh 7. Mesh 3 also has satisfactory convergence for monitor points 3, 13 and 14, but will not be used because of the outlayer in monitor point 12. Mesh 4 will be used in this study as it has smaller mesh size, which will lead to a decrease in computational time compared to Mesh 7. As such only mesh 4 is considered in subsequent sections of the report.

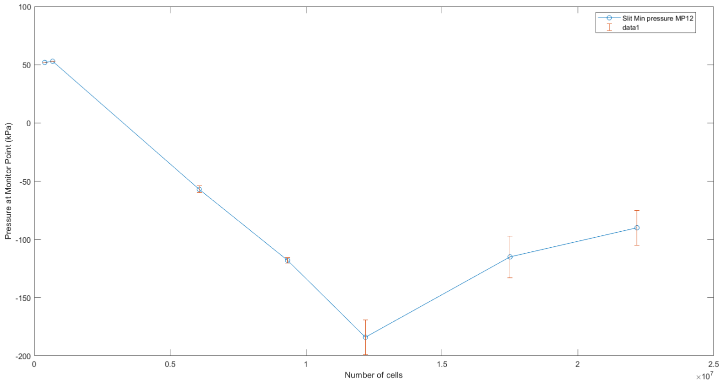

Figure 4.33: Mesh convergence for monitor point 12 which is the minimum pressure in the slit, from the points displayed in figure C.1. Amplitudes of the oscillations are presented with error bars.

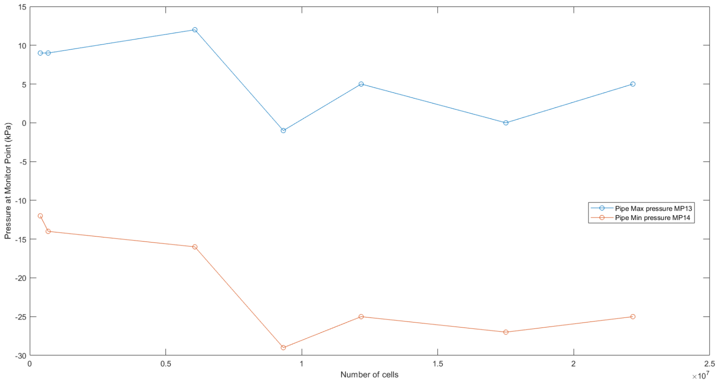

Figure 4.34: Mesh convergence for monitor points 13 and 14 which is the maximum and minimum pressure points in the outlet pipe, from the points in figure C.2

4.4.3 Mesh Quality

Mesh metric	Min	Max	Average	Standard Deviation
Skewness	0	0.867	0.193	0.111
Orthogonal Quality	0.133	1	0.806	0.111
Aspect Ratio	1.129	158.0	5.146	10.26

Table 4.6: Values for different mesh metrics from Mesh 4. The data is based on the mesh quality data presented in Appendix C.4.

The quality of the mesh which will be used in this simulation is measured using the metrics that are explained in detail in appendix A.2. These metrics are measured in ANSYS meshing for all cells in the mesh and tabulated in table 4.6. Smoothness is the only parameter discussed in this report that is not measured in the meshing software. The main problem regarding smoothness is the jump in size between the inflation and free stream cells normal to the wall which was previously discussed in the inflation layer part of section 4.4.1. All other metrics have satisfactory averages and standard deviations. However the max values are high for all three metrics. In order to determine if this is a problem, the number and location of these cells needs to be investigated.

The skewness is satisfactory for most of the cells. Figure 4.35 shows all cells with higher than 0.6 skewness. This is approximately $19,850$ cells which represents 0.113% of the total number of cells. These are spread throughout the domain with the only region with a high number of skewed cells being the inflation layer in the sharp corner of the AHC volume cover. This is not a big issue due to these cells being close to no slip walls, meaning that velocities are close to zero. The slit seems to have a low number of skewed cells compared to the rest of the domain, while the outlet pipe has no such cells.

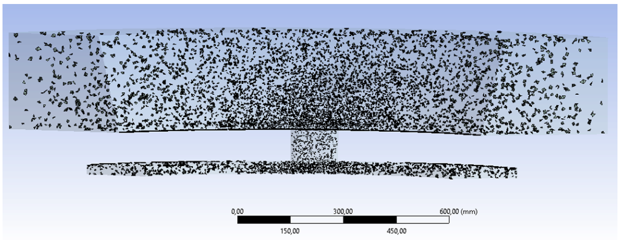

Figure 4.35: Display of all cells with higher than 0.6 skewness in the mesh.

Cells with poor orthogonal quality are spread across the domain like the cells with poor skewness. Figure 4.36 show the $20,850$ cells with lower than 0.4 orthogonal quality. This represents 0.191% of the total cells. In addition there are cells in the inflation layers on the pipe inlet with poor orthogonal quality as displayed in figure 4.37. This is to be expected because of the 90 degree sharp edge. A way to improve this would be to round of the edges of the pipe inlet, like it was done on the slit inlet and outlet and discussed in section 4.4.1. However since the cells in this area is much larger the round of radius needs to be increased substantially to be able to capture the curvature without reducing the cell size in the area. As such it was decided to rather use the sharp corner and accept orthogonal values of around 0.3-0.4 in the area.

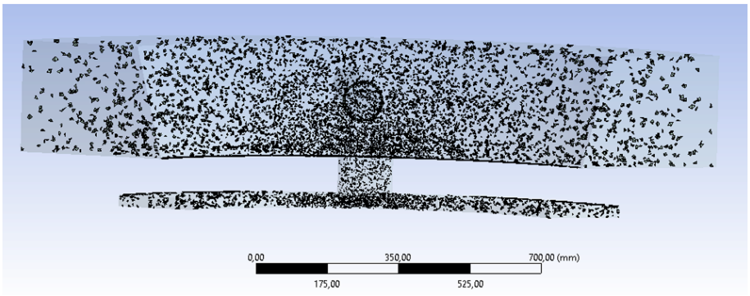

Figure 4.36: Display of all cells with lower than 0.4 orthogonal quality

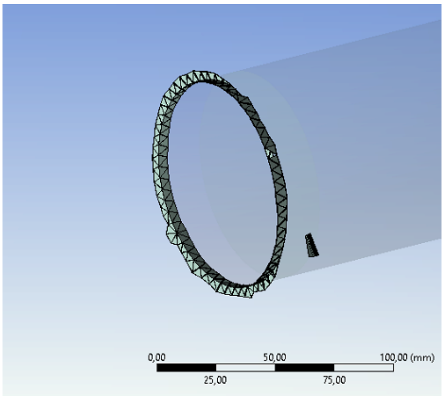

Figure 4.37: Cells with poor orthogonality on the pipe inlet.

Figure A.3 shows the $40,850$ cells with higher aspect ratio than 75. This represent 0.233% of the total cells. As expected these cells are placed in the inflation layers on the surfaces where the local cell size is largest. Aspect Ratios are going to be poor for the inner cells in the inflation layer. That is not going to be a big issue due to the no slip condition on the walls. This means that the velocity parallel to the wall is going to be smallest in the cells with the worst aspect ratio. There are no slip conditions on all the walls of the simplified domain as previously discussed in section 4.3.

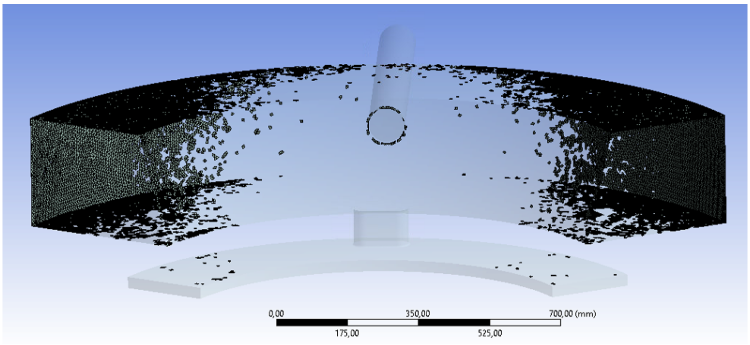

Figure 4.38: Display of all cells with higher than 75 aspect ratio

4.5 CFX Pre

4.5.1 Boundary Conditions

Inlet

The inlet boundary on the final domain has been discussed previously in this chapter. A velocity of 0.18 m/s is fixed normal to the inlet boundary in the axial direction. The area of the surface is approximately $0,266\ m^2$ which gives a flux of 47.9 L/s including round of errors from the velocity and area. There is also a fixed tangential velocity parallel to the inlet surface to drive the 600 rpm rotation of the water. This velocity is governed by (4.1) using $\omega = 62.83$ rad/s and $r = \sqrt{x^2 + z^2}$.

$$v_\theta = \omega * r \tag{4.1}$$

Outlet

In this simulation the outlet condition is defined with a pressure condition. A varying pressure condition is used on the outlet based on the measurements done at Torpa power plant. High vibrational values was measured at measurement point P41, which is shown in figure 5.3. This is a point in the slit water pipe system downstream the outlet boundary. Between the measurement point and the outlet of the CFD domain there are three pipes of different lengths which meet at a manifold and proceed as one pipe with larger diameter. Measurement point P41 is located 5.7 m downstream this pipe. This pipe system will be explained in more detail in chapter 5.

Since there is a distance between the measurement point and the outlet boundary it is hard to predict how the amplitude and frequency for the measured vibrations change between these points. The best approximation that can be done, while only using the measurements at P41, is to assume that the amplitude and frequency is the same. Alternatively an interpolation can be made between measurement point P38 which is inside the domain and P41 based on the distance and the difference in amplitude. The problem here is that the amplitude most likely does not decrease evenly with the distance travelled, but rather decrease rapidly at certain points where hydraulic elements cause partial reflections. Such elements can be the pipe inlets, and the manifold for instance. It is also preferable to have an outlet condition that is not influenced directly by measurement point P38, which is going to be used as a validation point.

High pressure amplitudes was only seen at the runs on 19 MW, 37 MW and 47 MW without the air intake at measurement point P41. FFT values from these measurements are displayed in figures D.8 and D.9. All these measurements have peak amplitudes on the same frequency of approximately 36.5 Hz. The lower boundary of the operating conditions at Torpa power plant are 40%-50% of the full load. Full load is at 72.5 MW. This means that 19 MW is outside the operating conditions. As such it is decided to base the amplitude of the outlet pressure condition on the average of the amplitudes from the 37 MW and 47 MW runs. These amplitudes were 2.7 mH2O and 2.1 mH2O respectively. The outlet function was defined as a sine function (4.2) with an amplitude of 23.5 kPa and frequency of 36.5 Hz.

$$p = 23,5[kPa] * sin(36,5[Hz] * 2 * \pi * t) \tag{4.2}$$

Additionally the outlet is defined as an opening instead of an outlet in the program. This is done in order to allow back flow on the outlet boundary, which can occur when pressure waves hits the boundary and is reflected. If the boundary is defined as an outlet a wall will be created to prevent any backflow through the boundary. It is uncertain if this is something that comes into play for this simulation when there is a varying pressure condition on the outlet. However it is still used as there are no disadvantages to using the opening boundary condition compared to the outlet for this case.

The remaining boundaries are the rotational interfaces and stationary walls which is the same as the conditions in section 4.2 and is applied to the same surfaces of the model. Rotational translation of the rotation about the y-axis is present above and below the head cover, while all walls are defined using the no-slip condition.

4.5.2 Compressibility

The fluid in the simulation is water and for the transient simulation in this case it has assumed to be incompressible with a density of 998 kg/m^3. As previously discussed in section 2.2.3 a compressible fluid model has been shown to improve the accuracy in the studies done in [6] and [7]. One of the problems including the compressible model presented in 2.2.3 is that the Courant stability condition now needs to be fulfilled for the wave propagation speed which is in the range of $1200 - 1400$ m/s. The maximum velocity in the incompressible flow field is $44, 6$ m/s. Assuming a wave propagation speed of 1200 m/s this means that the maximum velocity in the simulation is increased 27 times from the incompressible case. This means that the timestep needs to be approximately 27 times smaller in order to achieve the same stability on the same mesh. Using mesh 4, the incompressible transient simulation had a maximum Courant number of 0.62 using a timestep of $5e - 6$ seconds. This simulation used 13 days and 11 hours to simulate 0.1 s on a computer with 12 processor cores. A timestep of approximately $2e - 7$ seconds is needed to achieve a stable acoustic simulation on the same mesh. Using the same computer on a acoustic simulation would take just under a year to complete. This is unrealistic within the restrictions of this master thesis study and the mesh size would need to be reduced significantly which also would reduce the accuracy substantially. It is likely that an incompressible simulation on a satisfactory mesh provides better results than compressible simulations on a poor mesh.

Some attempts were made simulating with a compressible model on mesh 2, but they has significant stability issues even for timesteps with maximum acoustic Courant number less than one. No stability issues were seen using identical conditions and mesh for an incompressible model. Mach numbers are small in all areas of the veloctiy field with the maximum being $M_{max} = 0.037$ again assuming a sound speed of 1200 m/s. This should be well outside regions were compressible effects starts to occur. The mach numbers in the cases in [6] and [7] might be higher because the flow rates are much higher in the turbine than in the slit water system. Considering all these arguments, the compressible model was not used in this study.

The water is also assumed to have a constant temperature of $25°C$. In reality the water is colder and varies with the time of year, but the differences with temperature for the relevant properties in this case are small. Constant temperature is a reasonable assumption for water as a fluid as it has a high heat capacity which was previously discussed in chapter 2.

4.5.3 Turbulence Model

The turbulence model is set to Shear Stress Transport which was previously discussed in section 3.5. This is done to utilise the program controlled switching between $k - \epsilon$ and $k - \omega$ throughout the domain. One advantage of using this model is that good stability from the turbulence calculations is ensured, but at the same time it is hard to control exactly which turbulence model is used where. For this case where a combination k-omega and k-epsilon is needed to provide the best accuracy this model is a natural first choice.

4.5.4 Transient settings

The second order Backward Euler is used as the transient scheme in this simulation. This is done to remove the diffusion errors that can occur using the first order Backward Euler, which was previously discussed in section 3.4.3. Because this is a second order scheme the accuracy of the jump between the time step is increased. Total simulation time has been set to 0.1 seconds which is between three and four periods for the frequency set on the outlet boundary at 36.5 Hz. This means that frequencies lower than 10 Hz cannot be captured in the results of this CFD simulation. No amplitude peaks were measured below 20 Hz at any of the measurements in appendix D.1 which includes both measurement point P38 and P41, so this limitation should not filter out any real frequencies. The timestep is $5\mu s$.

4.5.5 Solver Control settings

High resolution, which was previously discussed in section 3.4.2, is used as the advection scheme in this simulation. This is used because the program controlled switch between first and second order schemes improving the ratio between simulation time and accuracy. It is hard to control which scheme is used where. This might lead to some unwanted diffusion errors from the first order scheme. However CFX is a renowned CFD software which has been used numerous times in similar research and as such it is assumed that the program will handle the switching in a satisfactory way. For increased accuracy the second order scheme could be used for the entire domain, but it would lead to an increase in computational time.

The convergence control is set using a residual convergence limit and maximum number of iterations per timestep. A RMS limit has been set to $1e - 4$ which is the default value in the program. This is a little high for the RMS and the time steps should ideally converge to a lower value. As previously mentioned this simulation lasted 13 days and 11 hours which could roughly be calculated in advance. If a stricter residual limit was set, there could easily have been 2-3 times more iterations per timestep meaning the simulation time would be 2-3 times longer. When this simulation was started there was not enough time until the deadline to be able to complete a simulation with stricter residuals. However as seen in the residual plots in figures C.4 and C.5 the values converged well below this limit in the transient simulations. All momentum and mass values converged to below $1e-5$ for the RMS values, with the pressure converging below $1e-6$. The maximum pressure residual was $1e-4$. This is a large improvement compared to the steady state initialisation which is displayed on the first 1000 iteration in the residual plots.

The minimum iterations were set to 1 and maximum was set to 20. All timesteps were converged in far less than 20 iterations. If there was more time the minimum iterations could be increased to 3-5 to improve the convergence further, but for the purposes of this master thesis study the residual convergence is satisfactory. All remaining settings in CFX-Pre is set to the default values.

Chapter V

Measurement Data Analysis

■ The measurements that were done at Torpa is analysed in this chapter. It starts with a presentation on the work that has been done by Norconsult at Torpa. The location of the measurement points are displayed, and some concerns related to the placement of P38 has been discussed. This point might unintentionally work as a low pass filter due to its placement, but it is uncertain which frequencies can be trusted. The results of the measurements are presented with FFT plots in Appendix D and discussed in this chapter. Finally resonance calculations have been done, comparing resonance frequencies to the measured frequencies. These comparisons are based on wave speed calculations that assume no air content in the water. Wave speeds that cause resonance at a frequency of $36.5Hz$ has also been calculated. No signs were found that there is resonance in the pipe system based on these assumptions, but a better estimate of the wave speeds at the plant is needed to make conclusions regarding resonance.

5.1 Vibrational Measurement at Torpa

The master thesis study in this report is supported by measurements that were made at Torpa by Norconsult in January 2014. These measurements were put together in a report. Relevant pages from this report is included in norwegian at the end of appendix D. This report stated that there were some high amplitude pressure pulsations measured in the slit water system which is the focus area in this study. The condition was graded 2 out of 4 with 1 indicating no issues, and 4 indicating that the plant needs to be shut down until the problem is fixed. No actions were recommended in this report for the slit water system. A summary of the relevant measurements is included in page 7 of the report and is also displayed in figure 5.1.

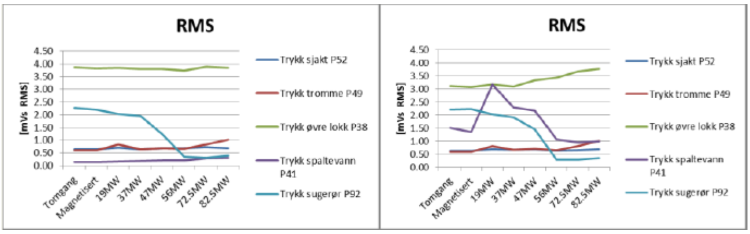

Figure 5.1: RMS pressure amplitudes in mH2O for measurements with and without air intake repsectively. Translation for comparison to fft plots in appendix D: Tomgang=idle run, Magnetisert=saturated.

These results show that the pressure amplitude are highest in measurement P38, named "Trykk øvre lokk" in norwegian, located in the volume above the head cover. Pressure pulsations was not reduced by using the air intake in this area, and actually showed a slight increase in RMS values. The measurements from the pipe system in P41, named "Trykk spaltevann" in norwegian, show a large reduction in RMS pressure with the use of air intake. The pressure amplitudes are high in the pipes for some of the operating conditions. Variations in pressure amplitudes are also very large for the different measurements without air intake at P41. Norconsult have provided FFT values from measurements at both P38 and P41 which has been plotted and listed in appendix D. These plots have been transformed from mH2O to kPa for simpler comparison with the CFD results. FFT-plots from P41 with air intake has not been included because the amplitudes are very low and don't need to be further analysed in this study.

5.2 Measurement Point Locations

5.2.1 P38

There were some misunderstandings throughout the thesis work between people involved, regarding the placement of measurement point P38. Einar Kobro who performed the measurements was able to clarify the placement of this measurement point in the fluid which is displayed in figure 5.2. The sensor is placed on the end of a thin pipe, and placed near the outlet of the slit. The pipe was threaded into the volume with the measuring device placed on the outside of the volume at the opposite end of the pipe. Rainpower has confirmed that the high pressure amplitudes measured at this point is an important part of the hypothesis they developed which is investigated in this study.

Some concerns were raised about the placement of this measurement point. The

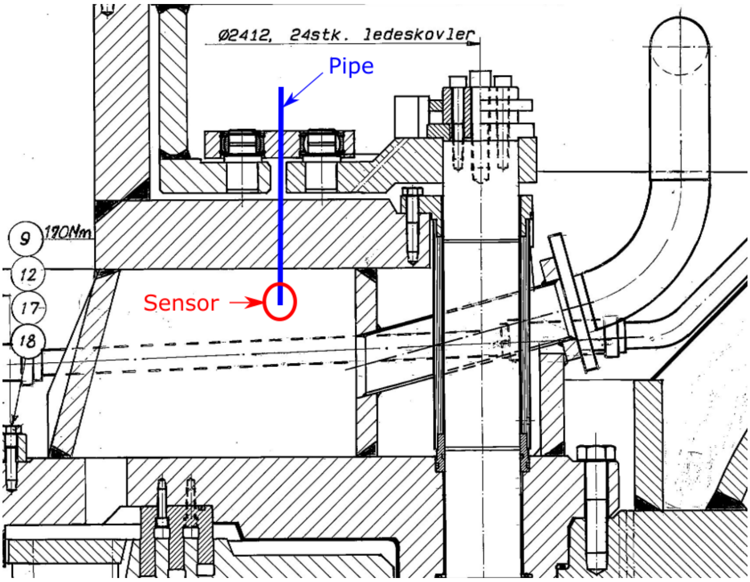

Figure 5.2: Location of measurement point P38 in the fluid, marked on the mechanical drawing from figure B.2.

placement of the sensor on the end of a long pipe will induce the effect of a low pass filter on the measurement unintentionally. A low pass filter means that frequencies higher than a certain limit is filtered out of the measurements [15]. It is not known what the frequency limit for the low pass filter in these measurements are. The work around for this issue is to look at the downstream measurement point and see which frequencies is seen at both measurement points. These are assumed to be trustworthy. If a frequency peak is measured at P41 but not seen at P38 for a high frequency it might be because this frequency has been filtered out. Additionally bubbles of air can accumulate on the long vertical pipe, also filtering out high frequencies. This effect could be dependent on the time of day that the measurements have been made, assuming that more bubbles have accumulated as time goes on after the sensor was placed. In order to be able to investigate these effects, the time schedule of the measurements are included in norwegian in appendix D.

5.2.2 P41

Measurement point P41 is placed on the pipe indicated in figure 5.3. As displayed in the figure, the outlet boundary from the CFD is based on three locations in the real structure. The geometry is symmetric upstream these boundaries, but downstream there are three pipes of different lengths that is collected in a manifold. After the manifold the pipe diameter is increased from 80 mm to 200 mm. The measurement point is placed 5.7 m downstream the manifold in the 200 mm pipe. Measurements from P41 is assumed to be more accurate than the ones in P38 due to a more ideal placement.

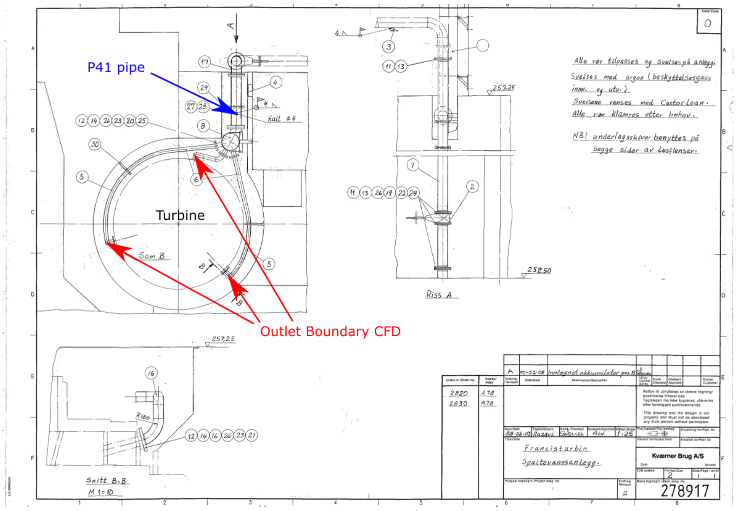

Figure 5.3: Location of measurement point P41 in the fluid, marked on mechanical drawing B.4. The figure only indicates the pipe which is measured and not the exact location of the point. The distance from the manifold to the measurement point has been confirmed as 5.7 m by Eidsiva.

However these measurements are more problematic to use in the CFD study due to the asymmetry of the pipes, and hydraulic elements in the pipes. The BOM which is displayed in figures B.5, B.6 and B.7 show that there is an accumulator placed on the manifold of the pipes. Date stamps on the BOM shows that it was also the case in 2014 when measurements were made. This will reflect some of the pressure, depending on the volume in the accumulator. which means that the amplitude is reduced in the pipes downstream. Unfortunately the BOMs was not available until a late in the study so this could not be accounted for when establishing the boundary conditions for the CFD. Effects, from this misunderstanding, on the results will be discussed in chapter 6.

5.3 Frequency Analysis

Most of the FFT plots from measurement points P38 and P41 show a dominating amplitude at a frequency of $36,5$ Hz. The plots from P41 also show a smaller peak at 73 Hz which seems like it is the second harmonic of the 36.5 Hz frequencies because it has double the frequency. No other significant peaks are shown on any of the measurements at P41. The amplitude peaks at 73 Hz are also present in most of the measurements at P38 both with and without air intake. These peaks seem to disappear on runs at 56 MW and full load while they are small at around 47 MW. However these peaks do appear downstream so there could be some unwanted filtering of the values at this frequency.

There are also some large amplitudes present on higher frequencies at measurement point P38. The most significant amplitude is present on the runs on 47 MW and higher outputs for the runs without air intake. A large peak is present at 186 Hz, but is not visible for the runs below 37 MW. The runs on high outputs was done earlier in the day according to the time schedule so this could be a case where accumulation of bubbles on the pipe is filtering out this frequency from the measurements for the last runs. However there are no peaks at this frequency at any of the measurements at P41. This could be because of dampening across the accumulator. There could also be resonance at this frequency in the volume where P38 is placed causing the peak to appear only at specific runs.

5.4 Resonance

Resonance could be a source for the high amplitudes that are present in the measurements. As previously discussed in section 2.2.1 resonance occur when a standing wave form is present which only appear at specific wave lengths. These wave lengths are only dependent of the pipe length and wave speed. Relevant pipe lengths has to be checked against standing wave conditions. This is done in order to determine if resonance is present, or can occur from small changes, in any of the pipe sections. Four pipe lengths will be checked in this section including the three asymmetrical pipe sections upstream the accumulator and the larger diameter pipe between the accumulator and the outlet. The pipes are marked Pipe A-D in this section and figure 5.4 displays which marking is related to which pipe.

There are no detailed mechanical drawings of the slit water pipe system. Because of this the lengths of pipe A-C are measured roughly with a ruler and protractor based on the knowledge that radius from the center of the turbine to the pipes are 1.5 m. They consist of a symmetrical section of 780 mm and asymmetrical section of different lengths. By considering the pipe as a combination of straight and curved sections, these length can be found when the curvature radius is known.

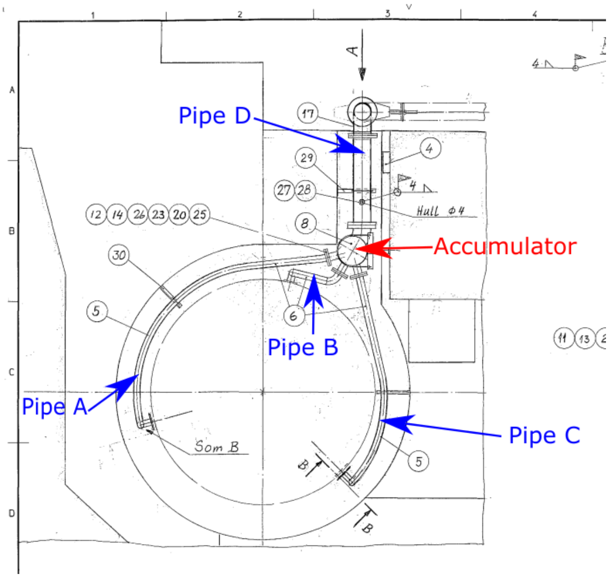

Figure 5.4: Location of pipes named A-D in the fluid, marked on the mechanical drawing from figure B.4.

The pipe lengths are listed in table 5.1 along with other relevant parameters for all four pipe sections. There might be some minor measurement errors to the estimated lengths of pipes A-C. For Pipe D the length from the accumulator to the outlet to the cooling water basin is 107.5 m. This information has been provided by Eidsiva who owns the power plant. There are also other elements that could lead to partial reflections of the waves like sharp bends, inlets, outlets and branches in the pipe system. Because there are no detailed mechanical drawings from the pipe system it is hard to account for all of these minor effects. As such it is assumed that the only significant partial reflection in the pipe system occurs at the accumulator and all others are neglected.

Parameters	**Pipe A**	**Pipe B**	**Pipe C**	**Pipe D**
Length [m]	4.5	1.5	3.6	107.5
Inner Diameter [mm]	80	80	80	200
Wall thickness [mm]	3	3	3	3
Youngs modulus [GPa]	193	193	193	193

Table 5.1: Relevant parameters for the pipe sections used in resonance study.

According to the BOM in figure B.5 the material used in all pipes are SIS2333, which is a stainless steel alloy more commonly known as AISI 304L. Material data are found from looking at the datasheet for this alloy at werkstoff number 1.4307. This is used to find the Young's modulus for the pipes. The data in table 5.1 can be used to calculate the wave propagation speed using (2.3). As previously discussed in section 2.2.2 this equation calculates the wave speed assuming no air content in the water. Figure 2.2 shows the variation in wave speed with air content in the pipe. It shows that the variation in wave speed is small after the pressure passes a certain threshold for a specific air content value. This threshold is equal to the wave speed without any air.

The bulk modulus for water at atmospheric pressure and $20°C$ is 2.19 GPa [2]. This value is used in the calculations because it is listed in the source and the temperature and background pressure is unknown in this case. (K/E)(D/e) values for the pipes are 0.303 and 0.756 for pipes A-C and D respectively. This gives wave speeds of 1298 m/s and 1118 m/s for the two different diameters assuming no air content in the water. The plot in figure 2.2 has a (K/E)(D/e) value of 0.263 which is comparable to the 80 mm diameter pipes for this case. This could have been used to approximate the effect of the air content, but the air content is unknown in this case. It is reasonable to assume that there are some air bubbles in the water naturally even when the air intake is not used. For low pressures the wave speeds are highly sensitive to the air content even when the air content is lower than 0.001%. As such no air content in the water is not necessarily a good assumption, but better assumptions cannot be made unless the wave speeds are measured experimentally at Torpa in the relevant pipes.

Minimum resonance frequencies assuming the calculated wave speed of 1298 m/s in pipe A-C and 1118 m/s in pipe D are listed in table 5.2. Because pipe sections A-C are short, all possible resonance frequencies at this velocity are higher than all the significant frequency peaks from the measurements at P38 and P41. Pipe D however is longer and have a wide range of frequencies that cause resonance at a wave speed of 1118 m/s. Some of these frequencies are listed in table 5.3. There are resonance frequencies at a difference of 2.5 Hz from both the 36.5 Hz peak and 73 Hz peak. No other significant peaks were measured at measurement point P41 so it is assumed that there are no resonance in this pipe at other frequencies. Since the measured peaks are placed approximately in the middle of the closest resonance frequencies it does not seem to be resonance on any of these peaks with the assumption of no air in the pipe. However a better estimate of the wave speed is needed to confirm this.

	Pipe A	**Pipe B**	**Pipe C**	**Pipe D**
Minimum Resonance Frequency [Hz]	216	649	270	7.8

Table 5.2: Minimum Resonance Frequencies for the pipe sections assuming a wave speed of 1298 m/s for Pipe A-C and 1118 m/s for Pipe D.

Resonance Wave Length	$4L/13$	$4L/15$	$4L/27$	$4L/29$
Resonance Frequency [Hz]	$33,8$	39	70.2	75.4

Table 5.3: Closest resonance frequencies to the peaks at 36.5 Hz and 73 Hz in Pipe D. Assuming wave speed of 1118 m/s.

Another way to look at the problem is to define which wave speeds cause resonance at a specific frequency. Table 5.4 shows the maximum wave speeds that can cause resonance at a frequency of $36,5Hz$. The wave speeds are low for pipes A-C because they are short. That means resonance can only occur at this frequency with a combination of low pressure and high air content. There is also a wide range of wave speeds below the maximum of 1118 m/s in pipe D that cause resonance in this pipe section. Some relevant wave speeds are presented in table 5.5. If the wave speed is measured experimentally at Torpa in pipe D it can be confirmed that there might be resonance when the wave speed is close to any of those values. A lower wave speed than 628 m/s means that lower resonance speeds needs to be calculated to check with resonance conditions. This can easily be done in an excel spreadsheet for other wave lengths and other frequencies using equations (2.1) and (2.2).

	Pipe A	**Pipe B**	**Pipe C**	**Pipe D**
Maximum Resonance Wave Speed [m/s]	219	73	175	5232

Table 5.4: Maximum wave speeds that can cause resonance at 36.5 Hz in pipe sections A-D.

Resonance Wave Length	$4L/15$	$4L/17$	$4L/19$	$4L/21$	$4L/23$	$4L/25$
Resonance Wave Speed [m/s]	1046	923	826	747	682	628

Table 5.5: Some wave speeds that cause resonance at 36.5 Hz lower than the maximum wave speed 1118 m/s.

There might also be resonance in the volume above the head cover where measurement point P38 is located, but this is harder to determine than in the pipes. This is because there are a lot of circulation in this volume and it is hard to determine how long the path of a pressure wave is in this area. As such it has not been considered in this section. There might also be resonance from the length of a combination pipe sections A-C and D. Since pipes A-C are short in comparison to pipe B it is likely to also be resonance in the combination of the pipes if there is resonance in pipe D isolated. However since the accumulator is placed between the pipe sections, only a part of the pressure amplitude gets through causing resonance effects to be lower in pipe A-C if pipe D is the source.

Chapter VI

Results and further work

■ This is the final chapter in the report. It starts by presenting the results from the CFD, comparing it with the measurement values. Several possible sources of errors exist and the effect of these factors are discussed. FFT plots were made for the CFD simulations, but suffer from poor frequency resolutions. Some misunderstandings during the course of this study has also lead to significant errors in the assumptions made for the boundary conditions. The conclusion section summarises the results in both chapter 5 and 6, and provides some recommendations for the case. The CFD results do not indicate that vortex shedding in the slits are the source for the dominating 36.5 Hz peaks from the measurements. Further improvements need to be made to the CFD before this can be confirmed. Accumulators can be installed at some locations in the pipe system to increase its lifetime of the pipes without any additional danger for resonance. Finally some specifics suggestions are made for the further work. This includes considering what should and should not be prioritised in the future, and some specific advice for how improvements could be made to the CFD.

6.1 CFD Results

Results of the CFD is based on the data presented in appendix C.2. The gauge pressure on the monitor points in the slit is plotted in figures C.6 to C.9. These plots show that there are higher frequencies measured in the slit in addition to the 36.5 Hz on the outlet boundary. In order to interpret the signals FFT plots were made for the pressures at monitor point 1-12 and is displayed in appendix C.2.3. The sampling frequency was $200,000$ samples/s corresponding with a timestep of $5e-6s$ and $20,000$ samples were made for the total simulation time of 0.1 s. This gives a frequency resolution of 10 Hz which is higher than it ideally should be [8]. However they are still assumed to provide better accuracy than what can be achieved by eye with a ruler.

Some problems occur with the FFT plots related to this issue. For the main frequency, which is 36.5 Hz, the energy would be split between the bin at 30 Hz and 40 Hz in the plot. This means that the approximation of the pressure amplitudes in these plots are poor. However it can give a fairly accurate indication of which frequency regions the highest peaks occur. The frequencies of the peak amplitudes are not known accurately either. A peak at 40 Hz in the plot could be based mainly on energy from a peak anywhere between 35 Hz and 45 Hz. The size of the neighbouring peaks will give some indication into where the peak lies in the range, as it will be near 40 Hz if both neighbouring peaks are small, and closer to 30 Hz if that peak is higher than the one at 50 Hz. There could also be issues if there are two frequency peaks close to each other meaning that energy from two peaks are collected in the same frequency bin. Looking at the FFT plots from the vibrational measurements it does not look like any of the measurements made at P38 or P41 have peaks closer than $25 - 30$ Hz from each other. Based on these arguments it can be assumed that the frequency of the peaks can be trusted with an accuracy of ± 5 Hz, but the individual pressure amplitude values are too inaccurate to trust.

Most of the monitor points have the highest peak amplitude near 40 Hz which is assumed to correspond with the 36.5 Hz amplitude implemented on the outlet. These amplitudes change slightly between 16 kPa and 20 kPa. Unfortunately due to the previously discussed issues with the FFT it is hard to determine if this is caused by slight amplitude increases or frequency shifts. The amplitude on the outlet is 23.5 kPa at 36.5 Hz, and it does not seem to be any significant increase in this amplitude at any of the monitor points in the slit.

Many of the monitor points has a second peak at 90 Hz. Interestingly this frequency equals the frequency of von Karman vortex shedding by using the slit height as a characteristic length which was calculated in section 2.1.2. The free stream velocity and characteristic length used in that calculation correspond very well with the conditions from the simplified domain used in the simulation specified in section 4.3. It does not fit as well for the real geometry presented in section 4.1, where the slit height varies between 65 mm and 93 mm. A decrease in characteristic length cause an increase in frequency for a given Strouhal number. The free stream velocity will also be smaller due to the effects displayed in figure 4.19 when it is driven by a moving wall. A decrease in free stream velocity gives a decrease in frequency for a given Strouhal number. It is not known if the Strouhal number is constant for the vortex shedding frequencies in this case, but it was constant for both cavity tone and von karman vortex streets which are comparable phenomenons.

Some of the monitor points had peaks at 140 Hz as well. No significant peaks was seen near 90 Hz or 140 Hz in the FFT plots from the measurements at Torpa.

Monitor point 12 has a lot of high peaks that is not seen on the other monitor points. This might be a case of CFD instabilities in the point dominating the frequencies that were measured at the other points. None of the extra frequency peaks propagate downstream to the monitor points at the location of measurement P38 displayed in figure C.11, or the monitor points in the pipe in figure C.10. All these monitor points measures an even sine wave corresponding with the outlet boundary condition plotted in figure C.14. FFT plots has not been made for these monitor points because the amplitude and frequency can be seen clearly from the pressure plots. The average inlet pressure, displayed in figure C.27, did have some small peaks at 90 Hz and 140 Hz in addition to the 36.5 Hz peak.

Monitor points 19-23 are located in the same region as measurement point P38. These are used as validation and there are large differences between the measurements and the CFD results. There are some frequency peaks in the measurements that is not seen in the same region for the CFD, and the amplitude is lower at 36.5 Hz for the CFD. Some of the peaks in the measurements can come from mechanical vibrations that the CFD simulations cannot account for. Other discrepancies between the CFD simulations and measurements can be caused by errors in the definition of the boundary conditions.

The assumptions made on the outlet boundary was that the pressure amplitude was equal to the amplitude measured at measurement point P41. However that assumption was made before the parts list for the slit water system was acquired. An important discovery from the parts list is that there is an accumulator between the outlet boundary and measurement point P41, which was used in the discussion in chapter 5. This means that there is a significant amplitude drop downstream the accumulator, meaning that the pressure on the outlet boundary should be higher than the pressure at measurement point P41. It would be closer to the amplitude at P38, but that would mean that this is used both as a validation and to determine the boundary condition. This would mean that the validation point is forced towards the real value by the boundary condition. Ideally these should be based on different measurements. The frequency peaks at both P38 and P41 are at approximately 36.5 Hz so it is reasonable to assume that it is close to the real frequency in the CFD outlet pipe. A better boundary condition could be defined by including the second harmony at 73 Hz, but it is also difficult to establish the exact amplitude of this frequency peak at the outlet boundary without performing more experimental measurements.

There was also a misunderstanding related to the volumetric flow rate. The $0,3\%$

leak from the best water flow, discussed in section 4.1, relates to the entire slit water system meaning that the flow through one of the three slits is $\frac{48L/s}{3} = 16L/s$. This will reduce some of the velocities in the flow, and it is unsure how much that influences the solution. The free stream velocities that was considered in the vortex shedding frequency calculations will remain unchanged because the rotation from the turbine is still 600 rpm. The volumetric flow rate through the slit is not constant like it was assumed in the simulations. This is because the pressure above the slits vary with the different turbine efficiency outputs. This effect might be the reason that the measured amplitudes vary a lot with the output as seen in figure 5.1.

6.2 Conclusions

Because of the mistakes that has been made in the boundary condition assumptions it is hard to conclude with anything from the CFD simulation at this stage in the study. The results points towards vortex shedding in the slit not being the source of the high amplitude peaks at 36.5 Hz at Torpa. There are several reasons why. One is that the pressure fluctuation in the slit did not propagate downstream to the monitor points above the head cover and to the outlet pipe. There is also no amplification of the 36.5 Hz peak compared to the outlet condition through any of the monitor points in the slit, which indicates that these frequencies are not produced there. However it needs to be kept in mind that the FFT plots from the CFD did not indicate the exact amplitudes of the peaks well. Since the boundary conditions are different from the real condition on both the inlet and the outlet it is hard to get a good validation against the measurements at P38. Because of this it is hard to establish the accuracy of these CFD simulations. The simplification done on the inlet might also influence the solution, because the free stream velocity will decrease when the inlet is defined through the labyrinth seal and rotation is driven by the rotating wall. This can lead to a decrease in vortex shedding frequency and might mean that it is closer to 36.5 Hz in reality.

For the case at Torpa accumulators can be used to reduce pressure amplitudes in the pipes. The measurement results from P41 show a significant drop in pressure amplitudes compared to the measurements at P38. This effect could be amplified by increasing the volume of air or gas in the accumulator that is already present at the power plant. However this leaves the three pipes upstream the accumulator, named pipe A-C in chapter 5, vulnerable to the high pressures in the volume above the head cover. A possibility, which will also increase the lifetime of these pipes, is to fit one accumulator on each of these three pipe inlets. This will isolate the high pressure amplitudes in the volume above the head cover. The old accumulator could also be kept as is for this solution for additional dampening. It is very unlikely that any resonance will occur at the measured frequencies for pipe A-C because they are short as discussed in chapter 5. As such resonance should not be an issue if accumulators are installed on both ends of these pipe sections.

6.3 Further Work

The main priority in the further work should be related to validating the hypothesis established by Rainpower before trying to optimise the design in any way. Improvements can be made for the CFD by changing the boundary conditions to more realistic options. There are still uncertainties related to these conditions however. It would be very beneficial for the CFD if new measurements can be made of the pressures and volumetric flow rates on the three pipes where the outlet boundary of the CFD is defined. Measurements of the wave propagation speed at both diameter pipes would also be very beneficial for resonance calculations. If there are no openings to insert sensors into these pipes one possibility is to try non-intrusive measurement methods.

The setup with geometry and mesh in CFX seems to work well, but some improvements could be made regarding mesh dependency by increasing the mesh size further. After it was clarified that the volumetric flow rate is in the region of 16 L/s it might not be necessary to keep the simplification on the inlet anymore. The axial velocity on the inlet is reduced from 43 m/s to $14,3$ m/s. This is still quite high across a cell in the region of $0,75$ mm in regards to stability, but it is better than it was with the previous assumption. If the inlet is defined as a body as displayed in figure 4.4 that body becomes sweepable and it is easy for the user to define the lengths of these cells in all directions. A good strategy here is to accept higher aspect ratios and stretch the cells in the tangential direction where the maximum velocity is in the range of $44,5$ m/s such that the Courant condition is satisfactory in the area without having to reduce the timestep substantially. The inlet could also be defined on just the surface of the volume, but then the cell shapes and sizes are harder for the user to control. As such it is recommended to have a one cell deep inlet body with free slip walls.

Simulating with a compressible fluid model should not be prioritised in the continuation of this work. This is because the computational cost is too high based on the available time and resources in a master thesis study. It is also not known what the speed of sound is at the plant. However since there is no frequency shift between measurement points P38 and P41, it seems like the wave speed is fairly constant at the plant even though the calculations from chapter 5 indicated otherwise. One possible explanation could be that the air content is slightly higher in pipes A-C. This means that the compressibility model from equation (2.5) might be valid if compressible solutions are desired in the future. It should also not be prioritised to simulate for a longer time in order to increase the FFT frequency resolution. A better strategy would be to investigate interpolation techniques that can be used to increase the resolution from [8].

When it comes to optimising the slit design, which Rainpower wanted to investigate, that should be not be prioritised until the hypothesis is properly validated and a satisfactory numerical and physical model is established. It might not be the best idea to use CFD to optimise the design either. The computational cost is already quite high with a simulation time of 13 days and 11 hours using a 12 core processor. After continued development of the CFD model, this cost will most likely increase even further. If every simulation takes around a month it is going to be hard to simulate enough different parameters to get a good optimisation and it will be up to the user to make good guesses on which changes that will influence the design positively. This seems to be way outside what can be expected from the time and resources available in a master thesis study.

References

[1] Kaneko, S., Nakamura, T., Inada, F., Kato, M., Ishihara, K., and Ishihara, T., 2013, *Flow Induced Vibrations: Classifications and lessons from practical experiences*, Elsevier Science Technology.

[2] White, F., 1998, *Fluid Mechanics, Fourth Edition*, McGraw Hill.

[3] Marjavaara, D., 2006, “CFD driven optimization of hydraulic turbine draft tubes using surrogate models,” .

[4] Zikanov, O., 2010, *Essential Computational Fluid Dynamics 1st edition*, John Wiley Sons, Incorporated.

[5] Wyley, E. B. and Streeter, V. L., 1978, *Fluid Transients*, McGraw Hill.

[6] Yin, J. L., Wang, D. Z., Q., W. L., L., W. Y., and Wei, X. Z., 2012, “Effects of water compressibility on the pressure fluctuation prediction in pump turbine,” *IOP Conference Series: Earth and Environmental Science*.

[7] Trivedi, C., 2018, “Investigations of compressible turbulent flow in a high-head francis turbine,” Journal of Fluids Engineering, **140**(1).

[8] Gasior, M. and Gonzalez, J., 2004, “Improving FFT frequency measurement resolution by parabolic and Gaussian spectrum interpolation,” *AIP Conference Proceedings* (Vol. 732), American Institute of Physics, pp. 276–285.

[9] ANSYS, 2019, *CFX-Pre User’s Guide*.

[10] Ferziger, J. and Péric, M., 2002, *Computational Methods for Fluid Dynamics 3rd edition*, Springer.

[11] Strikwerda, J. C., 2004, *Finite difference schemes and partial differential equations*, Vol. 88, Siam.

[12] Versteeg, H. and Malalasekera, W., 2007, *An Introduction to Computational Fluid Dynamics, 2nd edition*, Pearson education.

[13] Menter, F. R., Kuntz, M., and Langtry, R., 2003, “Ten years of industrial experience with the SST turbulence model,” Turbulence, heat and mass transfer, **4**(1), pp. 625–632.

[14] Çengel, Y. and Cimbala, J., 2006, *Fluid Mechanics: Fundamentals and Applications 1st edition*, McGraw Hill Education.

[15] Balchen, J. G., Andresen, T., and Foss, B. A., 2004, *Reguleringsteknikk*, NTNU, Institutt for teknisk kybernetikk.

Appendix - A

Theory supplement

■ This section provides a supplement to the theory and literature study chapters. It includes figures and theory descriptions that are not necessary for the work in the report, but provides additional context that might interest the reader.

A.1 Cavity Tone

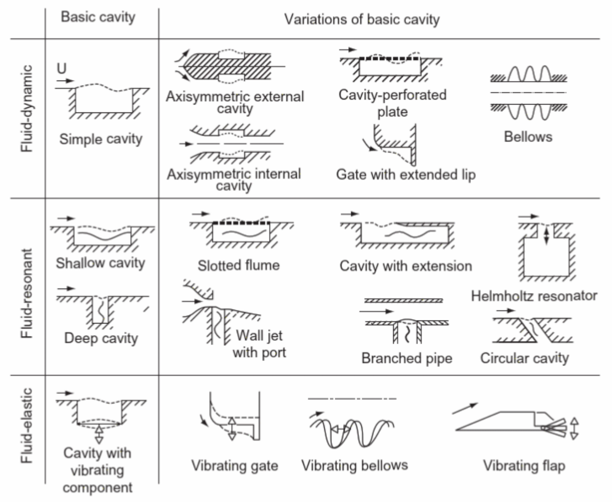

Figure A.1: Collection of basic cavity variations. [1] figure 5.50 p.263

A.2 Mesh Quality

A.2.1 Skewness

Skewness measures the misalignment between angles in a cell. Hexahedral cells perform best with all angles equal at 90 degrees at all faces of the cell, while tetrahedral cells performs best with all angles at 60 degrees. This corresponds to a skewness value of 0. For most geometries however the cells needs to be shaped differently in order to capture details of the geometry. The skewness value goes towards 1 as the maximum angle, θ_{max}, goes toward 180, or minimum angle, θ_{min}, goes toward 0 [9].

$$Skewness = max(\frac{\theta_{max} - 90}{90}, \frac{90 - \theta_{min}}{90}) \tag{A.1}$$

$$Skewness = max(\frac{\theta_{max} - 60}{120}, \frac{60 - \theta_{min}}{60}) \tag{A.2}$$

A.2.2 Orthogonality

Orthogonality is a mesh quality parameter which relates to reconstruction of fluxes in the discretisation. Fluxes are defined to the middle point of a cell boundary as $\vec{S}$ in figure A.2. However they are calculated through an interpolation through the cell centers as $\vec{d}$. If the cells are not parallel a distance, $\vec{m}$, between the point where the flux is defined and where the flux is actually calculated. Naturally the error increase with the distance between these points. The value for orthogonality is calculated as (A.3) which corresponds with cosine of the angle between the interpolated flux and the real flux. That means 1 is the desired value and the performance get worse as the orthogonality goes toward 0 [9].

$$Orthogonality = \frac{\vec{S} \cdot \vec{d}}{|\vec{S}||\vec{d}|} \tag{A.3}$$

A.2.3 Aspect Ratio

Aspect Ratio is a mesh quality parameter which measures the ratio between the side lengths of a cell face. The best performance is achieved with an aspect ratio of 1 which is achieved if the sides of a cell face, or the face areas of a 3D cell is equal. Errors increase with higher aspect ratios [9].

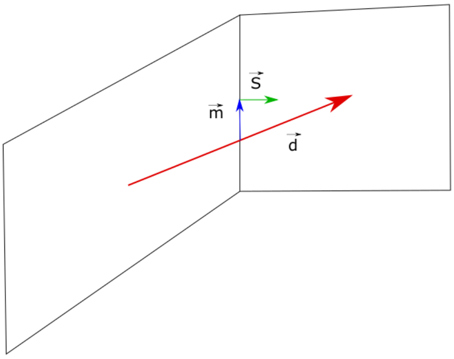

Figure A.2: Vectors from orthogonality calculations

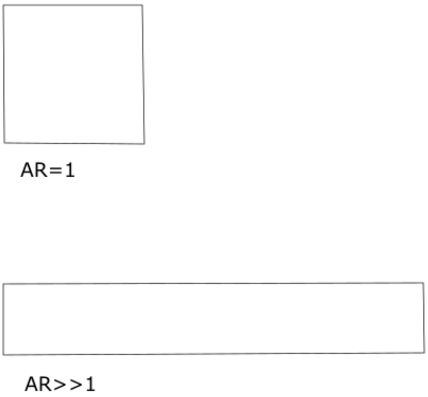

Figure A.3: Comparison between desirable and less desirable aspect ratio

A.2.4 Smoothness

Smoothness is a mesh quality parameter related to the difference between cell lengths of bordering cells. Errors occur if there is a large jump between bordering cell sizes. The best performance is achieved when the lengths are equal which corresponds with a smoothness value of 1, but values between 0.8 and 1.2 are acceptable [9].

Not Ok!

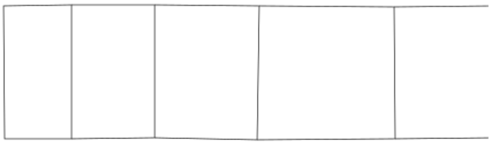

Ok!

Figure A.4: Comparison of desirable and undesirable smoothness in a mesh.

Appendix - B

Data from Torpa Power Plant

B.1 Mechanical Drawings

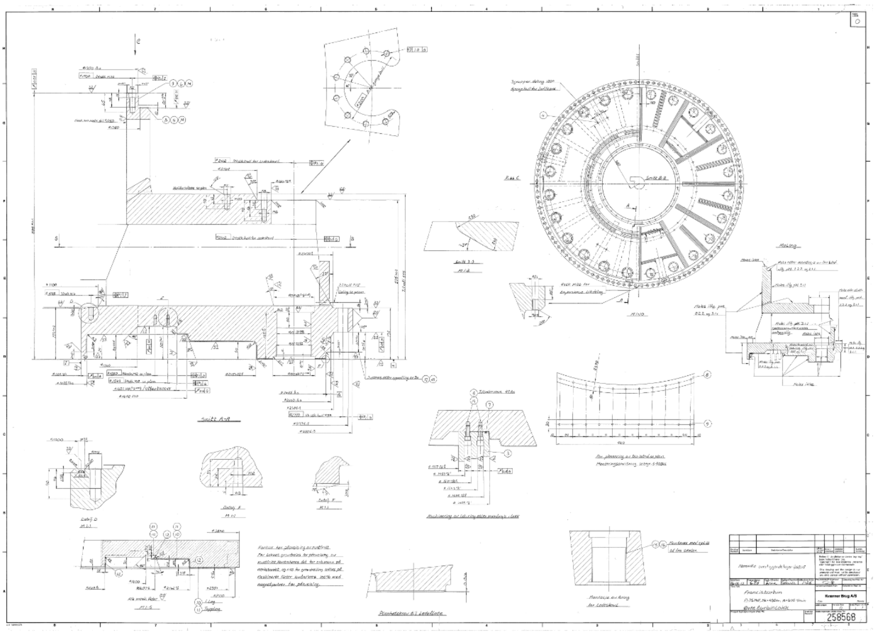

Figure B.1: Mechanical drawing of the head cover at Torpa. Shared with permission from Eidsiva.

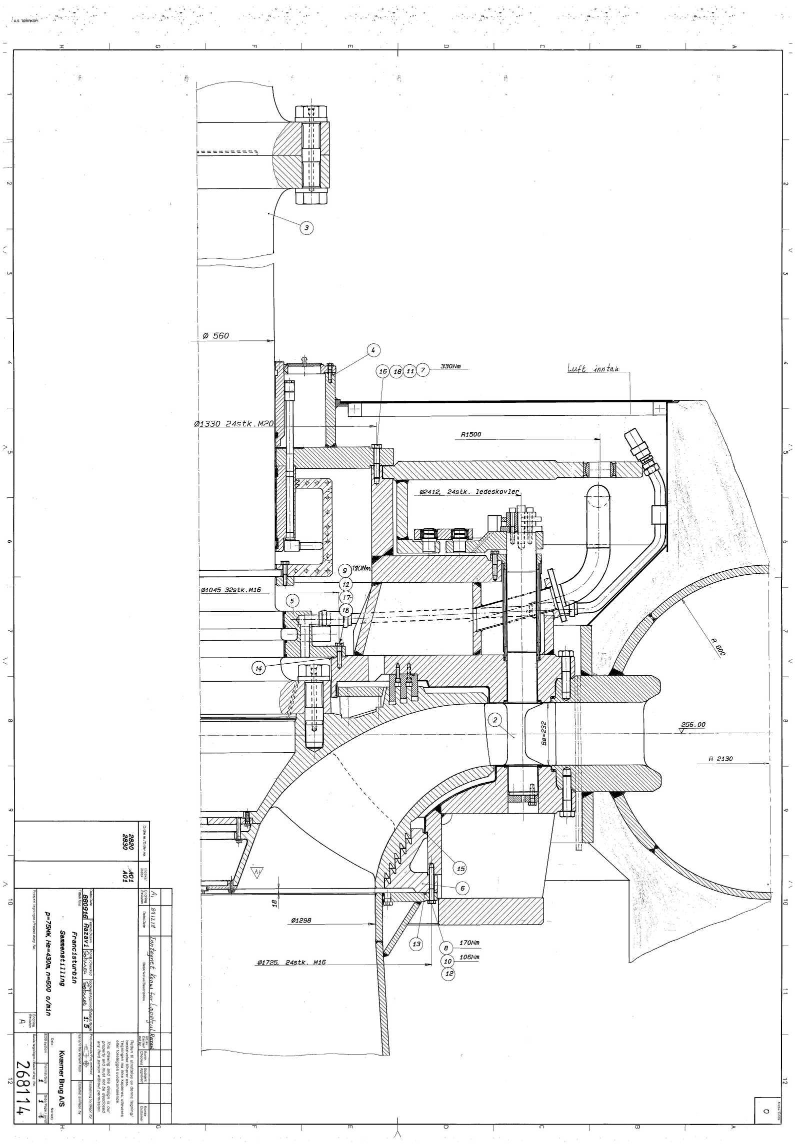

Figure B.2: Cross section drawing of the turbine at Torpa Power Plant. Shared with permission from Eidsiva.

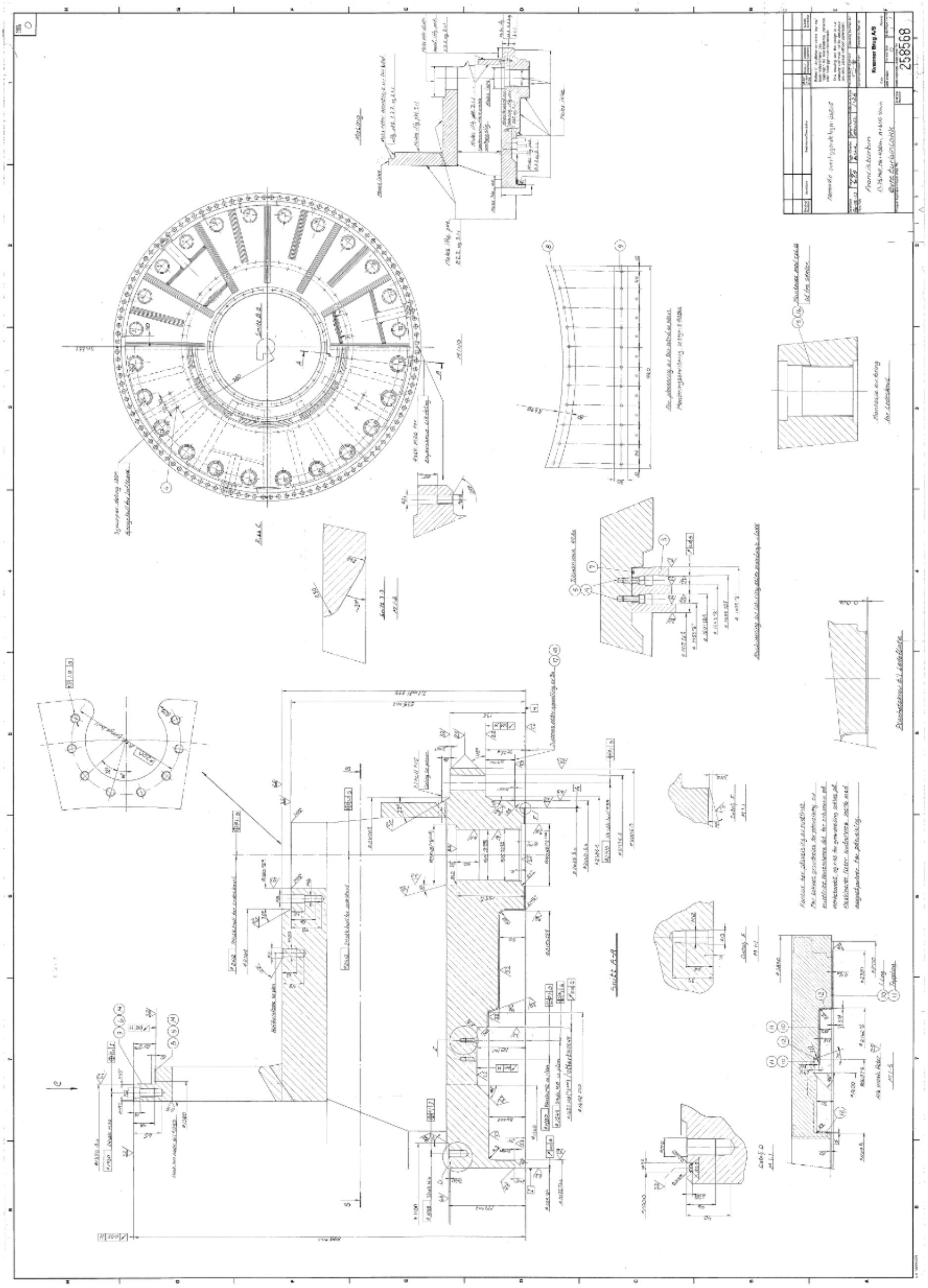

Figure B.3: Mechanical drawing of the head cover at Torpa with soldering instructions. Shared with permission from Eidsiva.

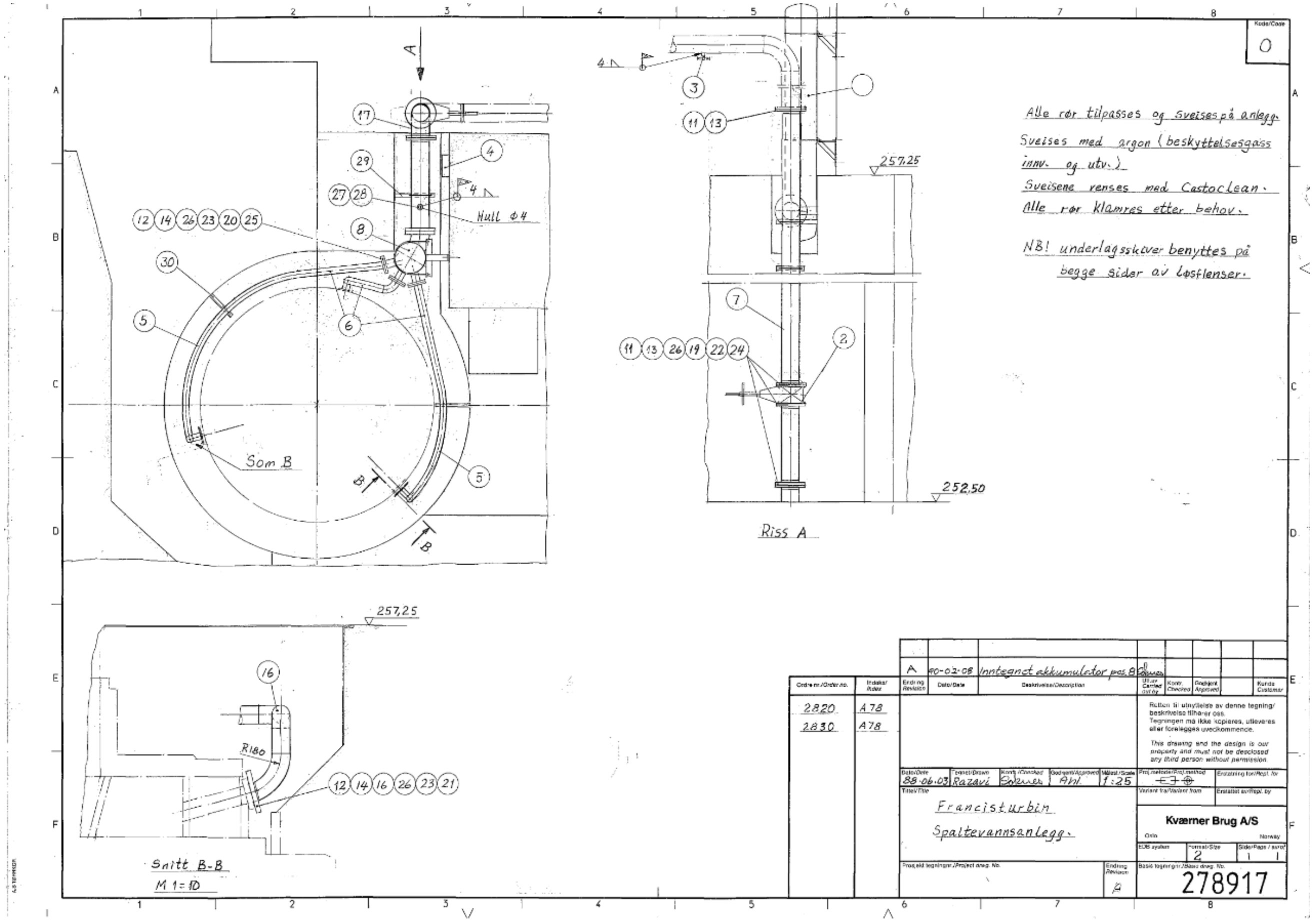

Figure B.4: Mechanical drawing of the slit water system at Torpa. Shared with permission from Eidsiva.

B.2 BOM

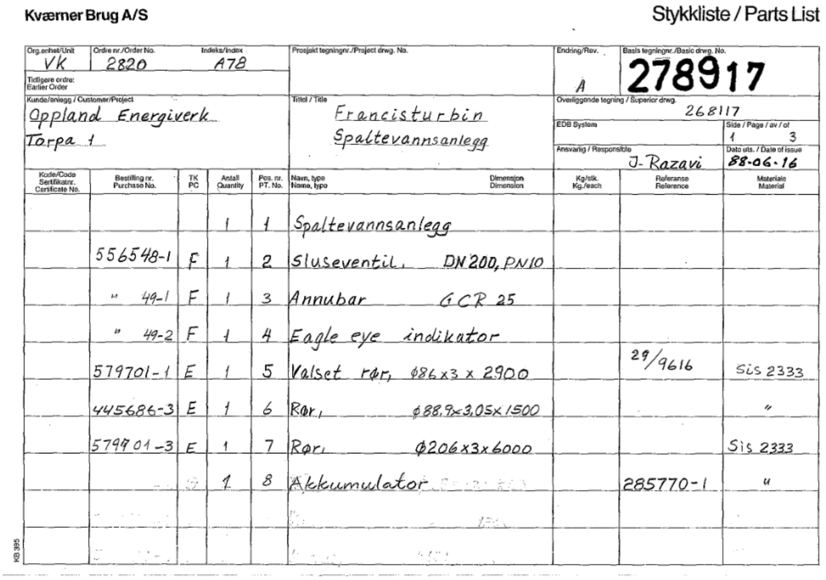

Kværner Brug A/S

Stykkliste / Parts List

Org.enhet/Unit: VK
Ordre nr./Order No.: 2820
Indeks/Index: A78
Tidligere ordre: Earlier Order:
Prosjekt tegningnr./Project drwg. No.:
Endring/Rev.: A
Basis tegningnr./Basic drwg. No.: 278917
Kunde/anlegg / Customer/Project: Oppland Energiverk Torpa 1
Tittel / Title: Francisturbin Spaltevannsanlegg
Overliggende tegning / Superior drwg.: 268117
EDB System:
Side / Page / av / of: 1 3
Ansvarlig / Responsible: J-Razavi
Dato uts. / Date of issue: 88-06-16

Kode/Code Sertifikatnr. Certificate No.	Bestilling nr. Purchase No.	TK PC	Antall Quantity	Pos. nr. PT. No.	Navn, type Name, type	Dimensjon Dimension	Kg/stk. Kg./each	Referanse Reference	Materiale Material
			1	1	Spaltevannsanlegg				
	556548-1	F	1	2	Sluseventil,	DN 200, PN10			
	" 49-1	F	1	3	Annubar	GCR 25			
	" 49-2	F	1	4	Eagle eye indikator				
	579701-1	E	1	5	Valset rør,	ø86 x3 x 2900		29/9616	Sis 2333
	445686-3	E	1	6	Rør,	ø88,9x3,05x1500			"
	579701-3	E	1	7	Rør,	Ø206x3x6000			Sis 2333
			1	8	Akkumulator			285770-1	"

KB 395

Figure B.5: BOM/part list page one in Norwegian from the slit water system at Torpa. Numbers correspond with mechanical drawings in the previous section.

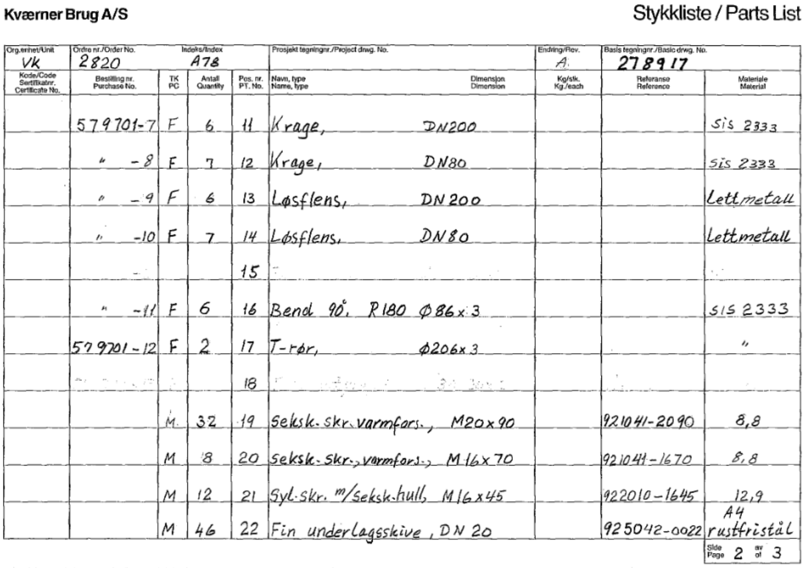

Kværner Brug A/S Stykkliste / Parts List

Org.enhet/Unit: VK
Ordre nr./Order No.: 2820
Indeks/Index: A78
Prosjekt tegningnr./Project drwg. No.:
Endring/Rev.: A
Basis tegningnr./Basic drwg. No.: 278917

Kode/Code Sertifikatnr. Certificate No.	Bestilling nr. Purchase No.	TK PC	Antall Quantity	Pos. nr. PT. No.	Navn, type Name, type	Dimensjon Dimension	Kg/stk. Kg./each	Referanse Reference	Materiale Material
	579701-7	F	6	11	Krage,	DN200			SIS 2333
	" -8	F	7	12	Krage,	DN80			SIS 2333
	" -9	F	6	13	Løsflens,	DN 200			Lettmetall
	" -10	F	7	14	Løsflens,	DN80			Lettmetall
				15					
	" -11	F	6	16	Bend 90°, R180	Ø86x3			SIS 2333
	579701-12	F	2	17	T-rør,	Ø206x3			"
				18					
		M	32	19	Seksk. skr. varmfors.,	M20x90		921041-2090	8,8
		M	8	20	Seksk. skr., varmfors.,	M16x70		921041-1670	8,8
		M	12	21	Syl.skr. m/seksk.hull,	M16x45		922010-1645	12,9
		M	46	22	Fin underlagsskive,	DN 20		925042-0022	A4 rustfristål

KB 396

Side Page 2 av of 3

Figure B.6: BOM/part list page two in Norwegian from the slit water system at Torpa. Numbers correspond with mechanical drawings in the previous section.

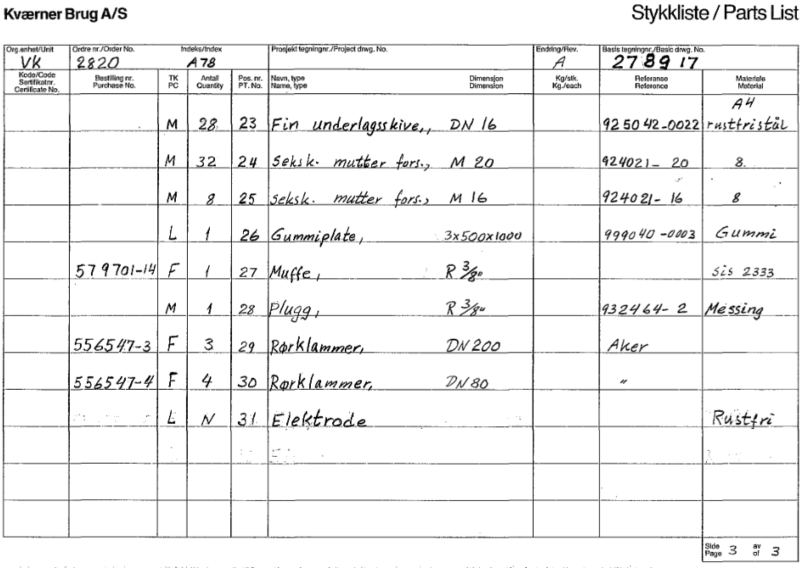

Kværner Brug A/S

Stykkliste / Parts List

Org.enhet/Unit: VK
Ordre nr./Order No.: 2820
Indeks/Index: A78
Prosjekt tegningnr./Project drwg. No.:
Endring/Rev.: A
Basis tegningnr./Basic drwg. No.: 278917

Kode/Code Sertifikatnr. Certificate No.	Bestilling nr. Purchase No.	TK PC	Antall Quantity	Pos. nr. PT. No.	Navn, type Name, type	Dimensjon Dimension	Kg/stk. Kg./each	Referanse Reference	Materiale Material
		M	28	23	Fin underlagsskive,,	DN 16		92 50 42-0022	A4 rustfristål
		M	32	24	Seksk. mutter fors.,	M 20		924021- 20	8.
		M	8	25	Seksk. mutter fors.,	M 16		924021- 16	8
		L	1	26	Gummiplate,	3x500x1000		999040 -0003	Gummi
	579701-14	F	1	27	Muffe,	R 3/8"			SIS 2333
		M	1	28	Plugg,	R 3/8"		932464- 2	Messing
	556547-3	F	3	29	Rørklammer,	DN 200		Aker	
	556547-4	F	4	30	Rørklammer,	DN 80		"	
		L	N	31	Elektrode				Rustfri

KB 396

Side/Page 3 av/of 3

Figure B.7: BOM/part list page three in Norwegian from the slit water system at Torpa. Numbers correspond with mechanical drawings in the previous section.

B.3 SpaceClaim Geometry Dimensions

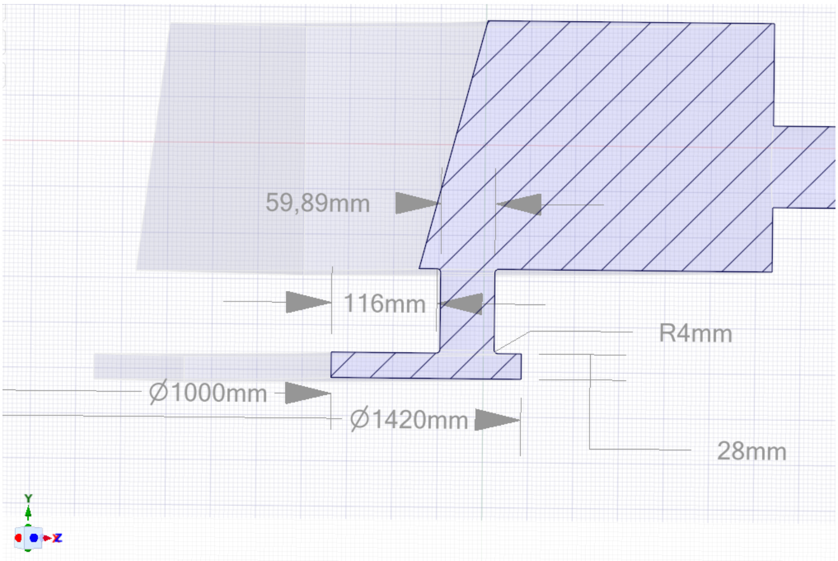

Figure B.8: Dimensions from simplified geometry used in the CFD simulations. Some minor differences may occur between the SpaceClaim model and the mechanical drawings.

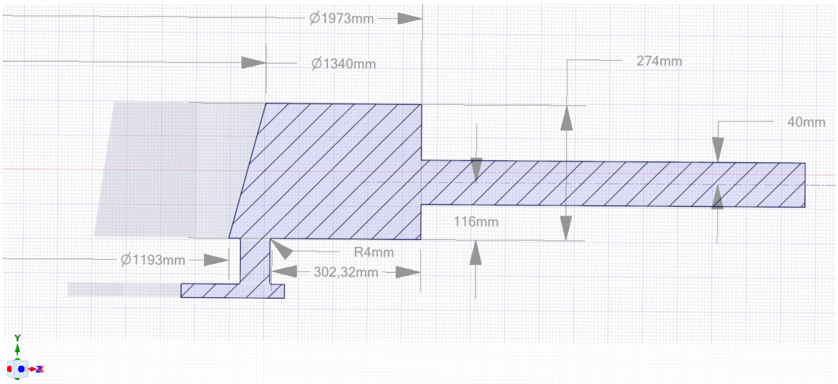

Figure B.9: Remaining dimensions from simplified geometry used in the CFD simulations. Some minor differences may occur between the SpaceClaim model and the mechanical drawings.

Appendix - C

CFD data

C.1 Monitor Points Locations

C.1.1 Slit

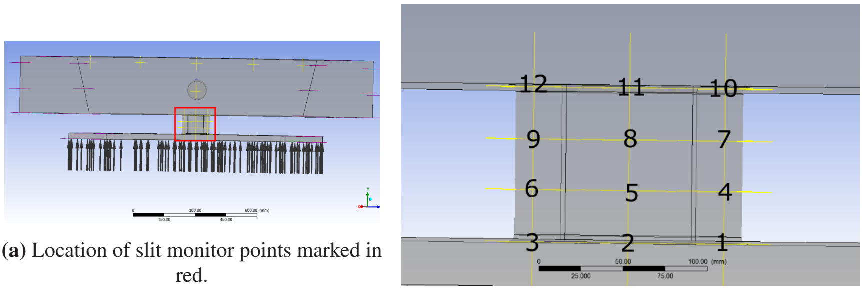

(a) Location of slit monitor points marked in red.

(b) Zoomed in view of monitor points 1-12.

Figure C.1: Location of monitor points 1-12 placed on the slit. The water flows from point 1 to 3 in tangential direction, and 1 to 10 in axial direction.

C.1.2 Outlet Pipe

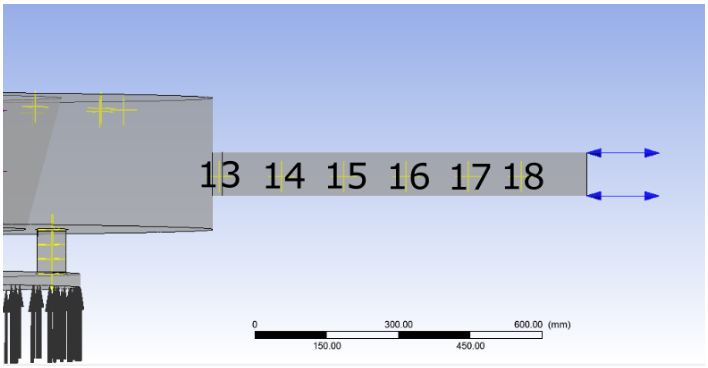

Figure C.2: Monitor point 13-18 locations on outlet pipe.

C.1.3 Above Head Cover

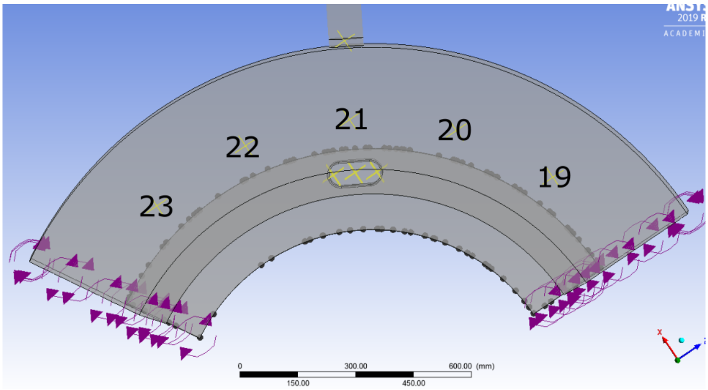

Figure C.3: Monitor point 19-23 locations in volume above the head cover. These points are used as validation against point P38 from the vibrational measurement done by Norconsult.

C.2 CFD transient results

C.2.1 Residuals

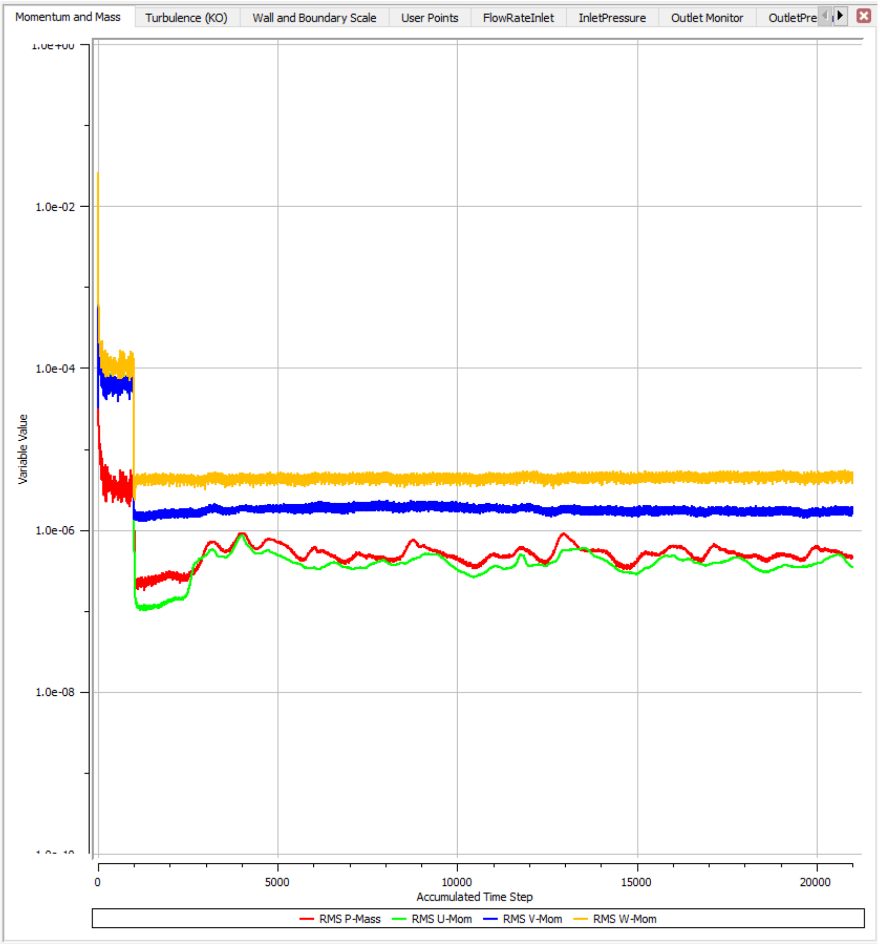

Figure C.4: RMS residuals for transient simulation per timestep. The first 1000 timesteps are the iterations from the steady state initialisation and are included for comparison reason.

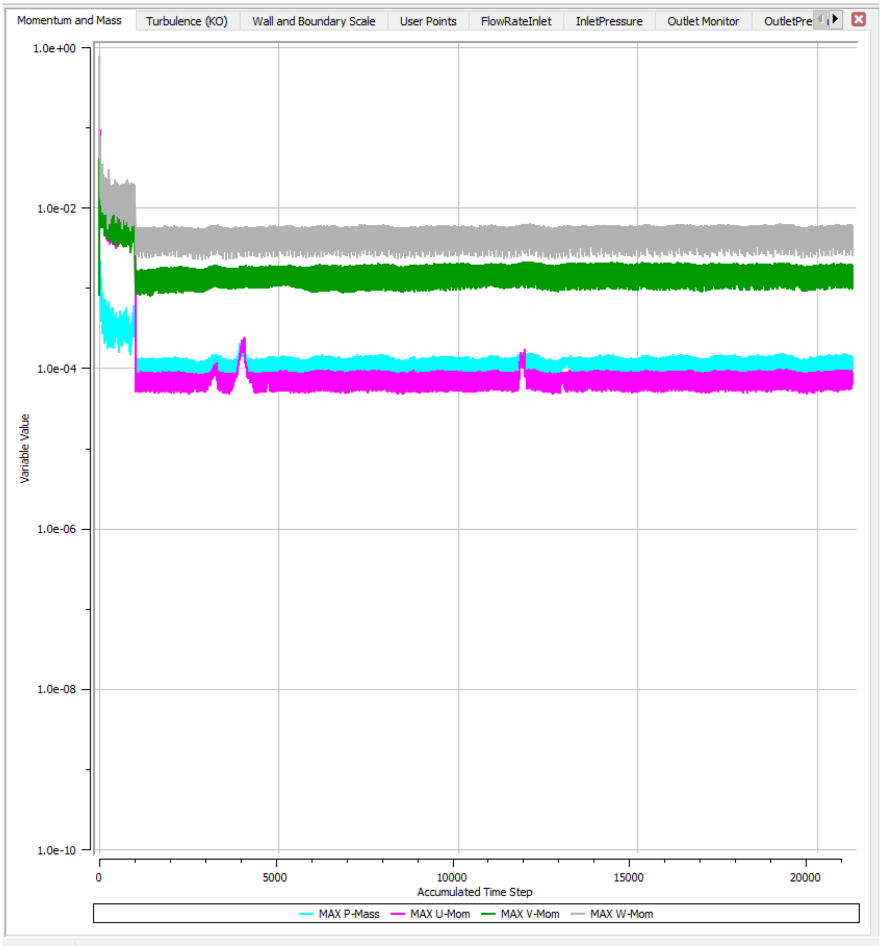

Figure C.5: Max residuals for transient simulation. The first 1000 timesteps are the iterations from the steady state initialisation and is included for comparison reason.

C.2.2 Monitor Points

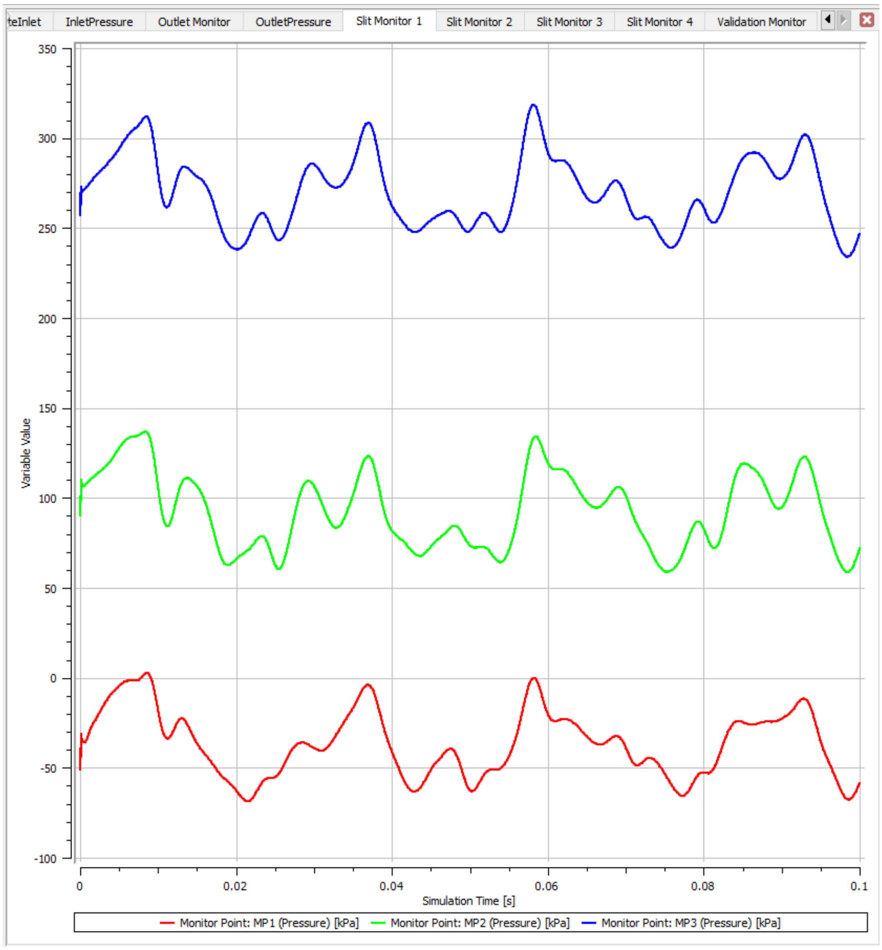

Figure C.6: Pressure values for monitor points 1-3 plotted against simulated time.

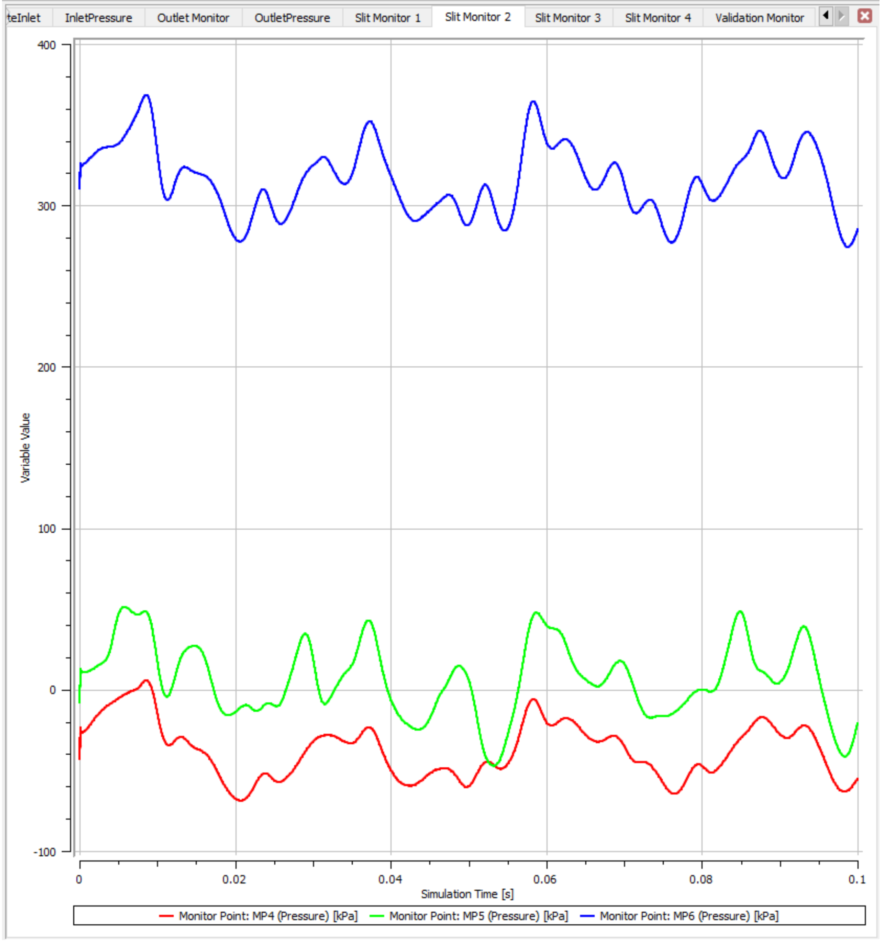

Figure C.7: Pressure values for monitor points 4-6 plotted against simulated time.

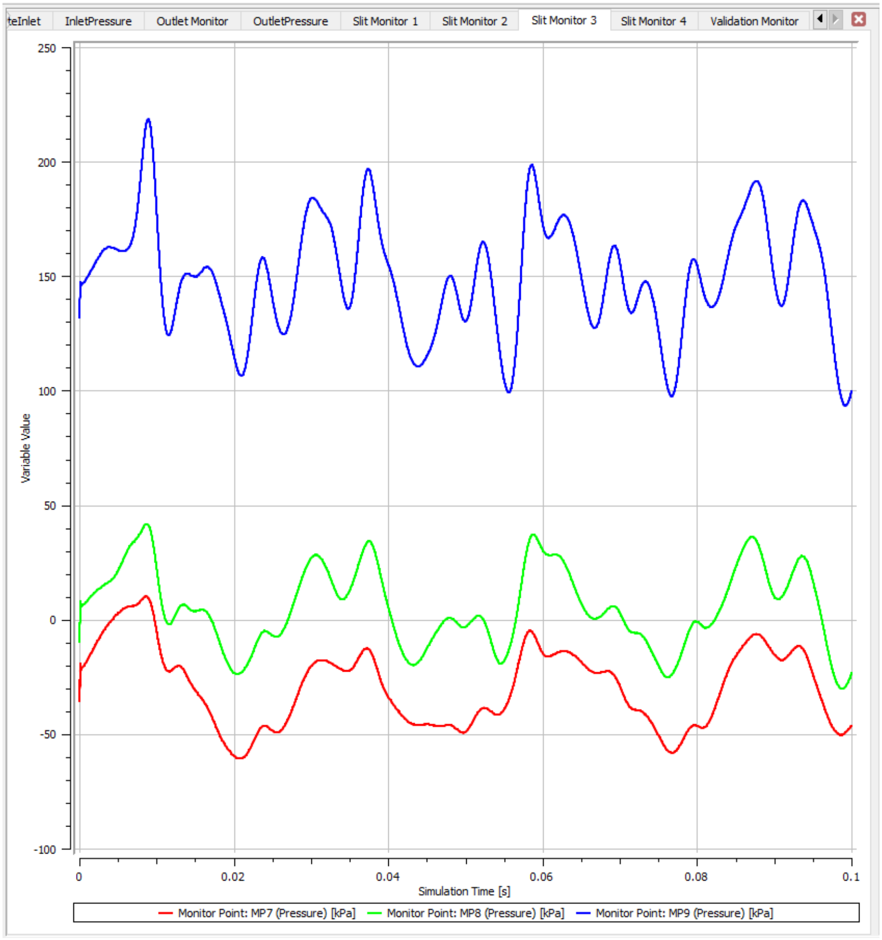

Figure C.8: Pressure values for monitor points 7-9 plotted against simulated time.

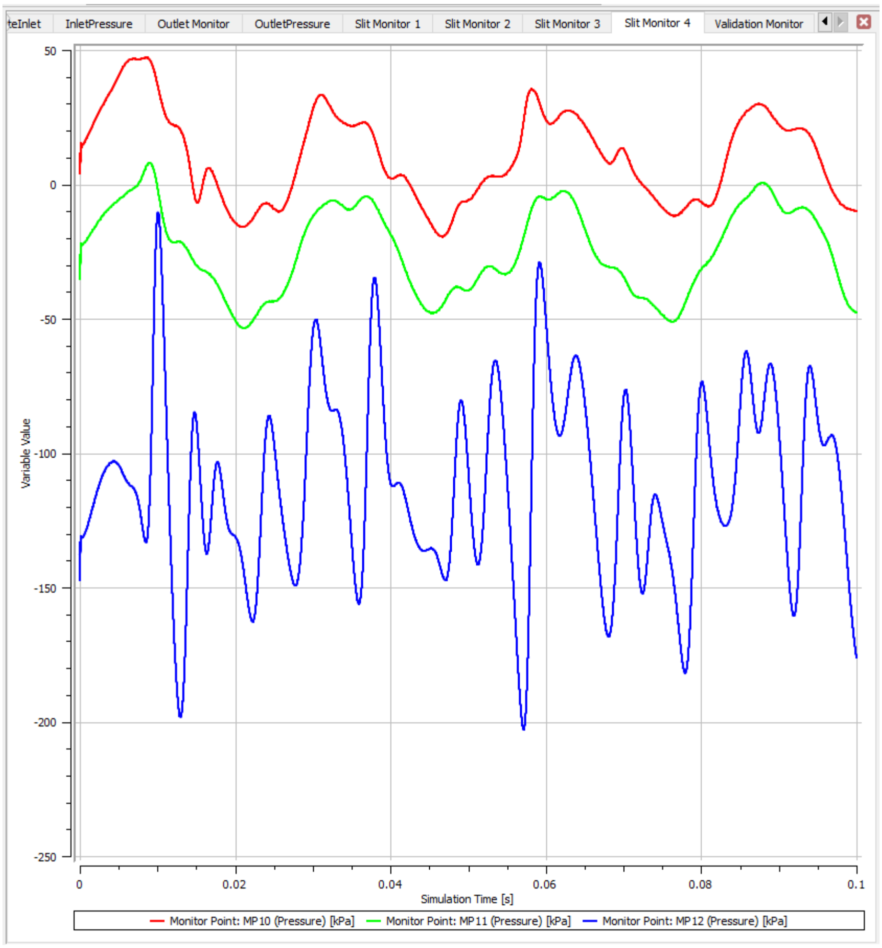

Figure C.9: Pressure values for monitor points 10-12 plotted against simulated time.

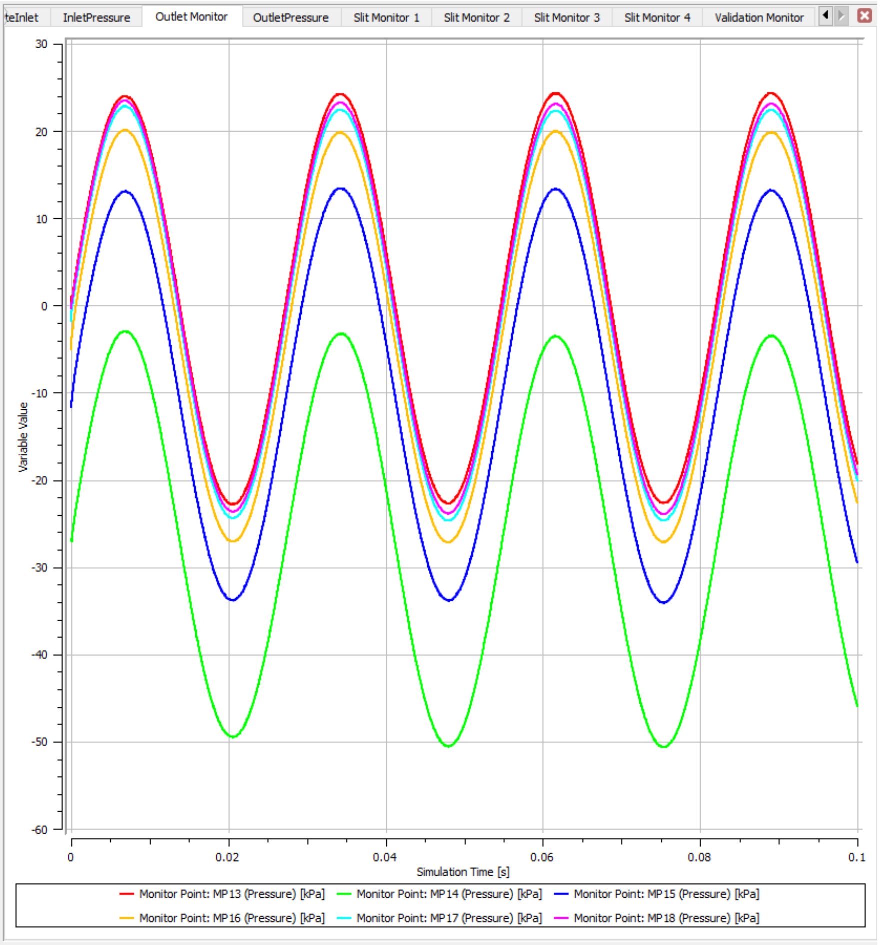

Figure C.10: Pressure values for monitor points 13-18 plotted against simulated time.

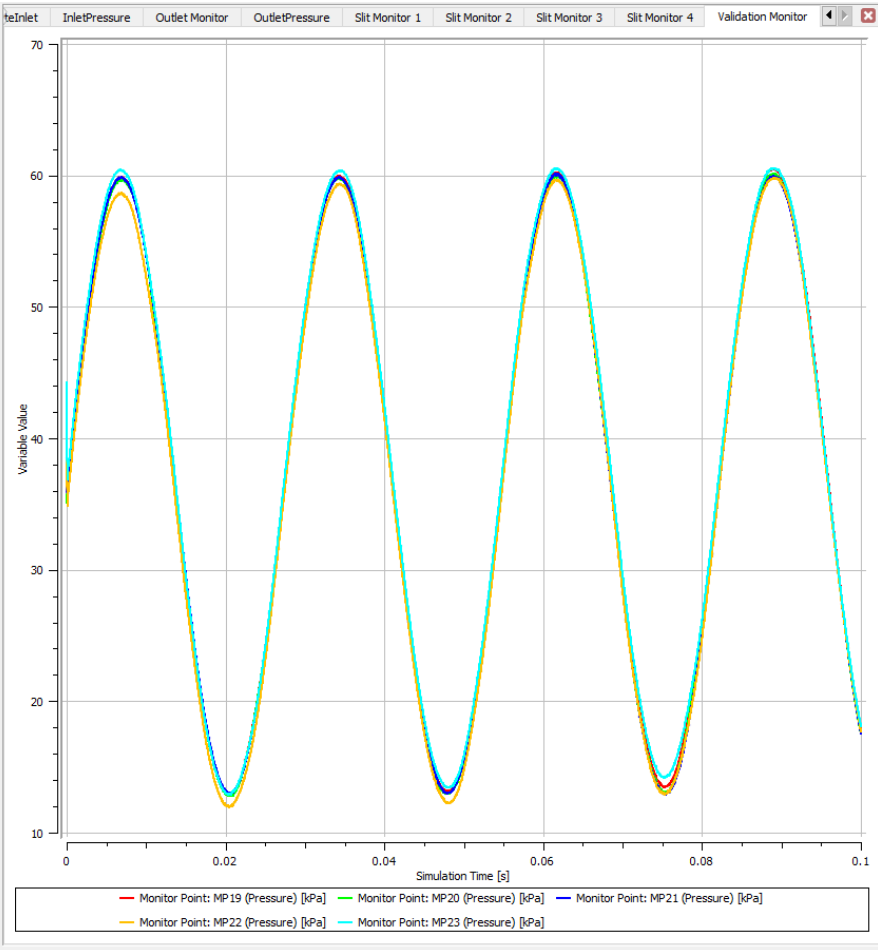

Figure C.11: Pressure values for monitor points 19-23 plotted against simulated time.

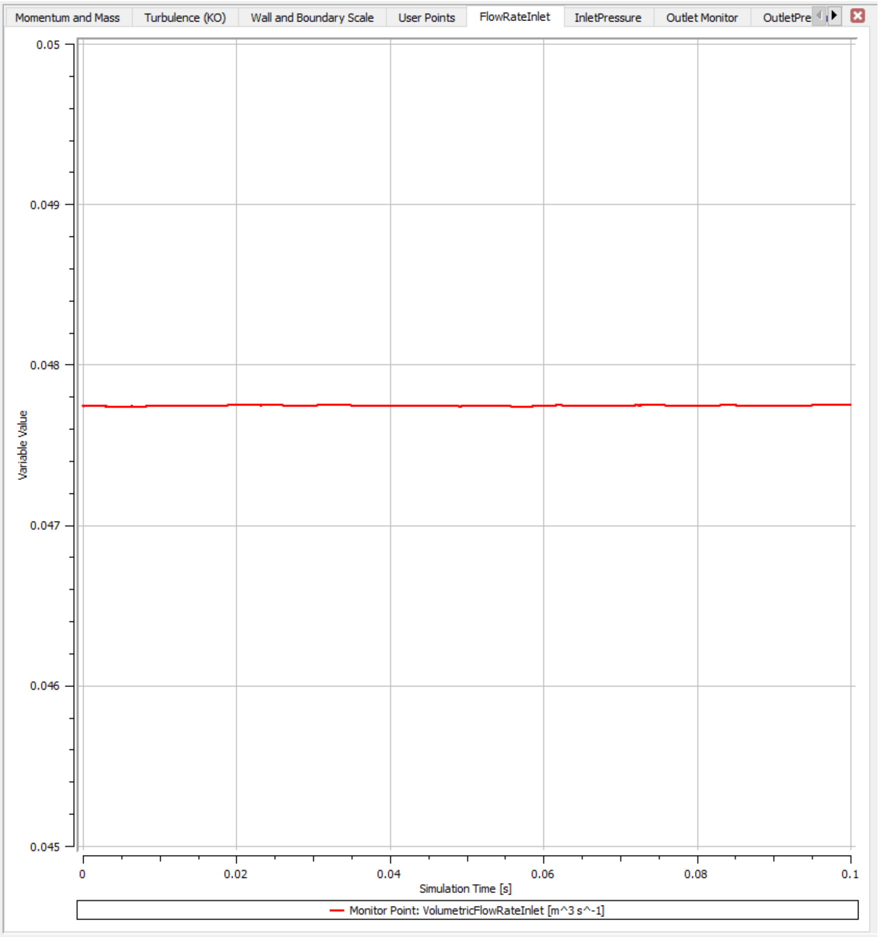

Figure C.12: Flow rate on the inlet plotted against simulated time. Used as consistency check for the inlet condition.

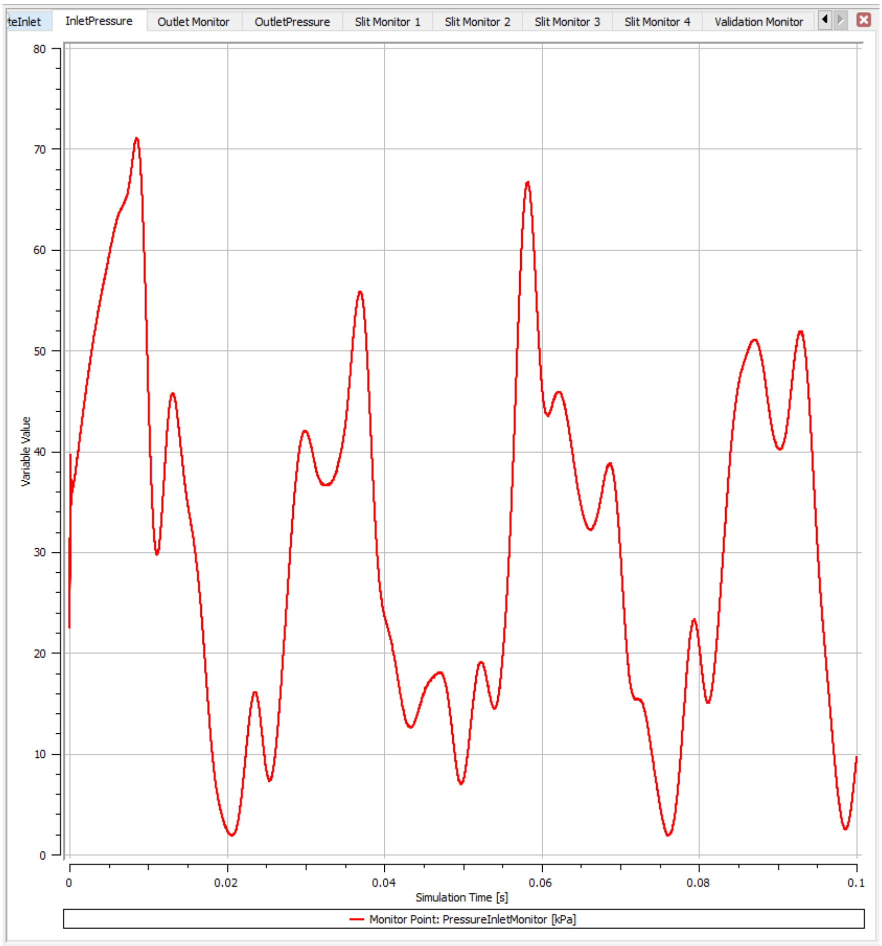

Figure C.13: Average pressure on the inlet plotted against simulated time.

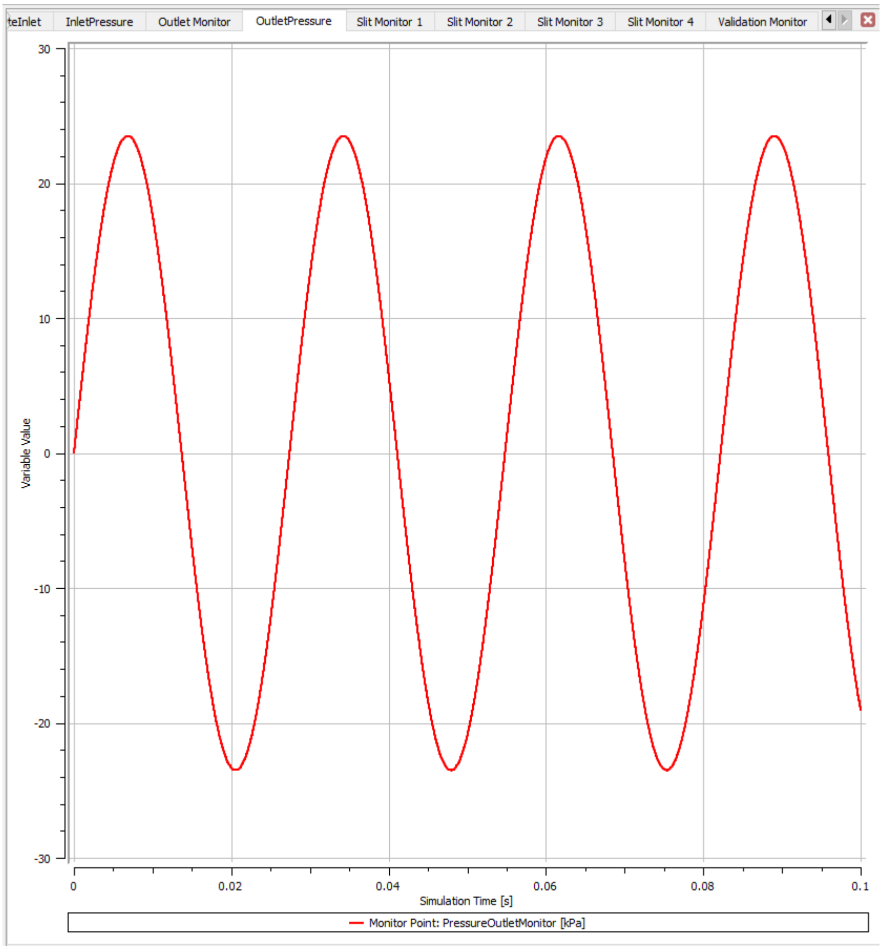

Figure C.14: Average pressure on the outlet plotted against simulated time. Used as consistency check for the outlet condition.

C.2.3 FFT plots

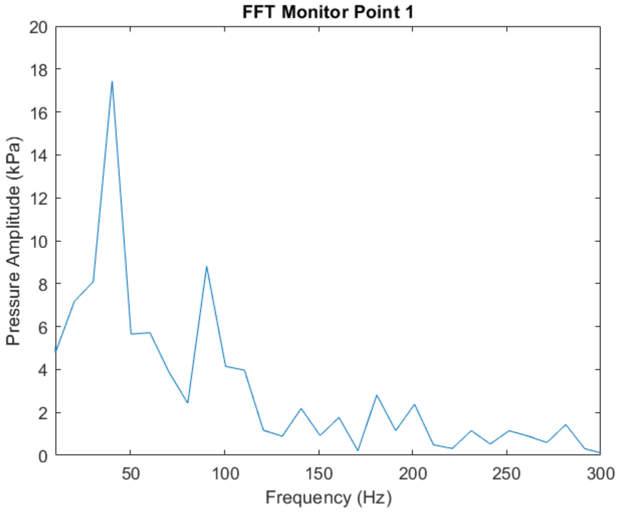

Figure C.15: FFT plot from monitor point 1 in figure C.6

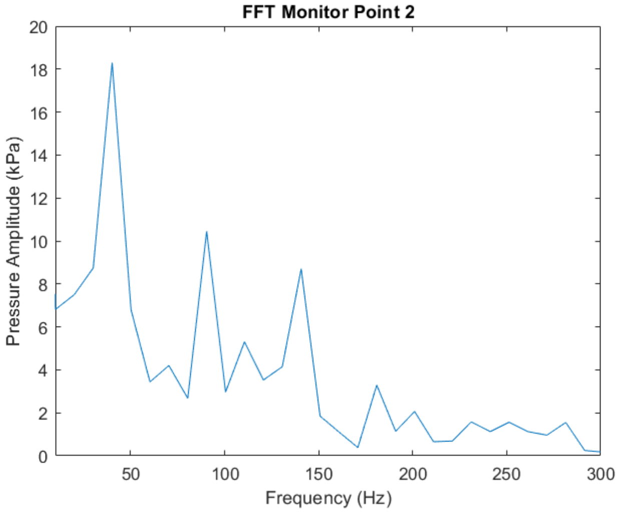

Figure C.16: FFT plot from monitor point 2 in figure C.6

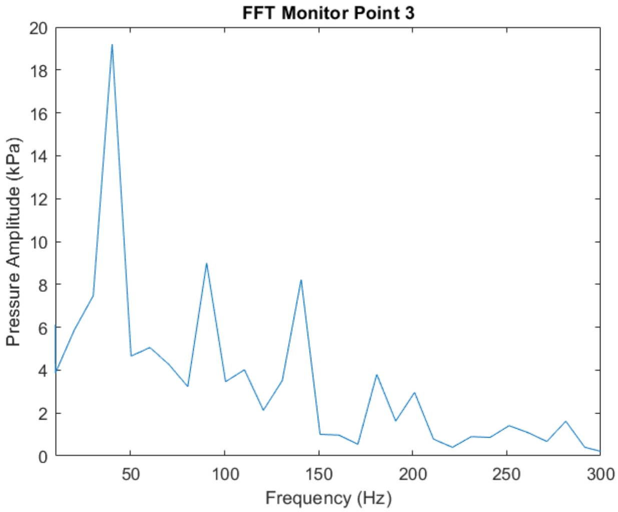

Figure C.17: FFT plot from monitor point 3 in figure C.6

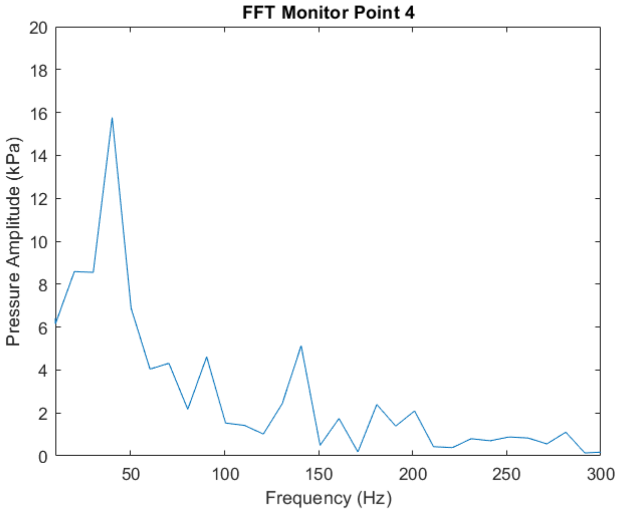

Figure C.18: FFT plot from monitor point 4 in figure C.7

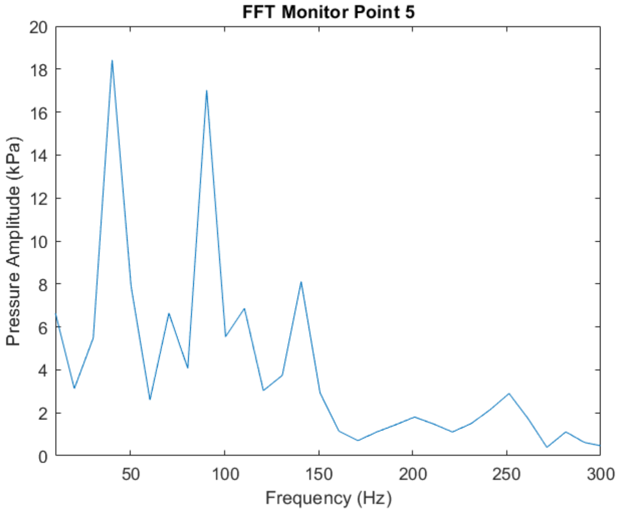

Figure C.19: FFT plot from monitor point 5 in figure C.7

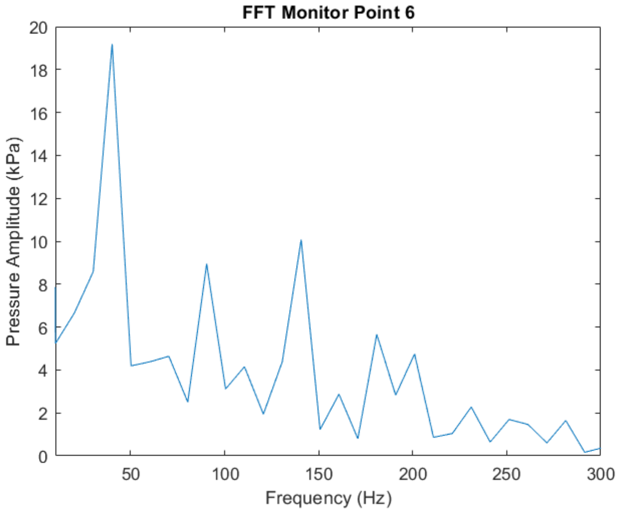

Figure C.20: FFT plot from monitor point 6 in figure C.7

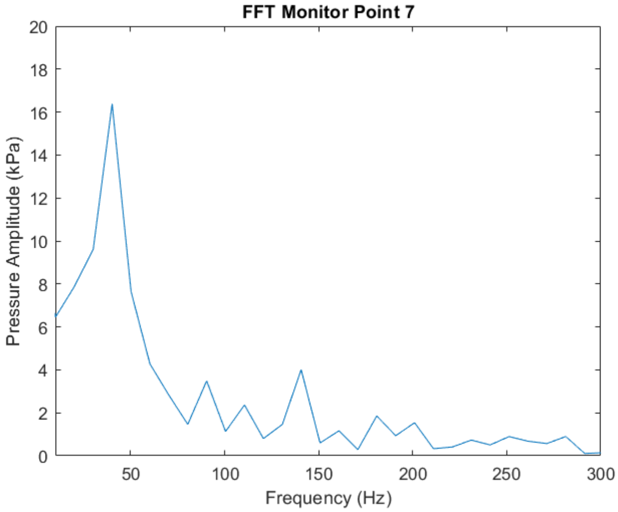

Figure C.21: FFT plot from monitor point 7 in figure C.8

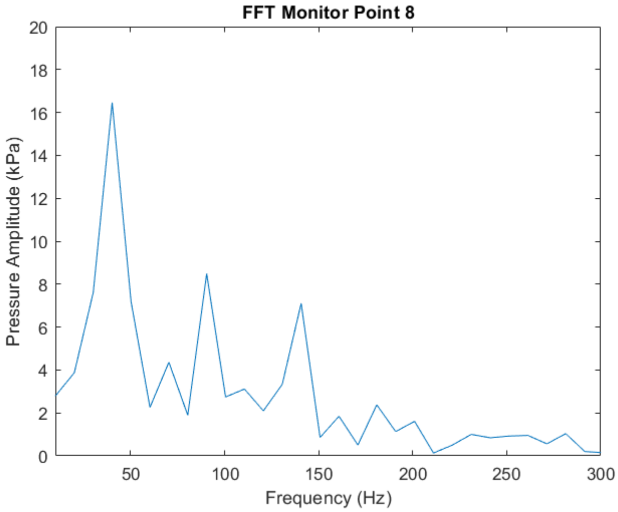

Figure C.22: FFT plot from monitor point 8 in figure C.8

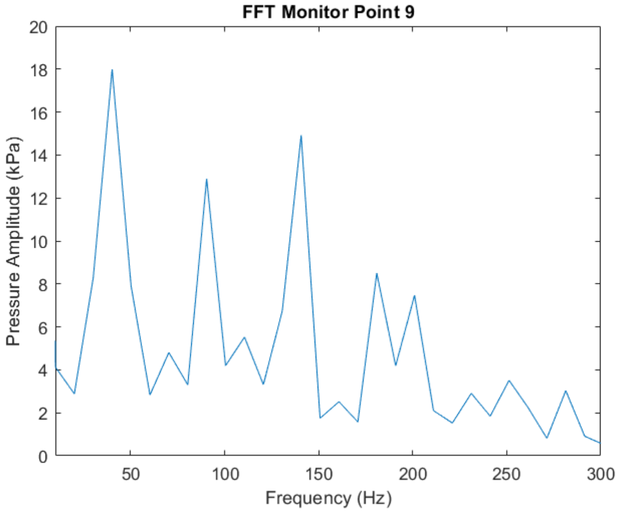

Figure C.23: FFT plot from monitor point 9 in figure C.8

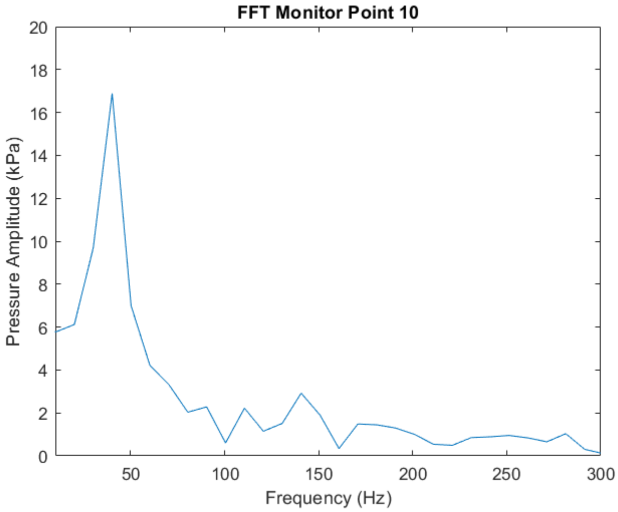

Figure C.24: FFT plot from monitor point 10 in figure C.9

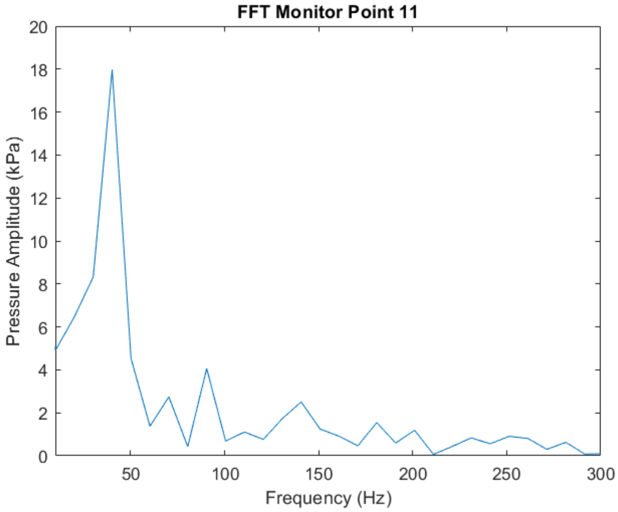

Figure C.25: FFT plot from monitor point 11 in figure C.9

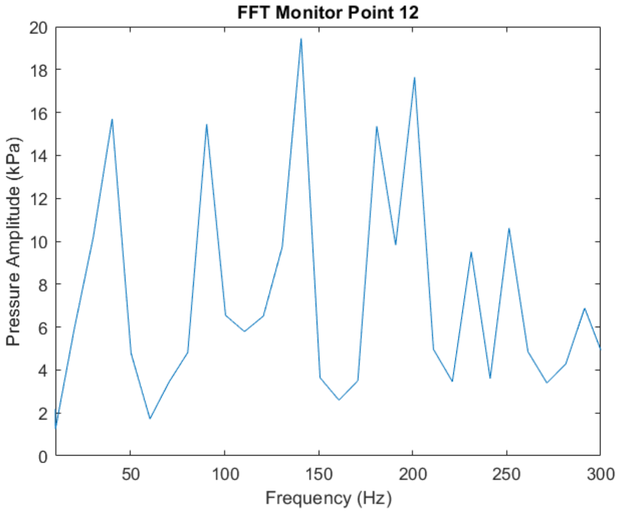

Figure C.26: FFT plot from monitor point 12 in figure C.9

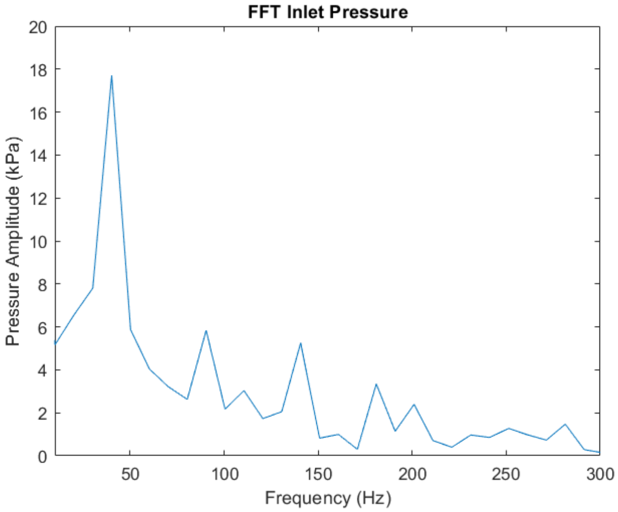

Figure C.27: FFT plot from average inlet pressure in figure C.13

```
clear all
close all

%Import data from csv file
Slit1Table=readtable('SlitMonitor.csv','HeaderLines',5);
%Transform from table to array
Slit1Array=table2array(Slit1Table);

%Extract time scale removing the offset in the first 100 measurements
t=Slit1Array(101:20000,1)-5*10^(-4);
%Extract pressure data from monitor points in the csv file
MP1=Slit1Array(101:20000,2);
MP2=Slit1Array(101:20000,3);
MP3=Slit1Array(101:20000,4);

%Define sampling frequency
Fs=200000;
%Define sampling period
Ts=1/Fs;
%Define sampling length
L=size(MP1);
L=L(1);

%Perform fast fourier transform on the data
Y1=fft(MP1);
Y2=fft(MP2);
Y3=fft(MP3);

%Compute two sided spectrum
P21=abs(Y1/L);
%Compute one sided spectrum
P11=P21(1:L/2+1);
P11(2:end-1) = 2*P11(2:end-1);

%Compute spectrums for second dataset
P22=abs(Y2/L);
P12=P22(1:L/2+1);
P12(2:end-1) = 2*P12(2:end-1);

%Compute spectrums for third dataset
P23=abs(Y3/L);
P13=P23(1:L/2+1);
P13(2:end-1) = 2*P13(2:end-1);

f=Fs*(0:(L/2))/L;                        %Define the frequency scale

%Plot Amplitude vs frequency for the three datasets.
figure
plot(f,P11)
xlabel('Frequency (Hz)')
ylabel('Pressure Amplitude (kPa)')
title('FFT Monitor point x1')
```

```
axis([10 300 0 20])

figure
plot(f,P12)
xlabel('Frequency (Hz)')
ylabel('Pressure Amplitude (kPa)')
title('FFT Monitor Point x2')
axis([10 300 0 20])

figure
plot(f,P13)
xlabel('Frequency (Hz)')
ylabel('Pressure Amplitude (kPa)')
title('FFT Monitor Point x3')
axis([10 300 0 20])
```

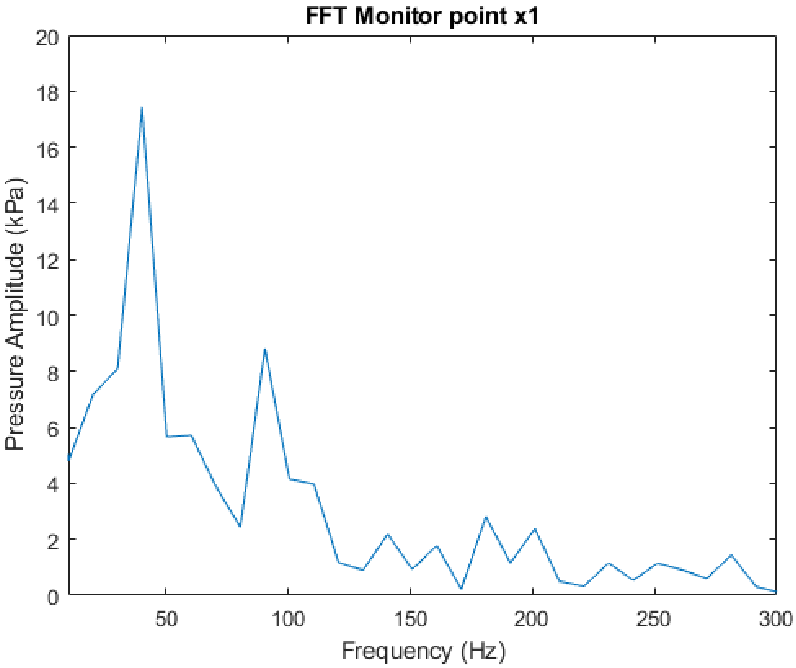

C.3 Pre study tangential velocity

C.3.1 Residuals

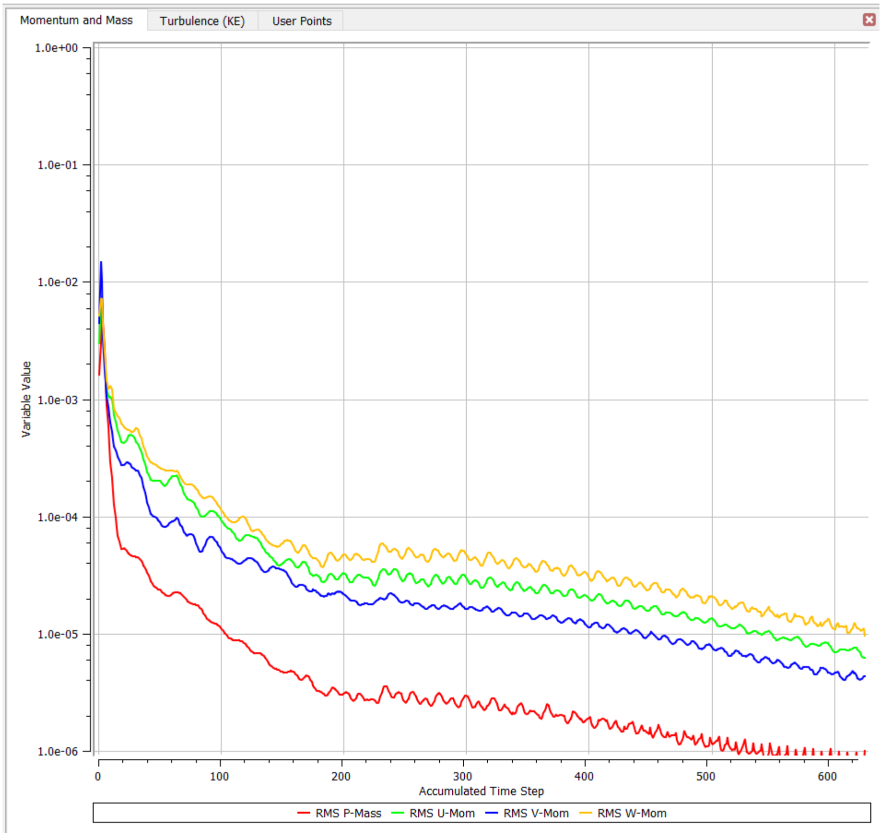

Figure C.28: Residuals from pre study on reduction of volume below the head cover.

C.3.2 Monitor Points

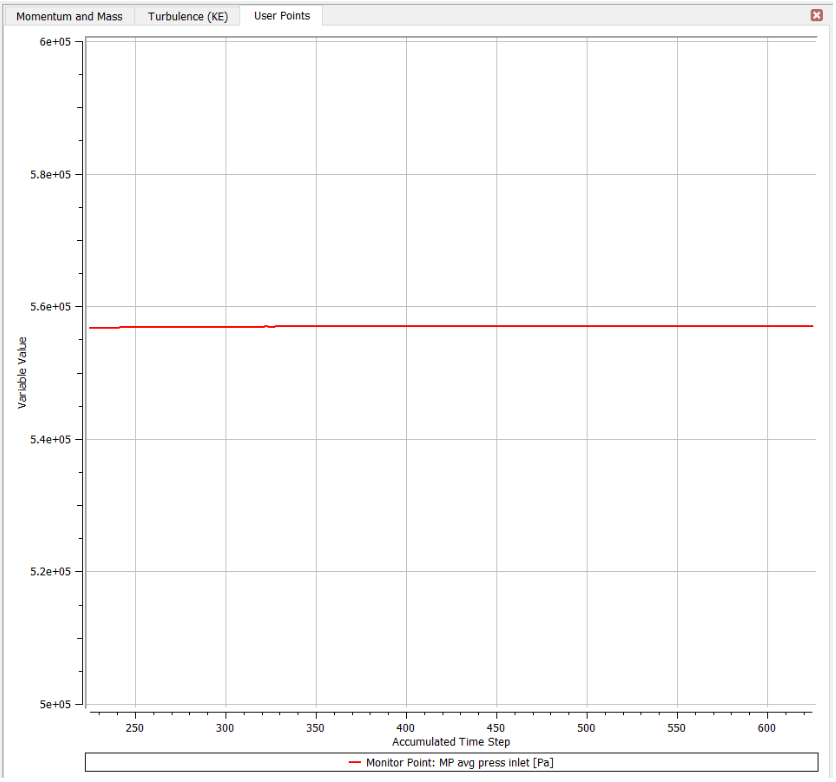

Figure C.29: Monitor point displaying convergence of the inlet pressure for the pre study on volume reduction below the head cover.

C.4 Mesh Convergence Data

C.4.1 Mesh 1

Residuals

Figure C.30: RMS-residuals from steady state initialisation on mesh 1.

Figure C.31: Max-residuals from steady state initialisation on mesh 1.

Imbalances

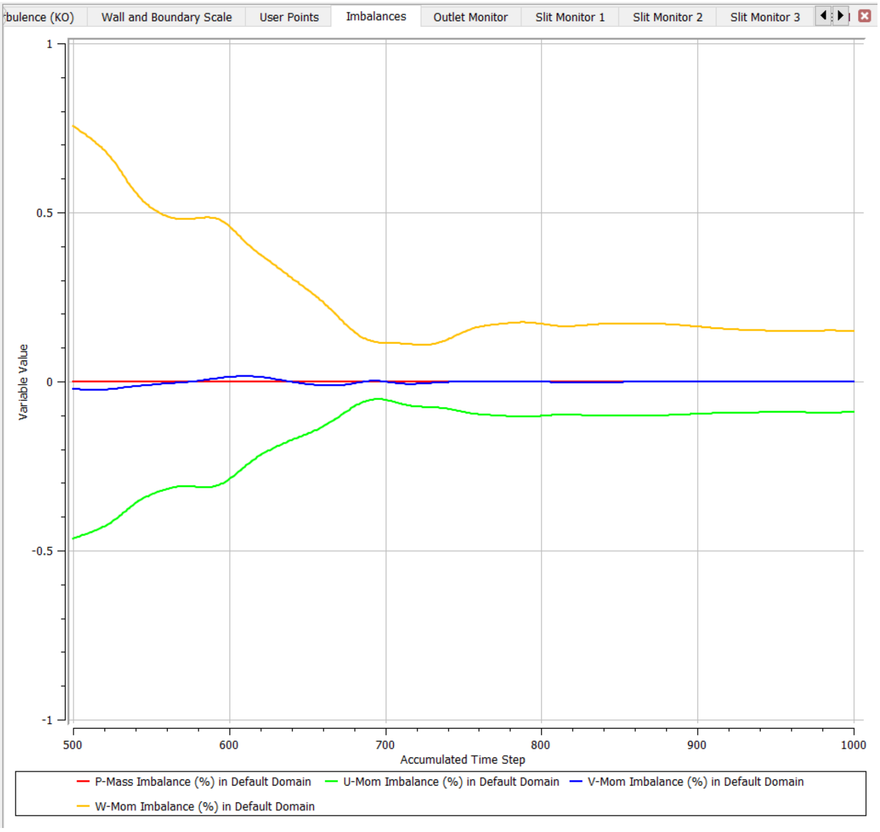

Figure C.32: Imbalances from steady state initialisation on mesh 1.

Monitor Points

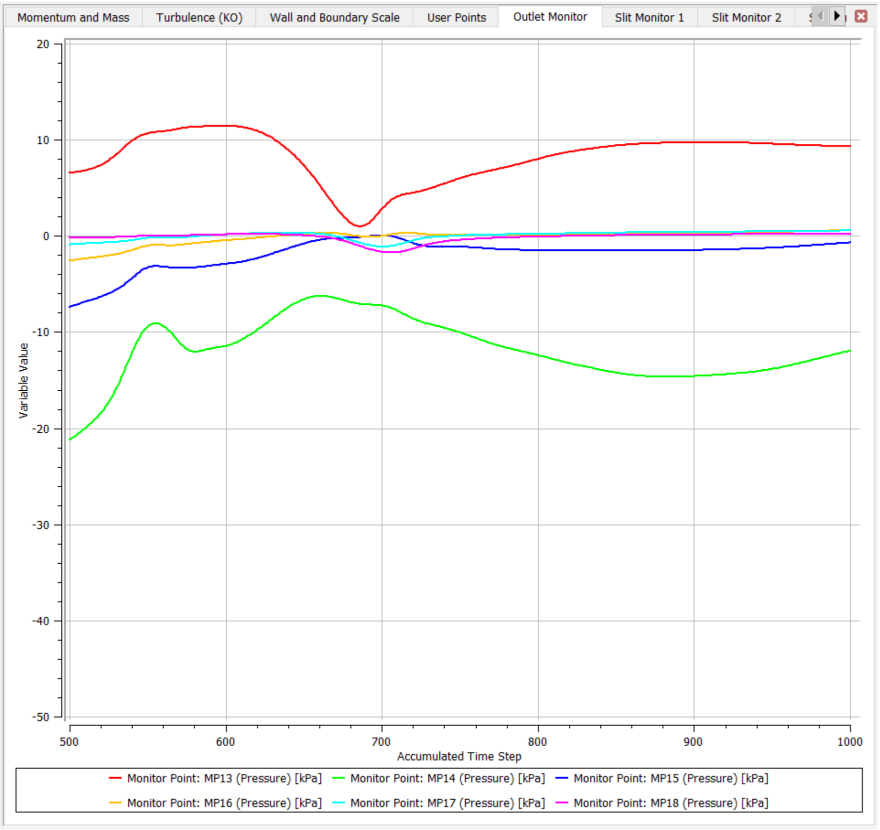

Figure C.33: Outlet monitor points 13-18 from steady state initialisation on mesh 1.

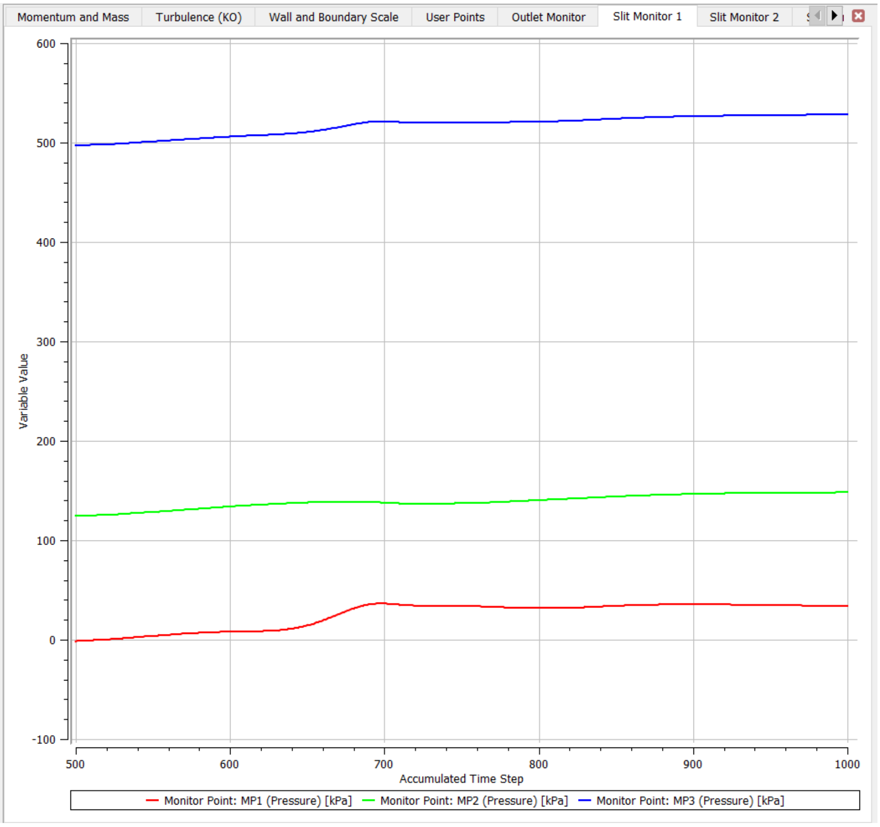

Figure C.34: Slit monitor points 1-3 from steady state initialisation on mesh 1.

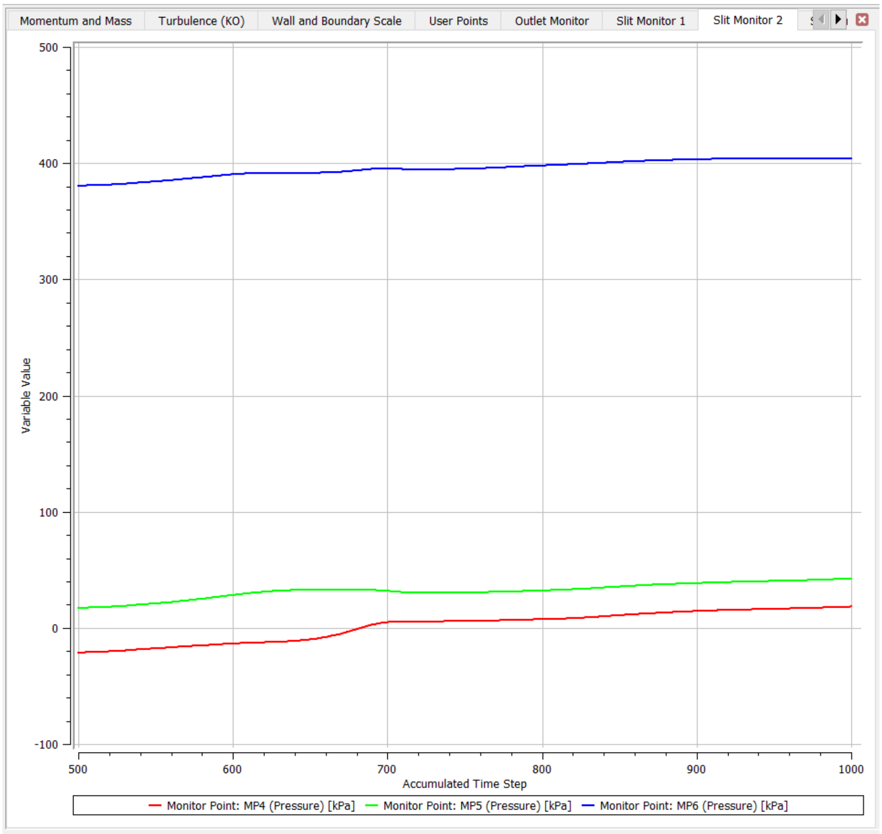

Figure C.35: Slit monitor points 4-6 from steady state initialisation on mesh 1.

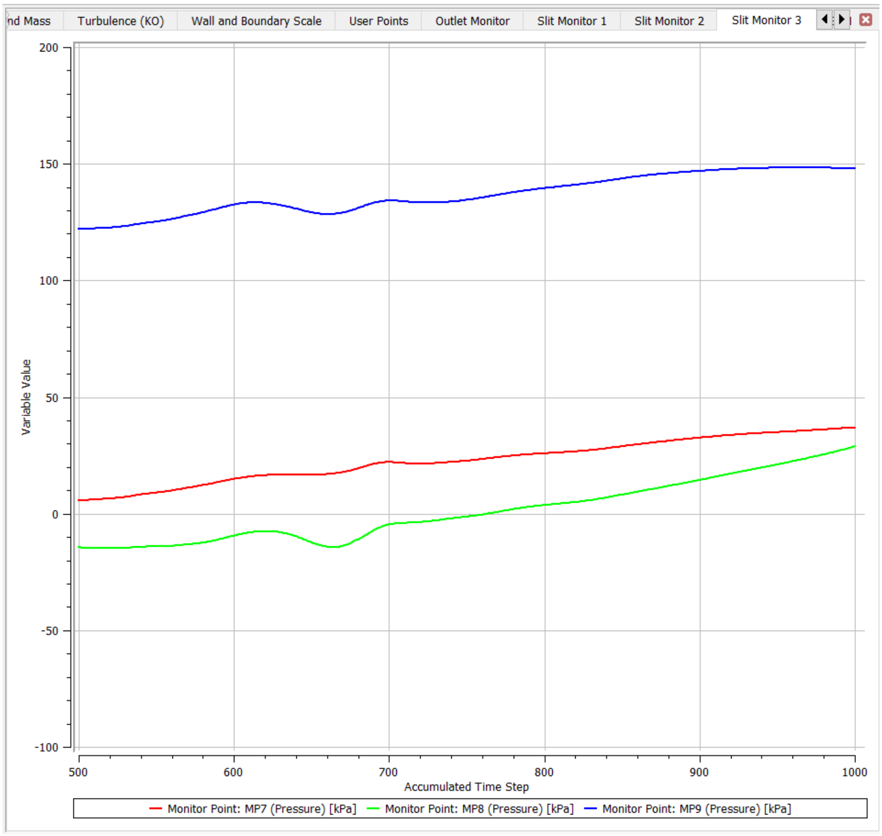

Figure C.36: Slit monitor points 7-9 from steady state initialisation on mesh 1.

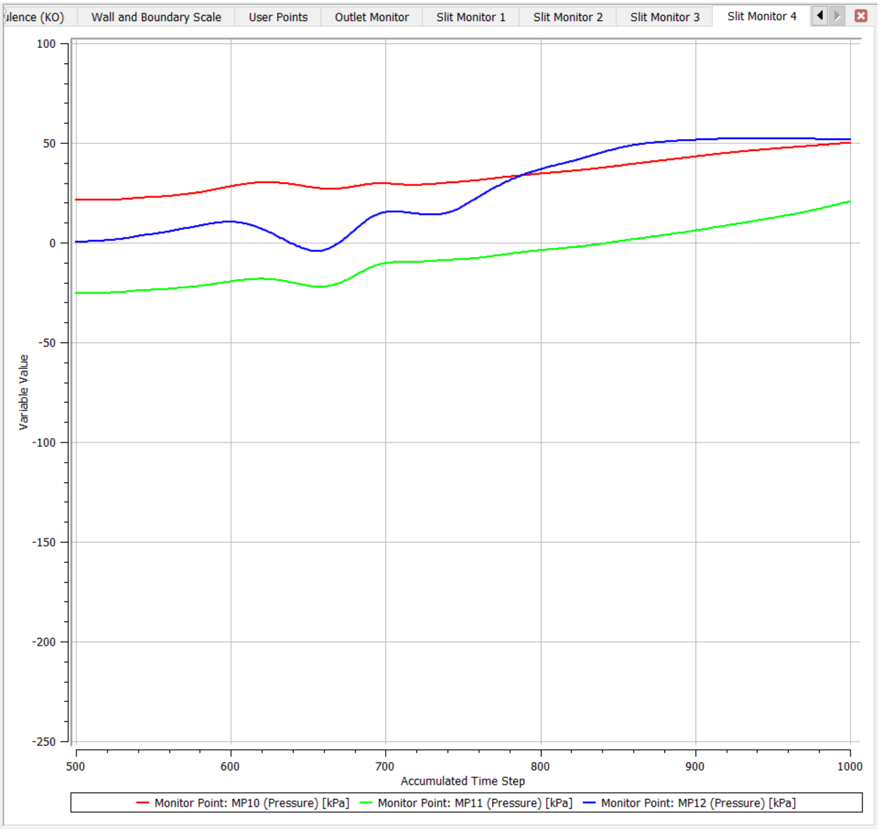

Figure C.37: Slit monitor points 10-12 from steady state initialisation on mesh 1.

C.4.2 Mesh 2

Residuals

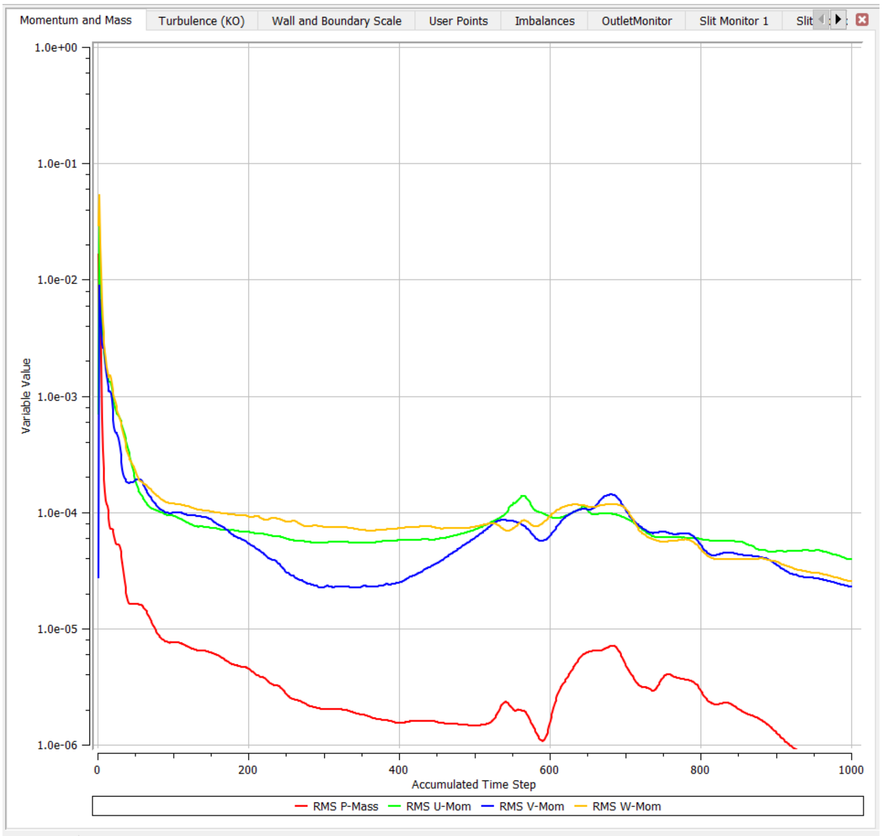

Figure C.38: RMS-residuals from steady state initialisation on mesh 2.

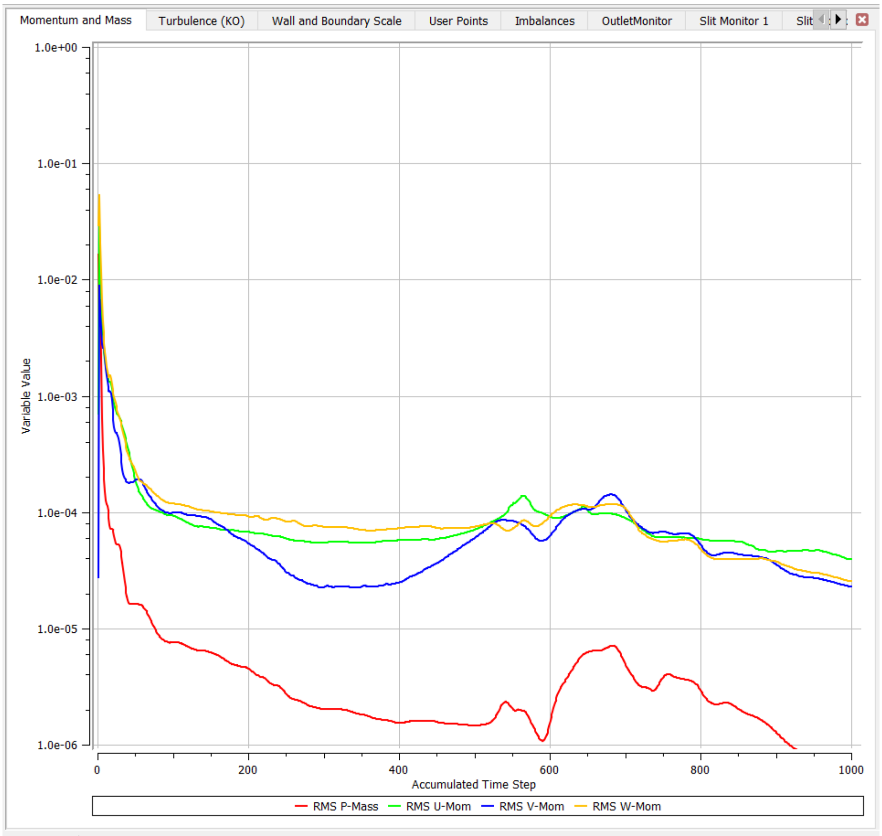

Figure C.39: Max-residuals from steady state initialisation on mesh 2.

Imbalances

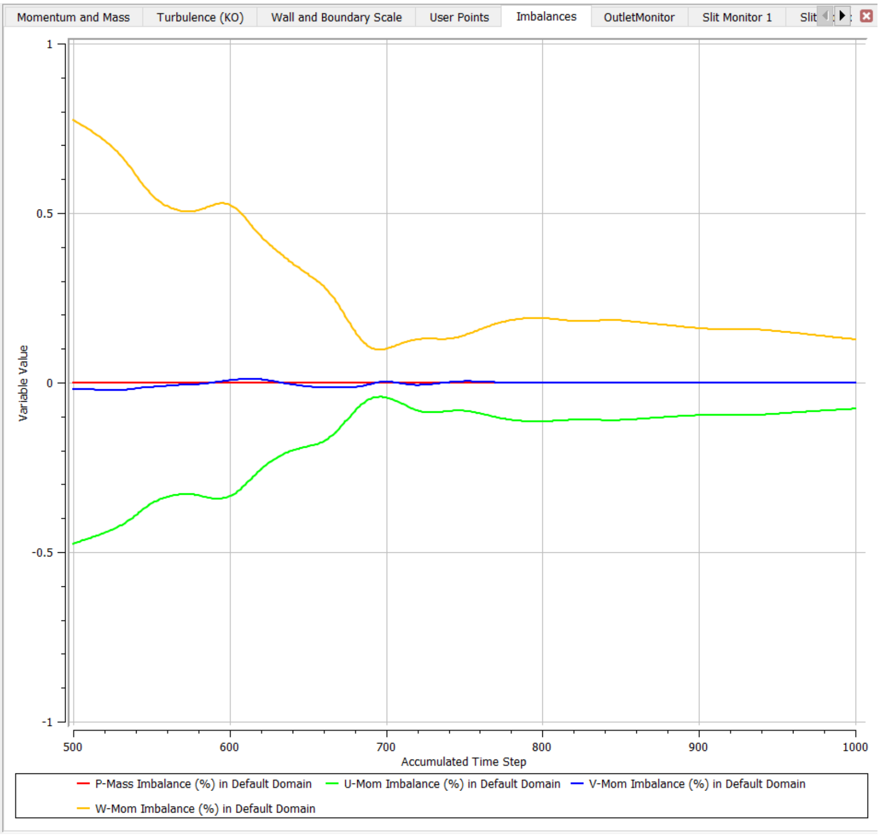

Figure C.40: Imbalances from steady state initialisation on mesh 2.

Monitor Points

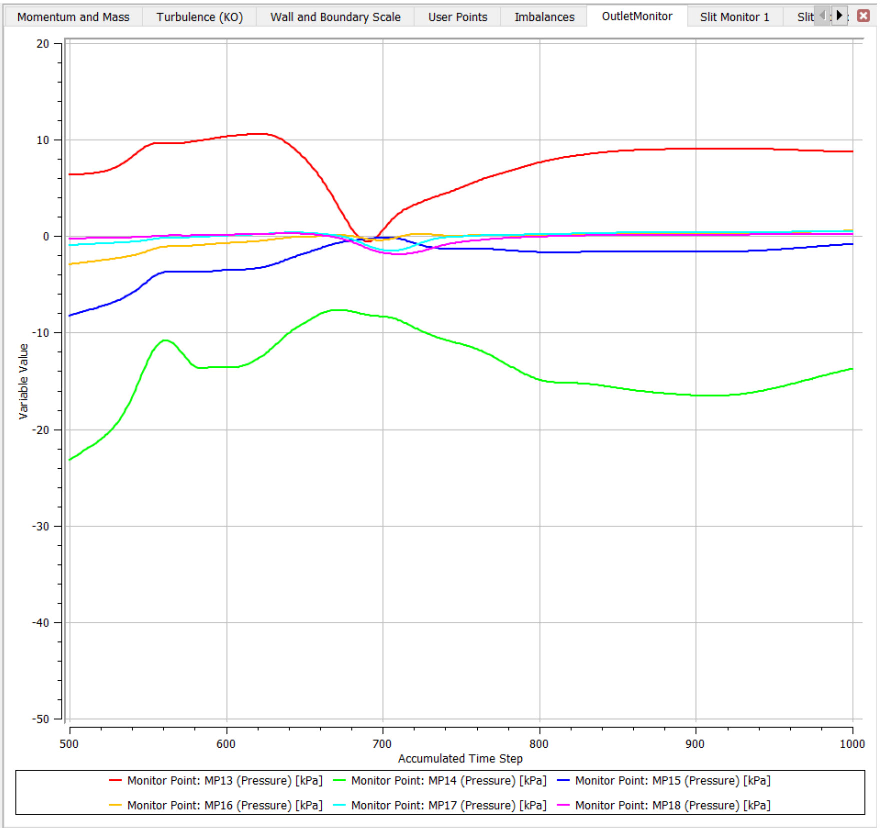

Figure C.41: Outlet monitor points 13-18 from steady state initialisation on mesh 2.

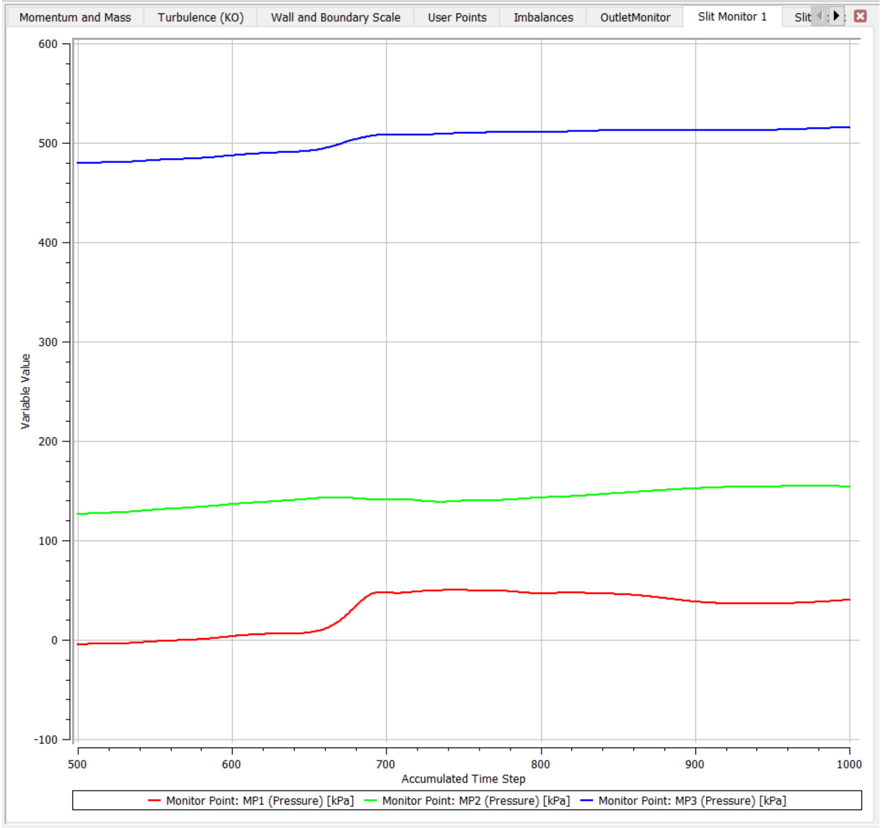

Figure C.42: Slit monitor points 1-3 from steady state initialisation on mesh 2.

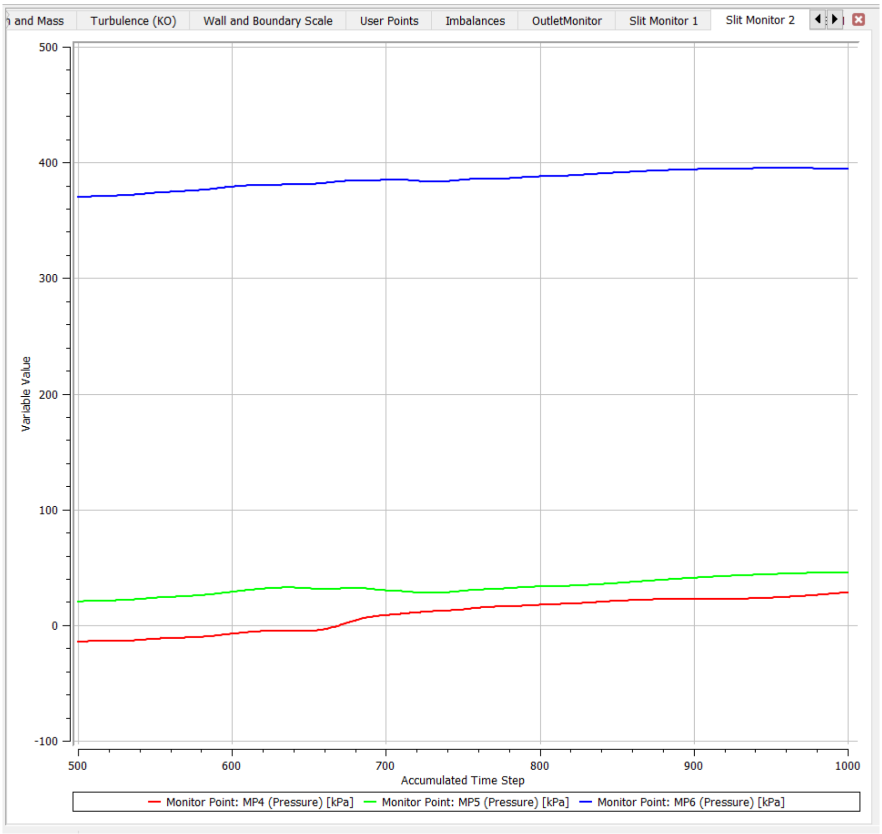

Figure C.43: Slit monitor points 4-6 from steady state initialisation on mesh 2.

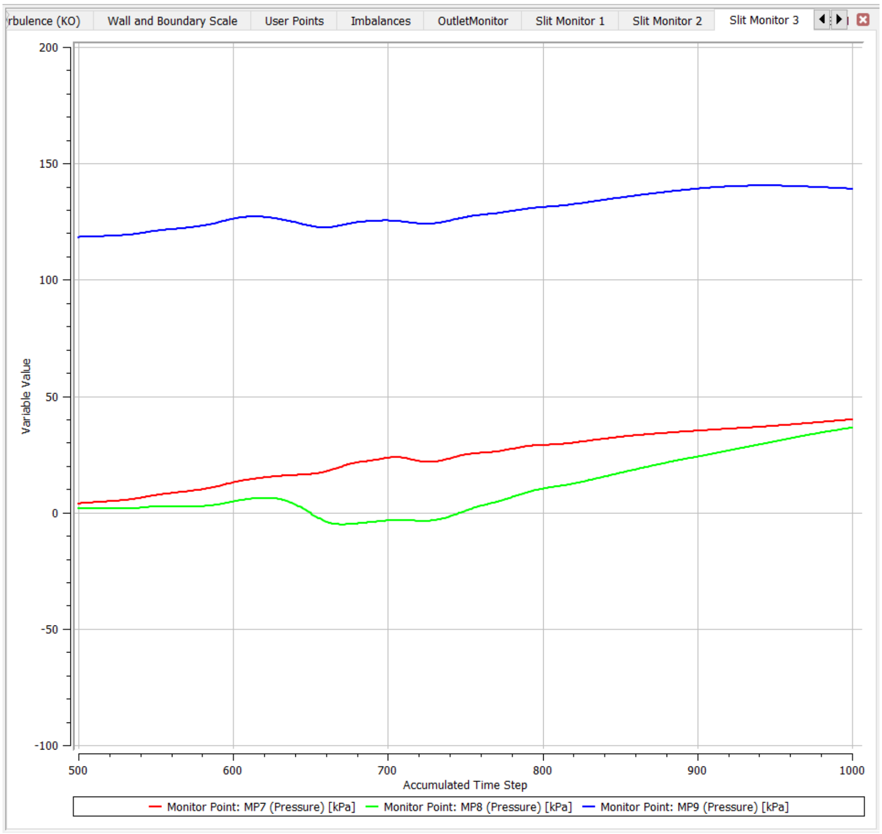

Figure C.44: Slit monitor points 7-9 from steady state initialisation on mesh 2.

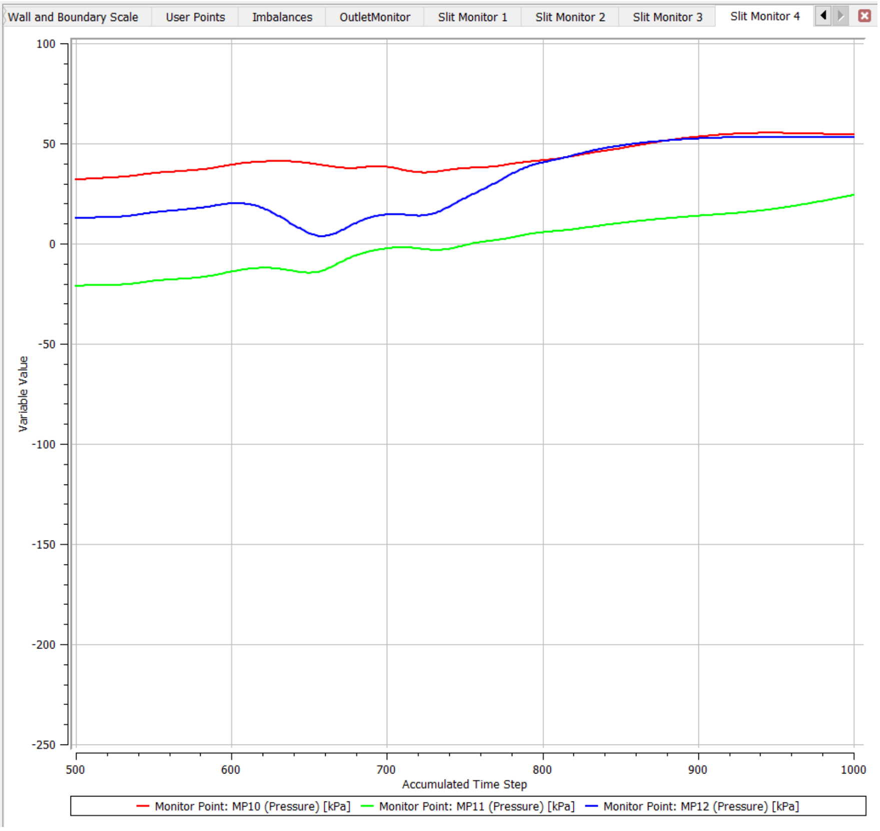

Figure C.45: Slit monitor points 10-12 from steady state initialisation on mesh 2.

C.4.3 Mesh 3

Residuals

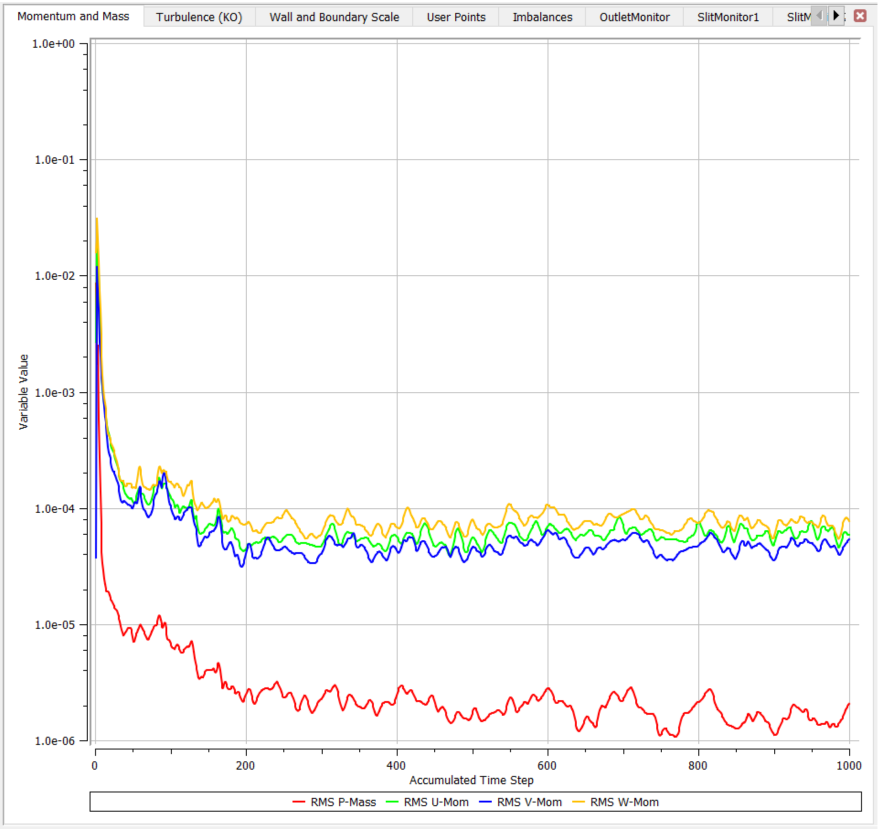

Figure C.46: RMS-residuals from steady state initialisation on mesh 3.

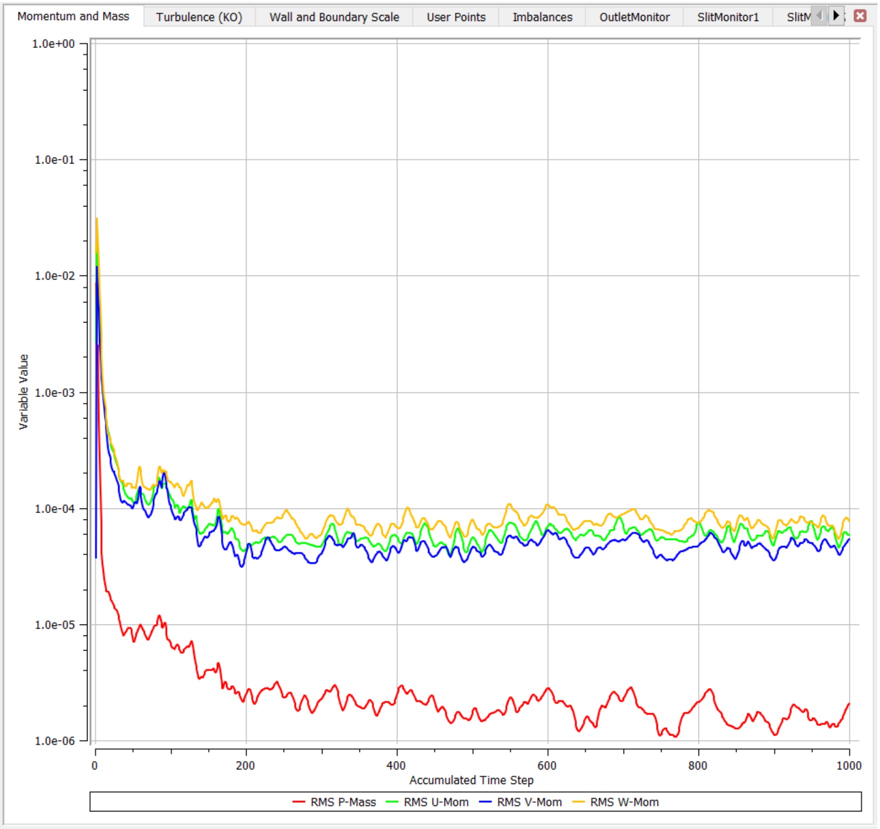

Figure C.47: Max-residuals from steady state initialisation on mesh 3.

Imbalances

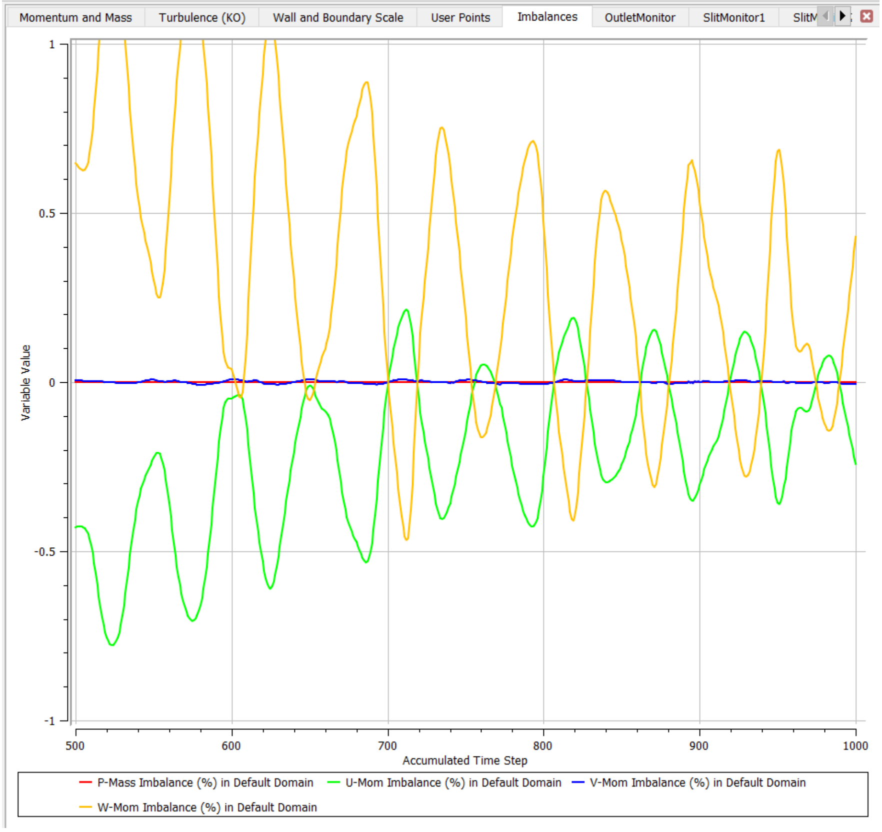

Figure C.48: Imbalances from steady state initialisation on mesh 3.

Monitor Points

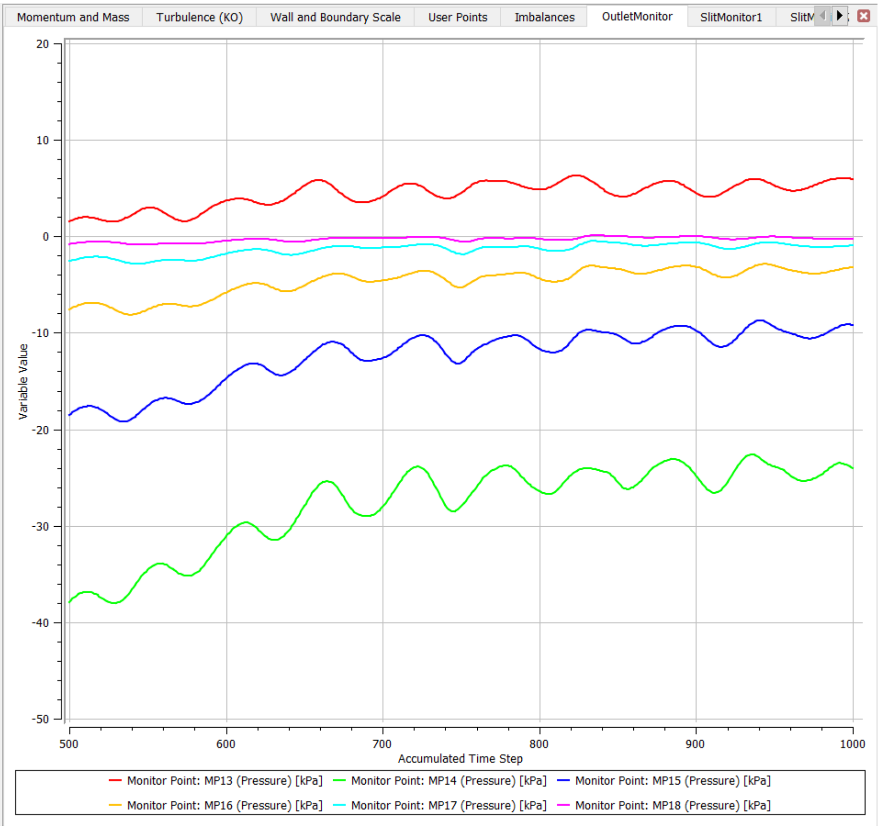

Figure C.49: Outlet monitor points 13-18 from steady state initialisation on mesh 3.

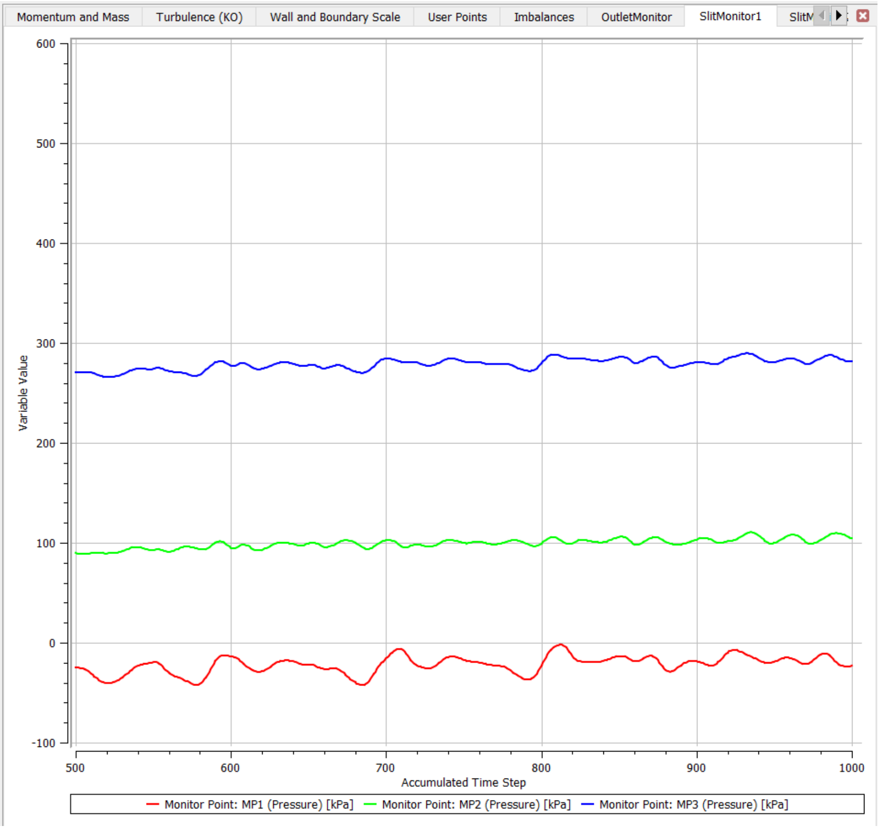

Figure C.50: Slit monitor points 1-3 from steady state initialisation on mesh 3.

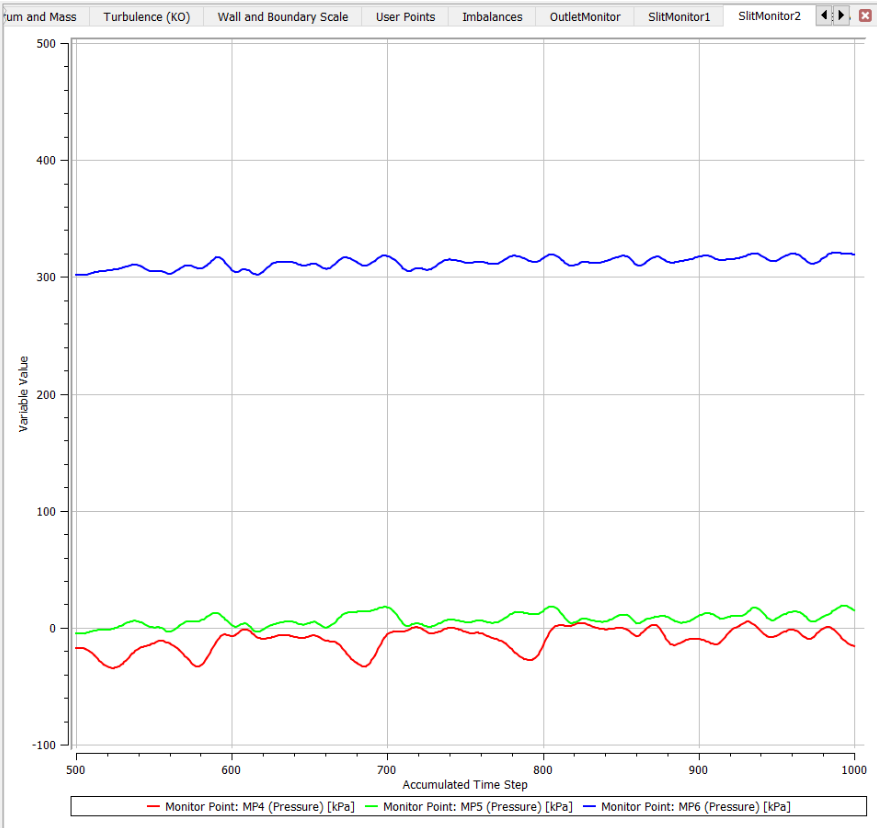

Figure C.51: Slit monitor points 4-6 from steady state initialisation on mesh 3.

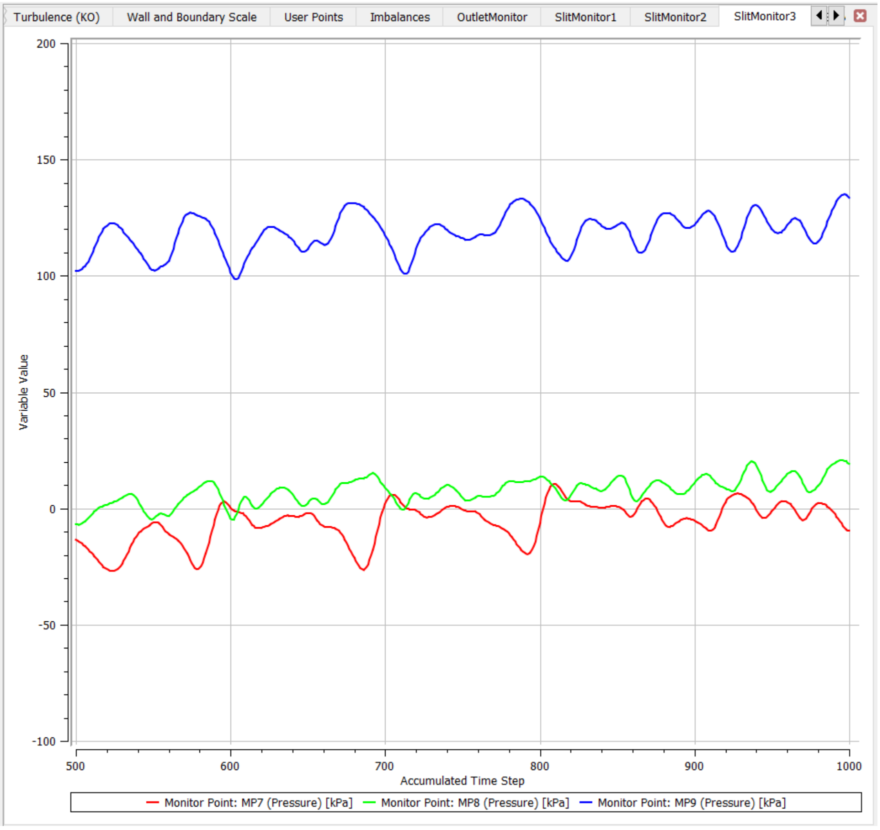

Figure C.52: Slit monitor points 7-9 from steady state initialisation on mesh 3.

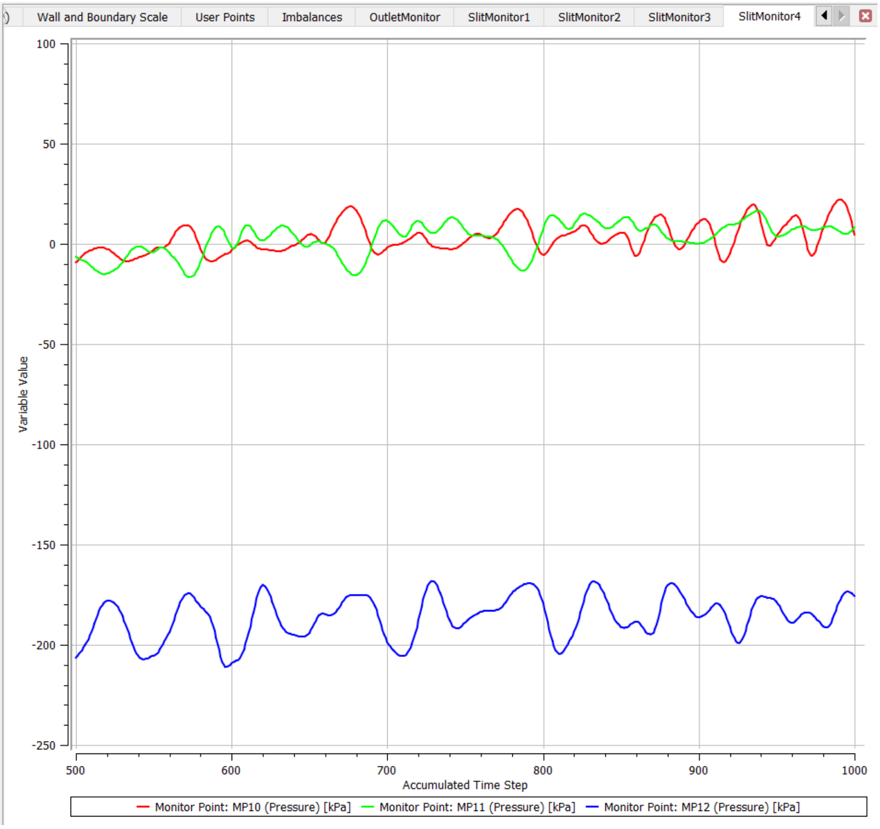

Figure C.53: Slit monitor points 10-12 from steady state initialisation on mesh 3.

C.4.4 Mesh 4

Residuals

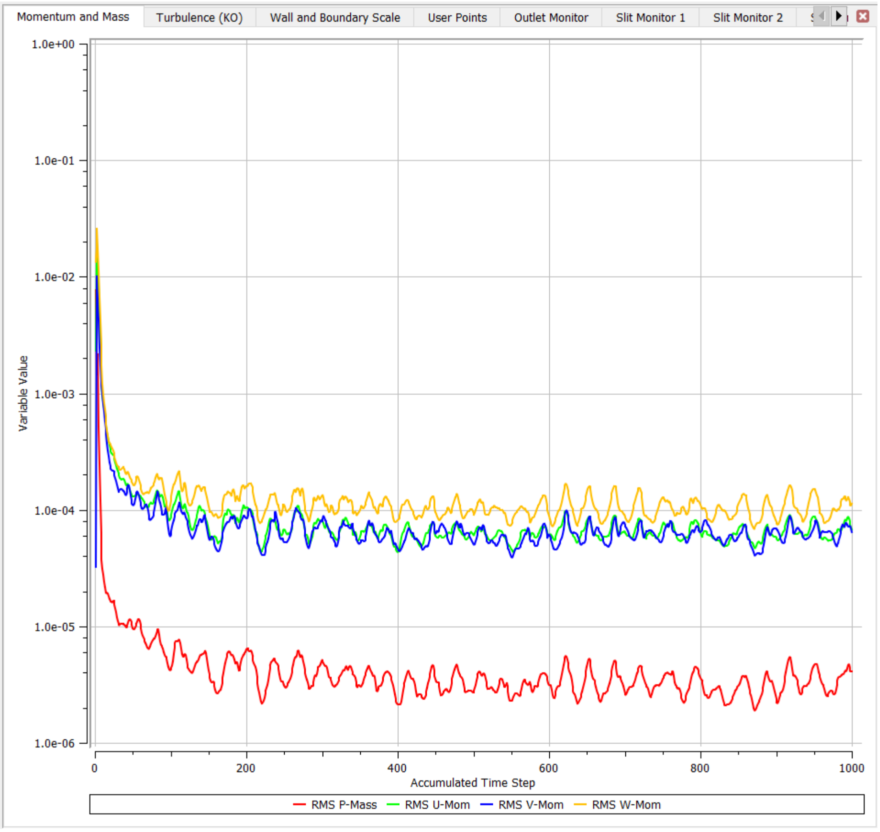

Figure C.54: RMS-residuals from steady state initialisation on mesh 4.

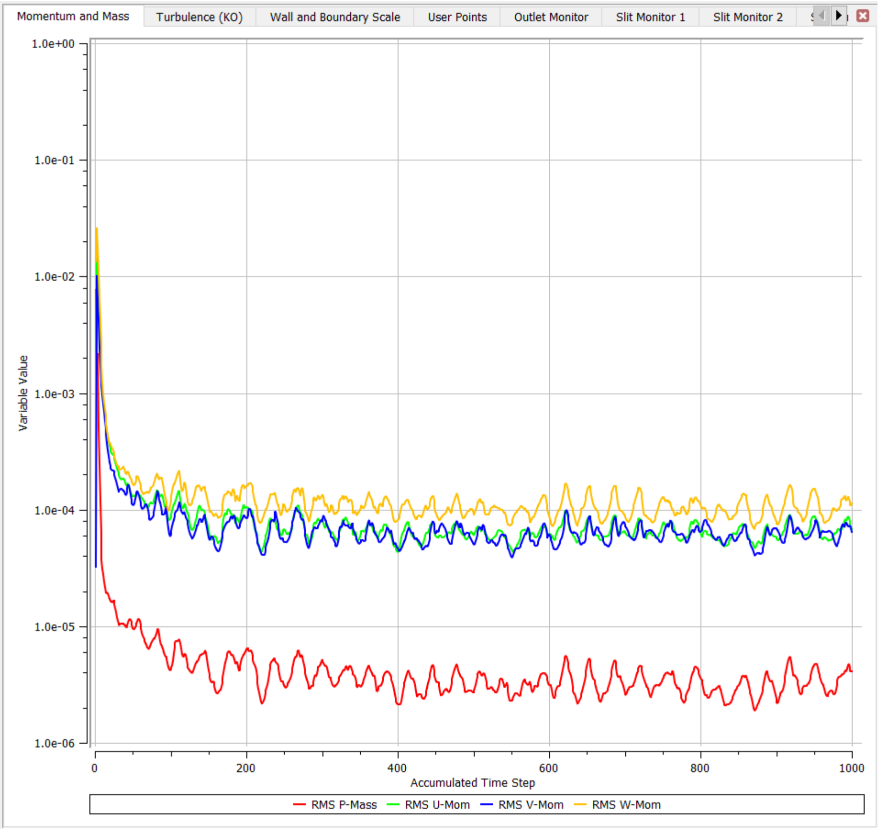

Figure C.55: Max-residuals from steady state initialisation on mesh 4.

Imbalances

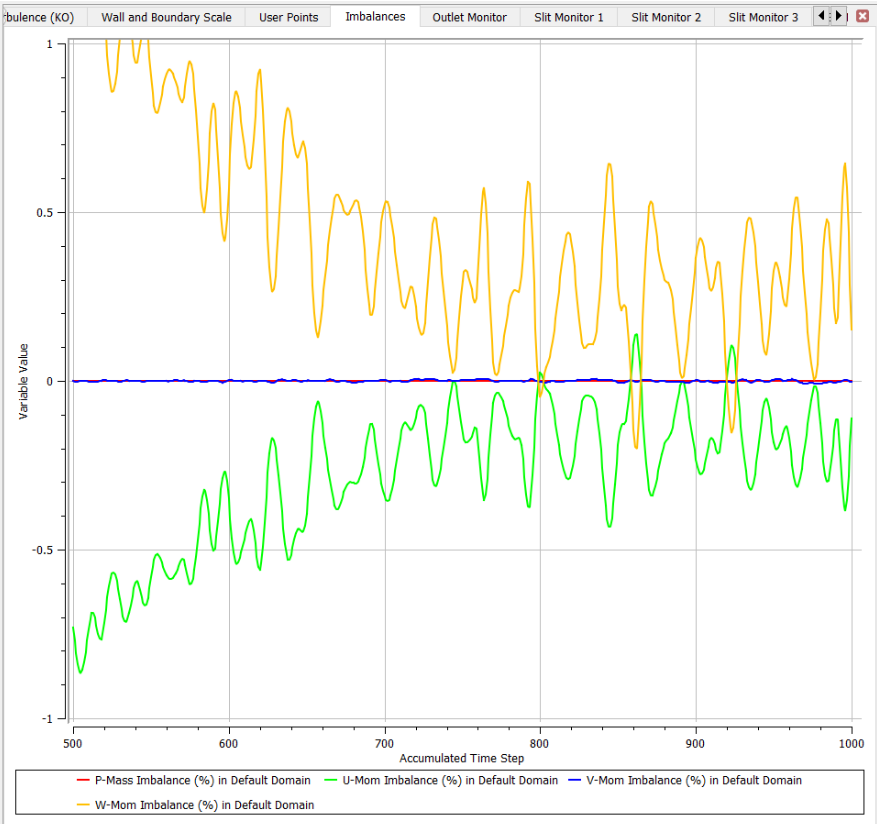

Figure C.56: Imbalances from steady state initialisation on mesh 4.

Monitor Points

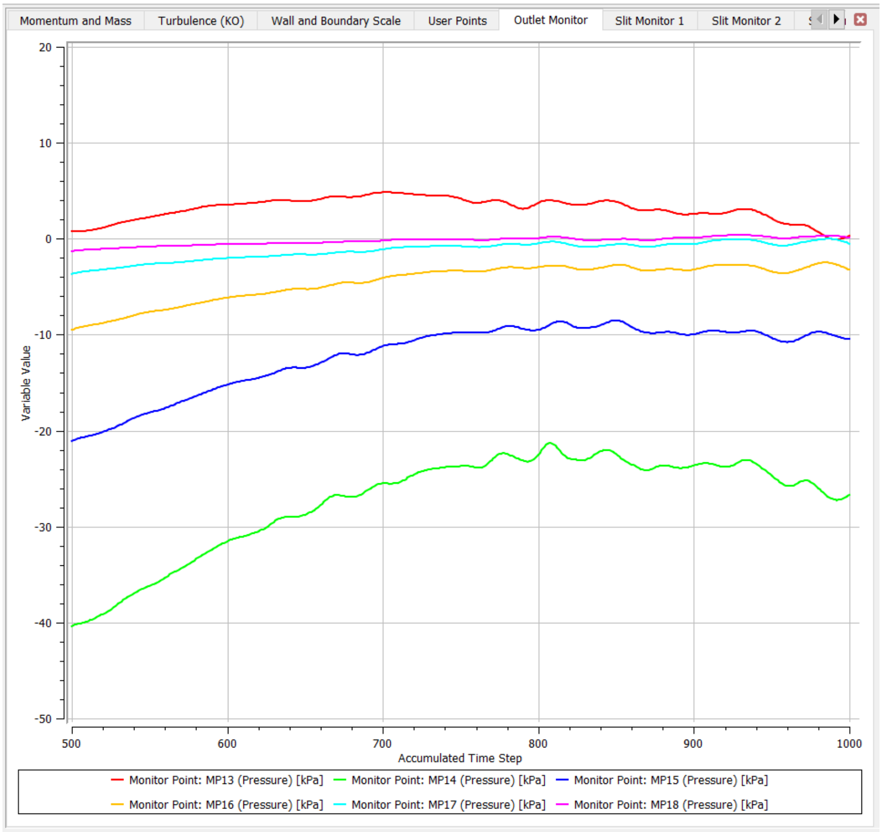

Figure C.57: Outlet monitor points 13-18 from steady state initialisation on mesh 4.

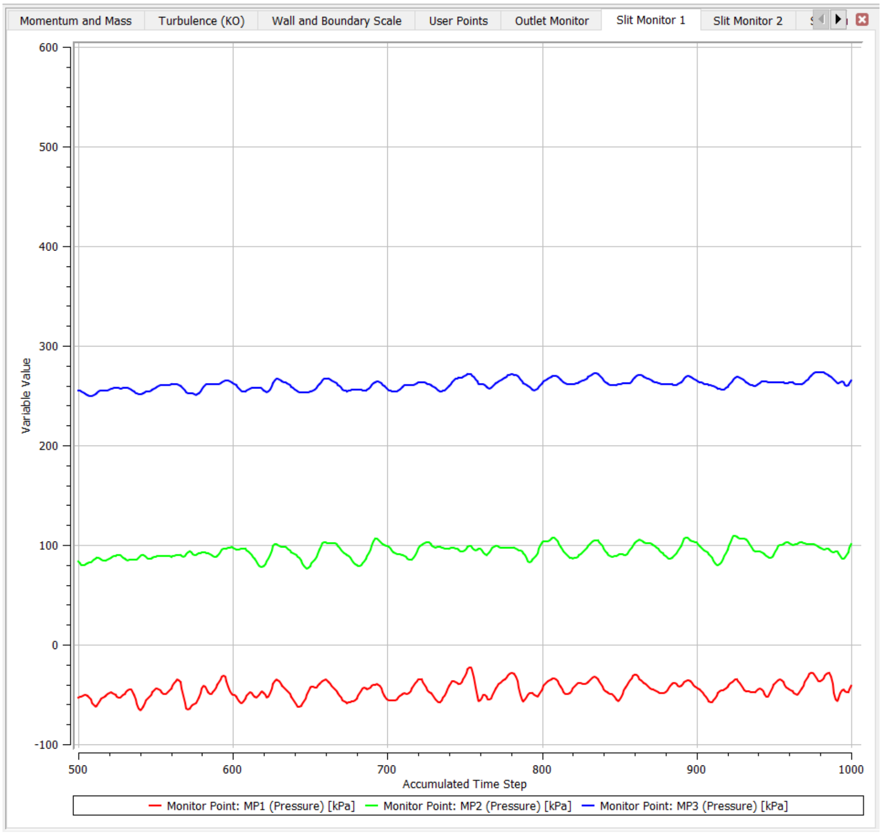

Figure C.58: Slit monitor points 1-3 from steady state initialisation on mesh 4.

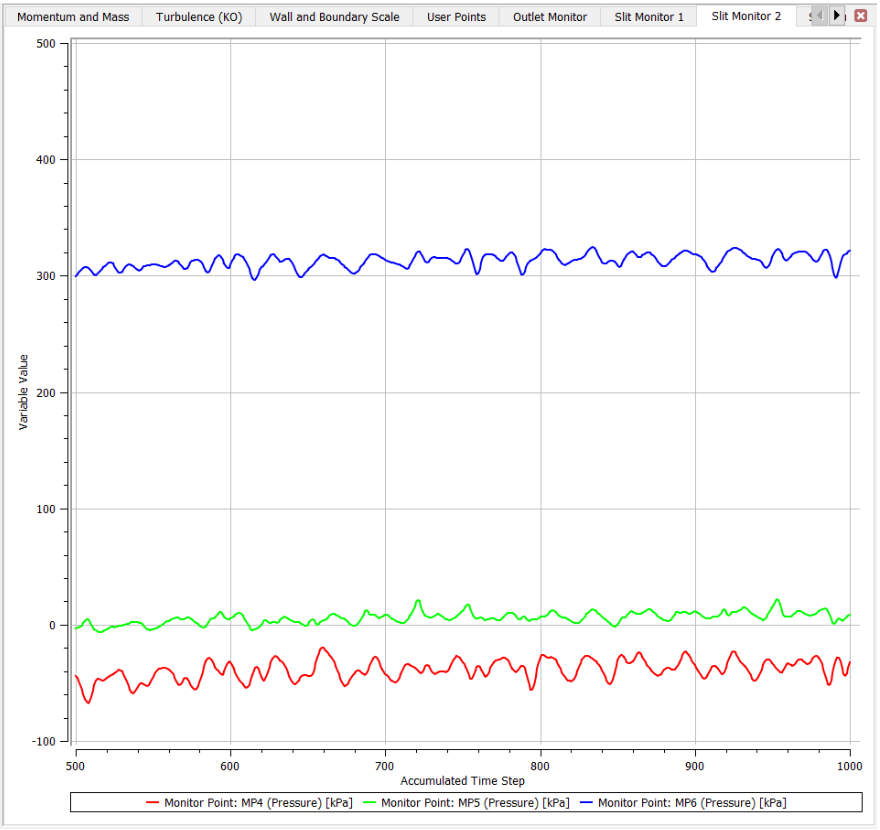

Figure C.59: Slit monitor points 4-6 from steady state initialisation on mesh 4.

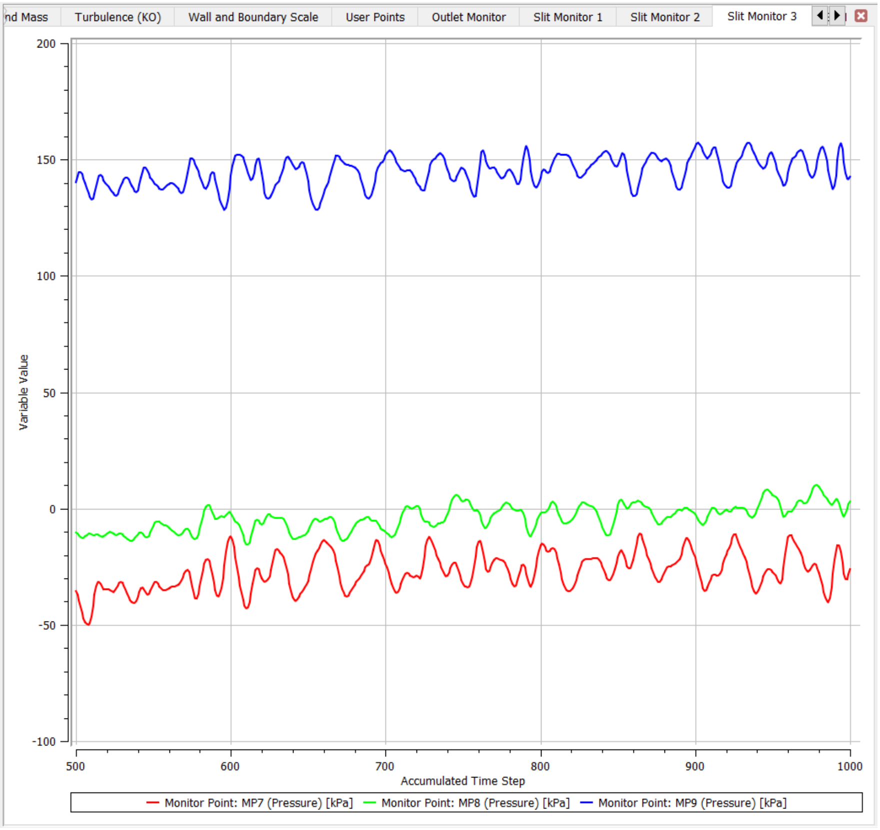

Figure C.60: Slit monitor points 7-9 from steady state initialisation on mesh 4.

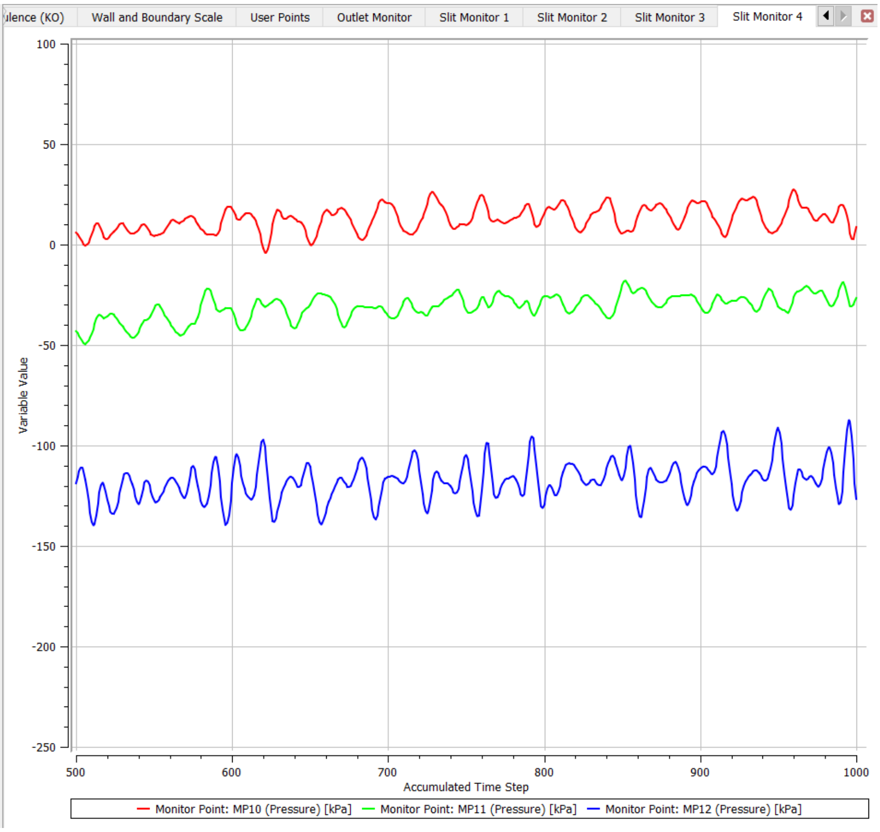

Figure C.61: Slit monitor points 10-12 from steady state initialisation on mesh 4.

C.4.5 Mesh 5

Residuals

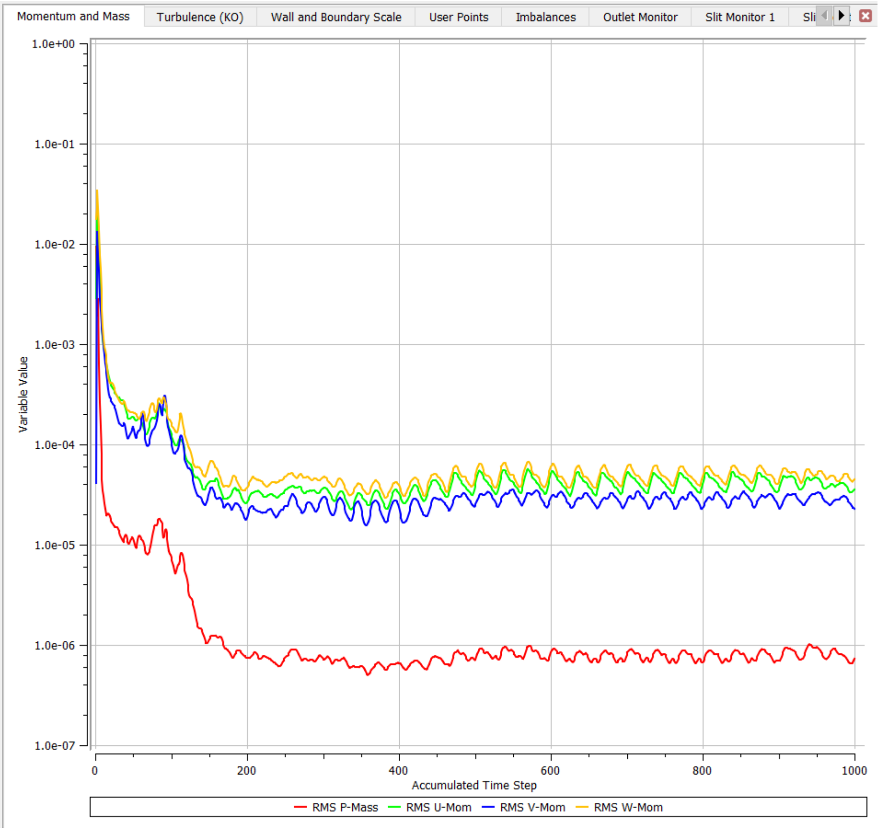

Figure C.62: RMS-residuals from steady state initialisation on mesh 5.

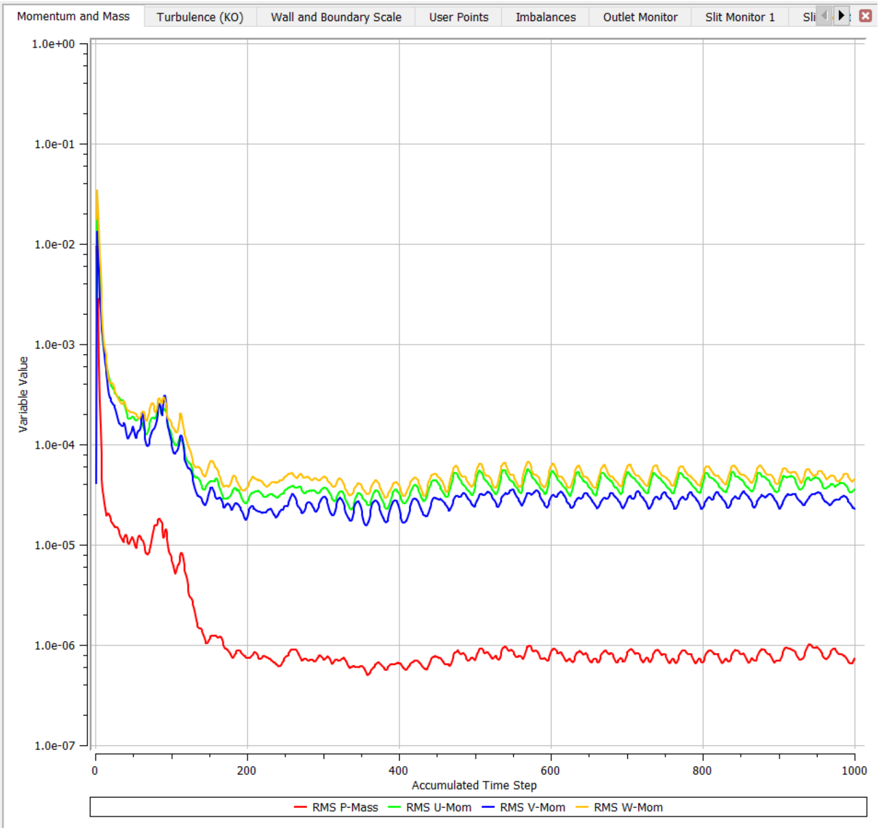

Figure C.63: Max-residuals from steady state initialisation on mesh 5.

Imbalances

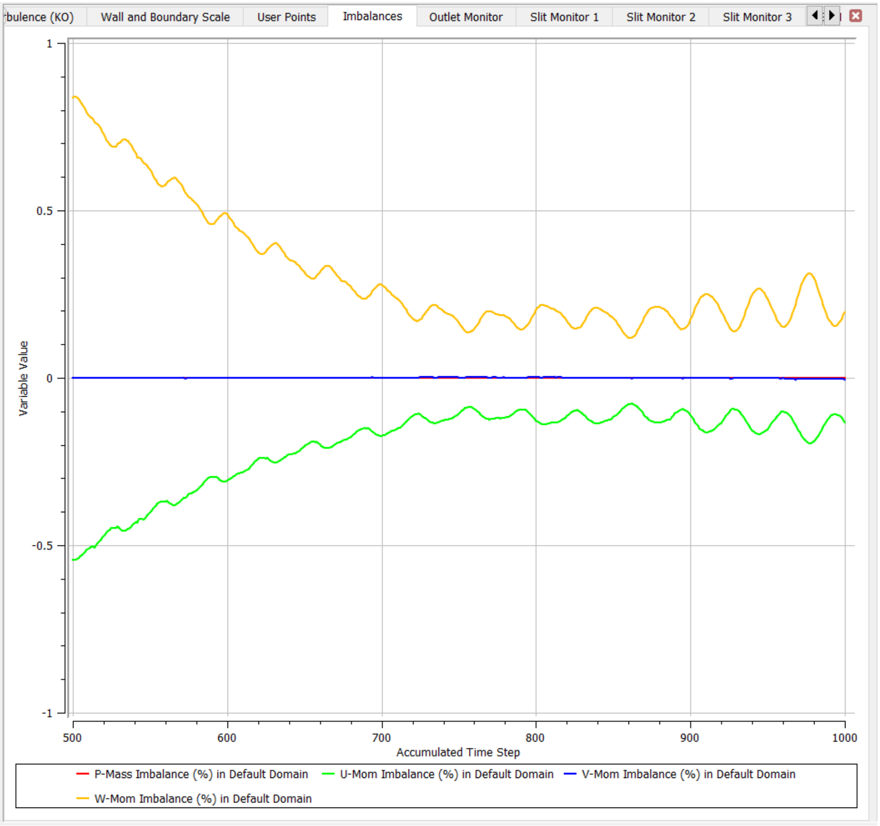

Figure C.64: Imbalances from steady state initialisation on mesh 5.

Monitor Points

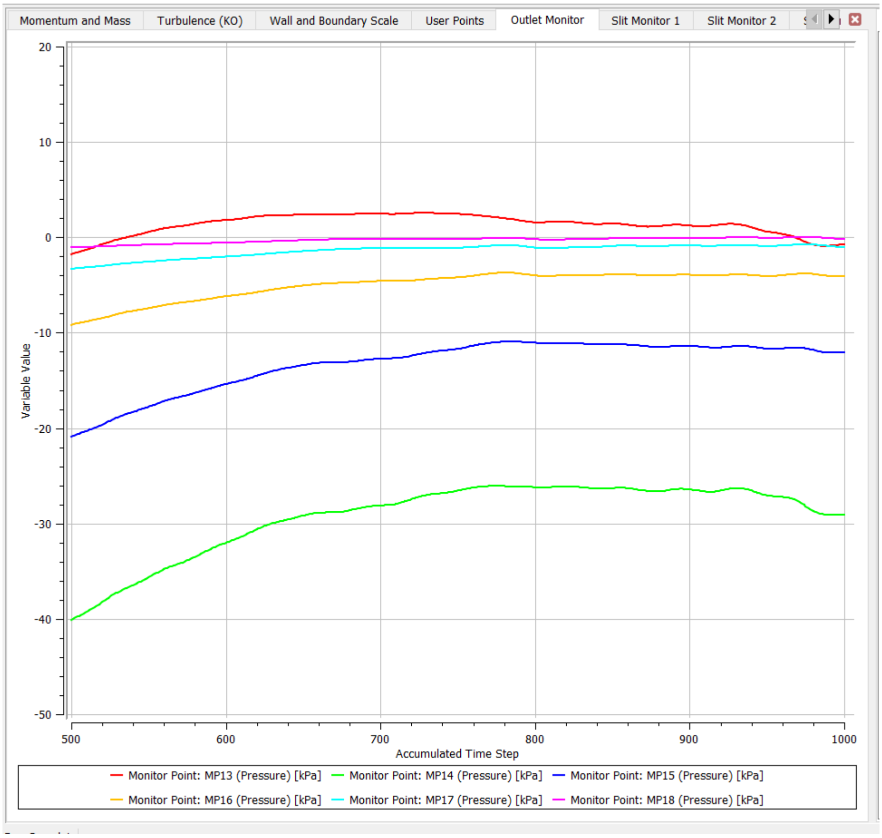

Figure C.65: Outlet monitor points 13-18 from steady state initialisation on mesh 5.

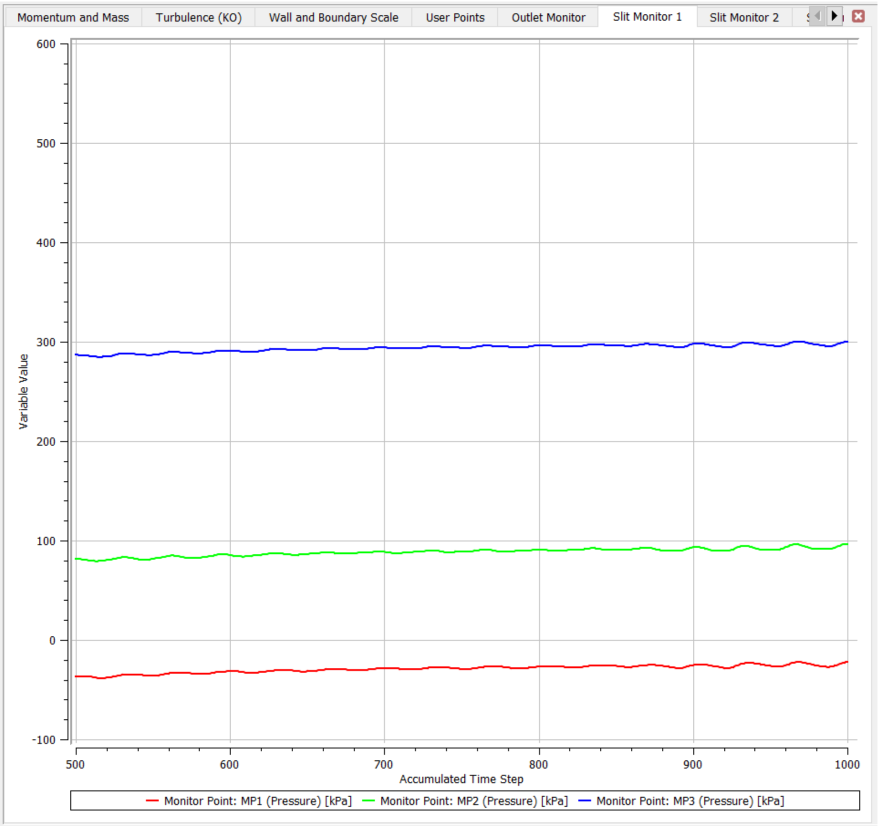

Figure C.66: Slit monitor points 1-3 from steady state initialisation on mesh 5.

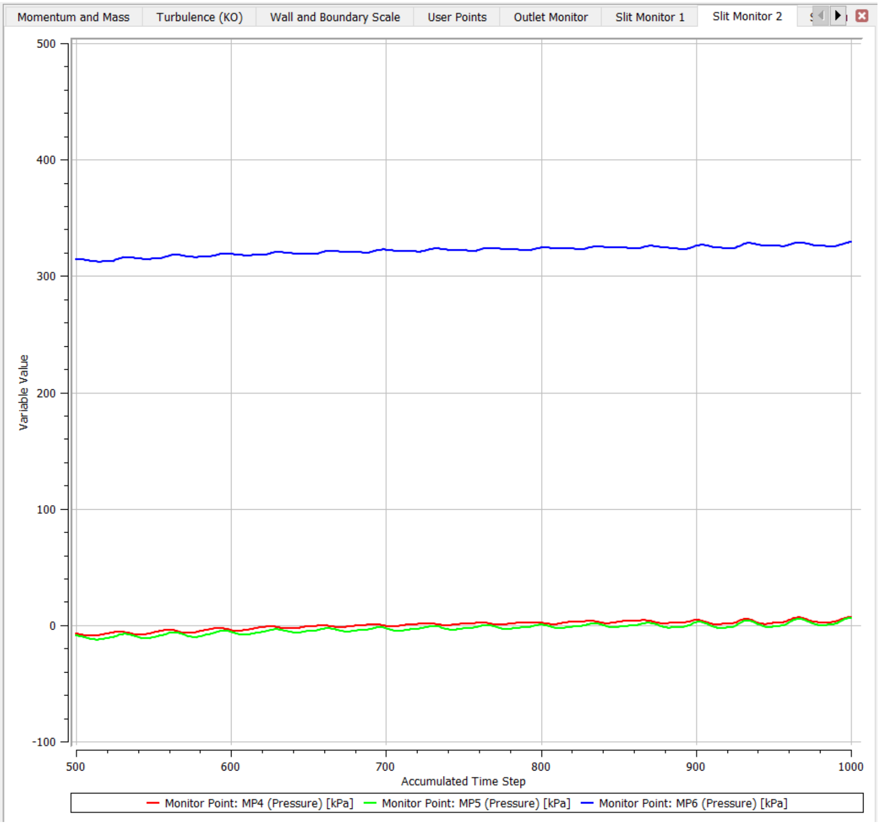

Figure C.67: Slit monitor points 4-6 from steady state initialisation on mesh 5.

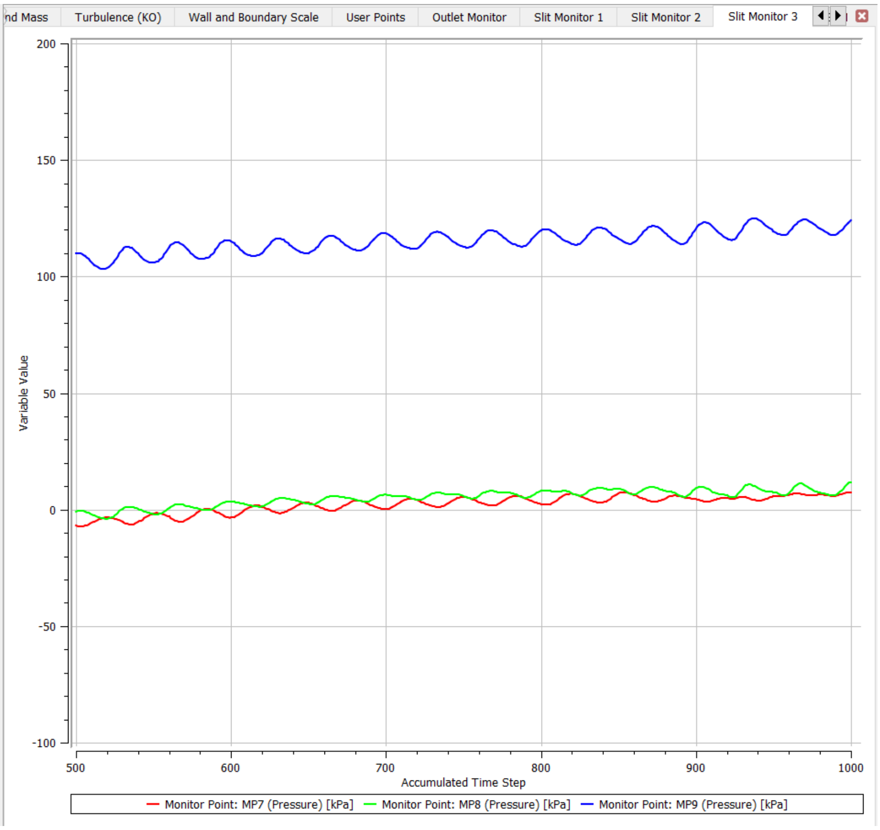

Figure C.68: Slit monitor points 7-9 from steady state initialisation on mesh 5.

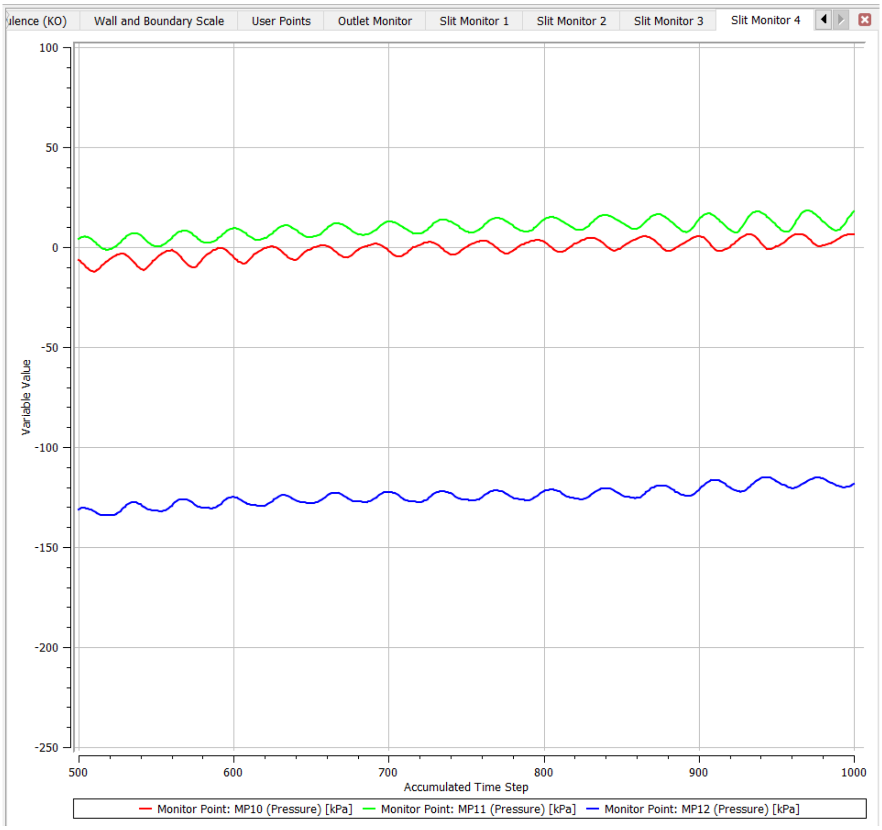

Figure C.69: Slit monitor points 10-12 from steady state initialisation on mesh 5.

C.4.6 Mesh 6

Residuals

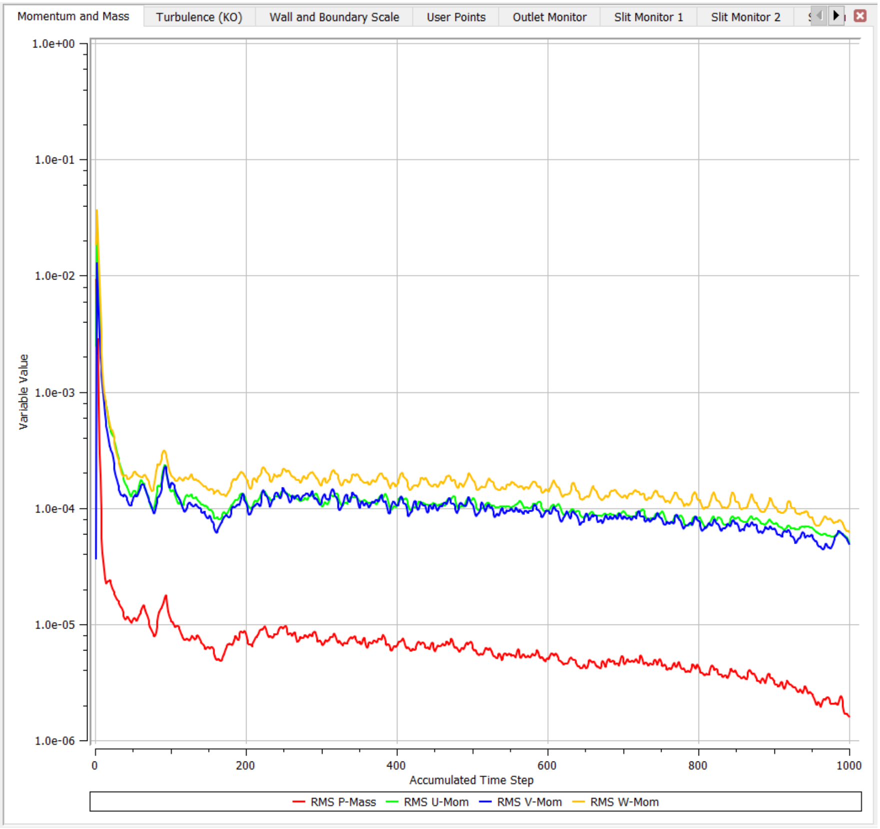

Figure C.70: RMS-residuals from steady state initialisation on mesh 6.

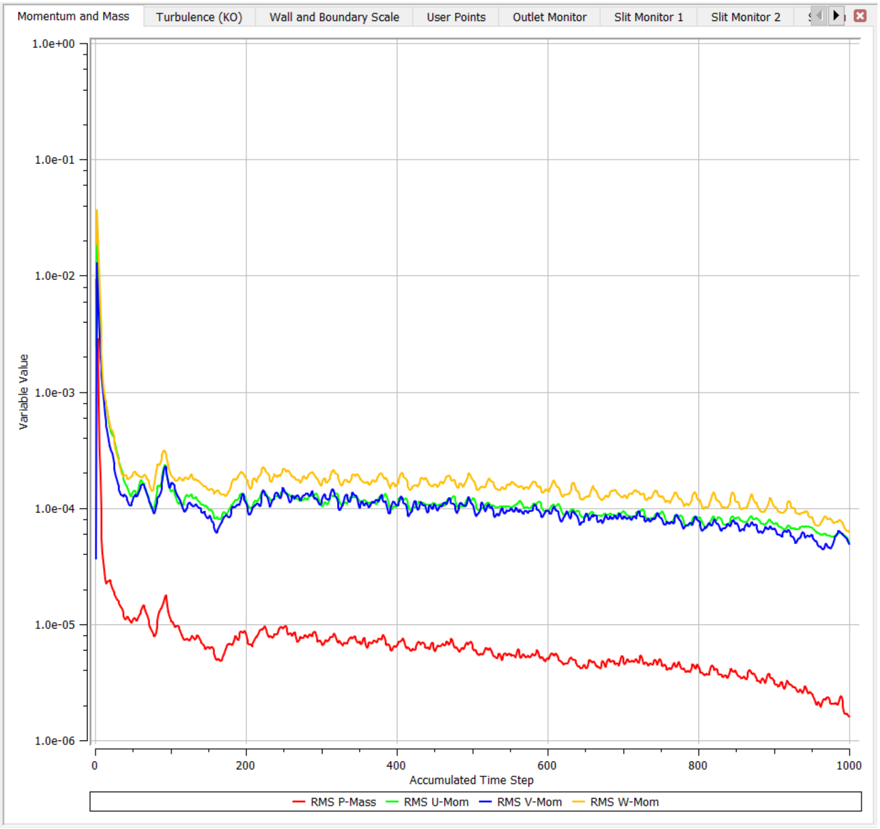

Figure C.71: Max-residuals from steady state initialisation on mesh 6.

Imbalances

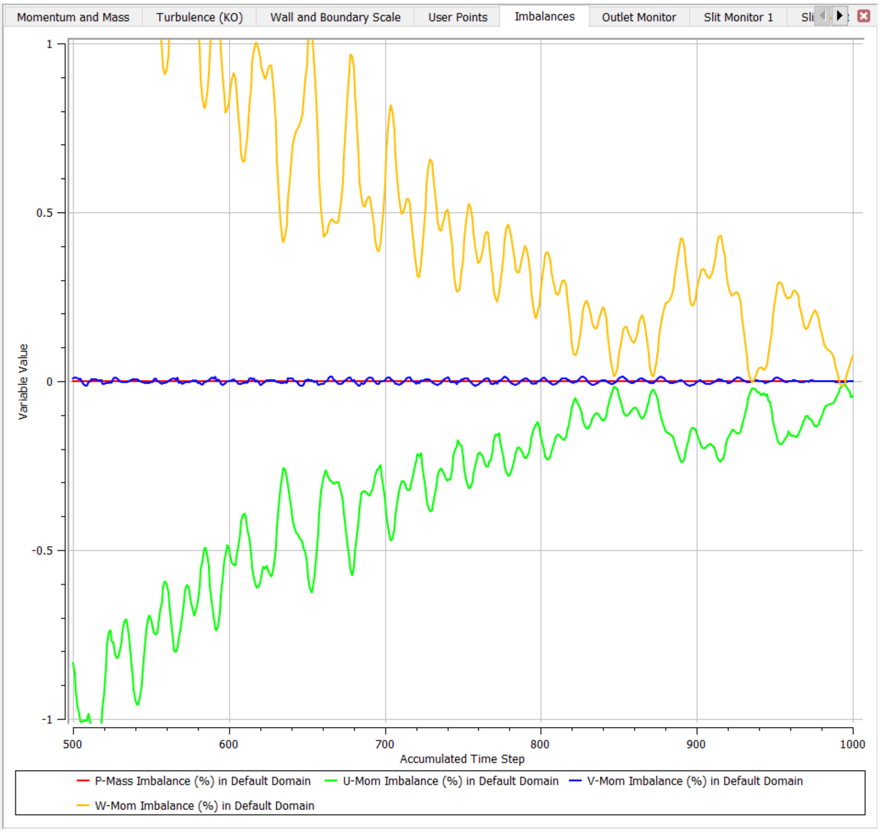

Figure C.72: Imbalances from steady state initialisation on mesh 6.

Monitor Points

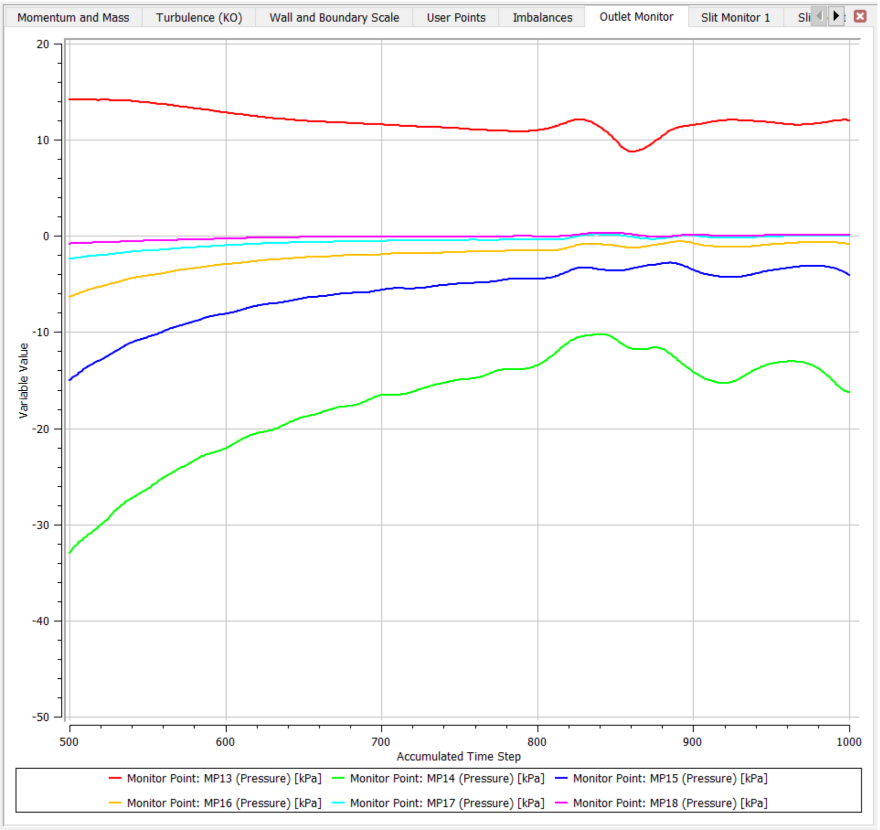

Figure C.73: Outlet monitor points 13-18 from steady state initialisation on mesh 6.

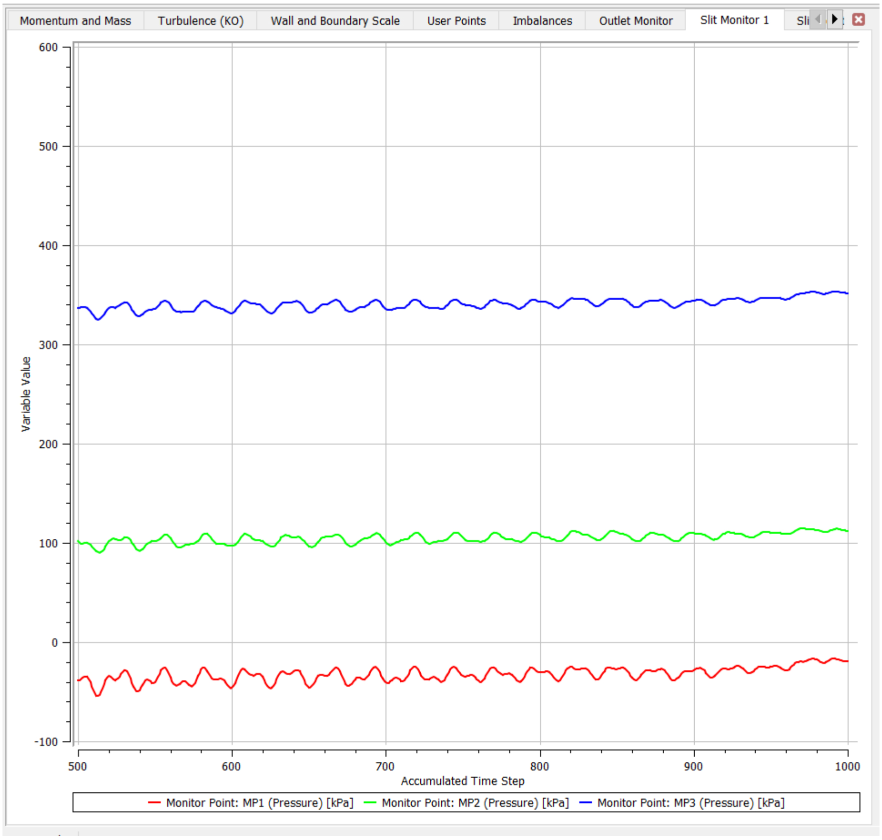

Figure C.74: Slit monitor points 1-3 from steady state initialisation on mesh 6.

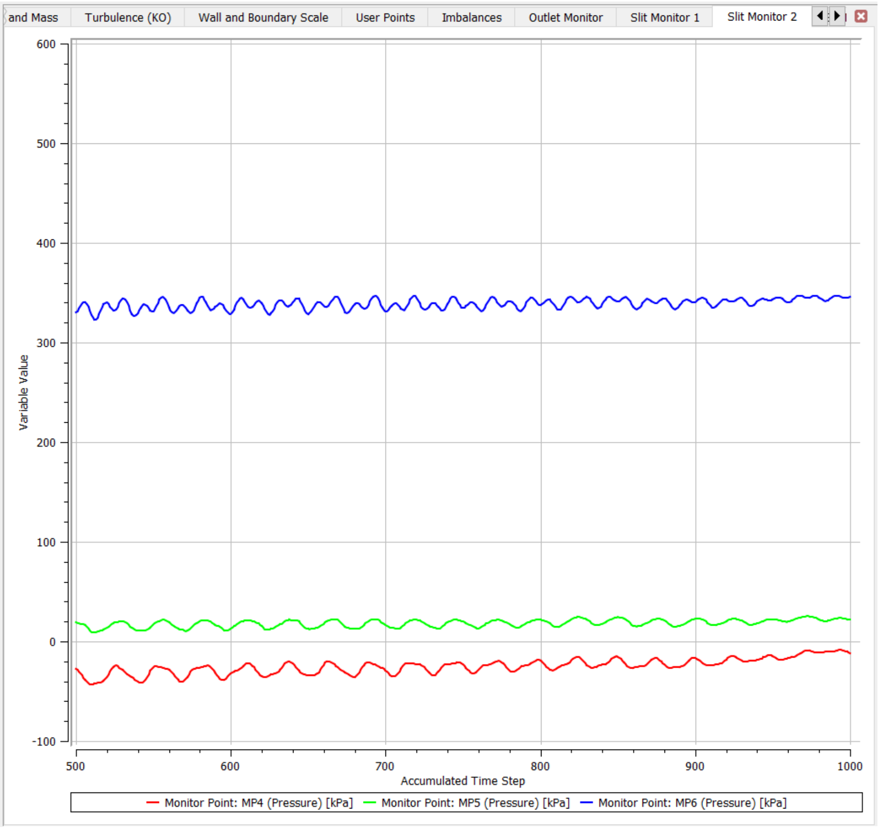

Figure C.75: Slit monitor points 4-6 from steady state initialisation on mesh 6.

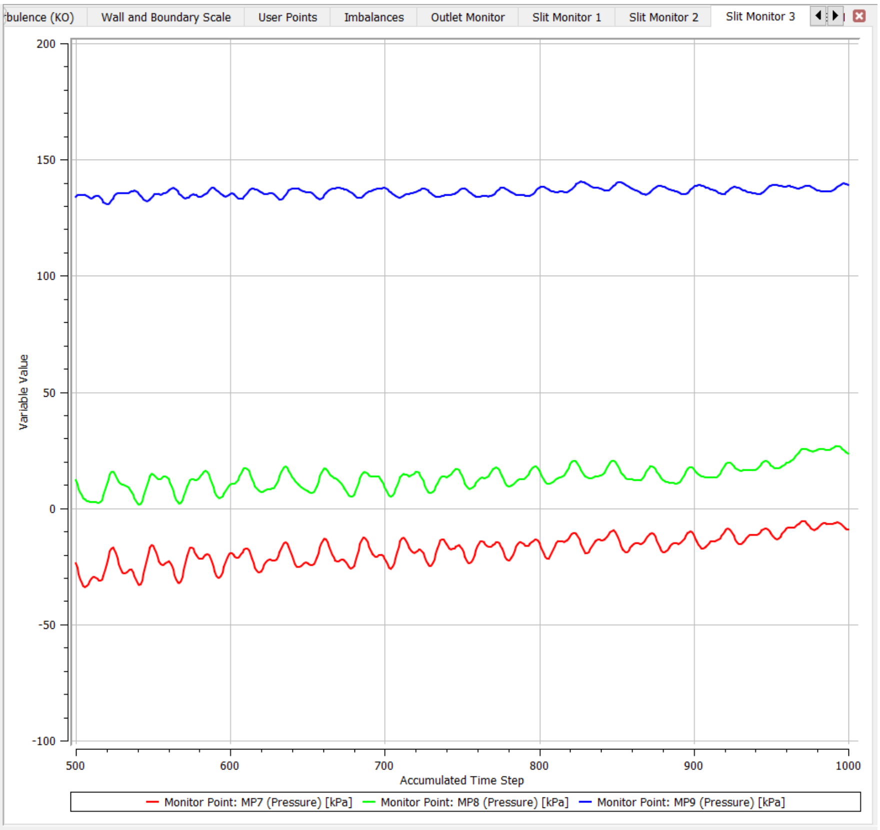

Figure C.76: Slit monitor points 7-9 from steady state initialisation on mesh 6.

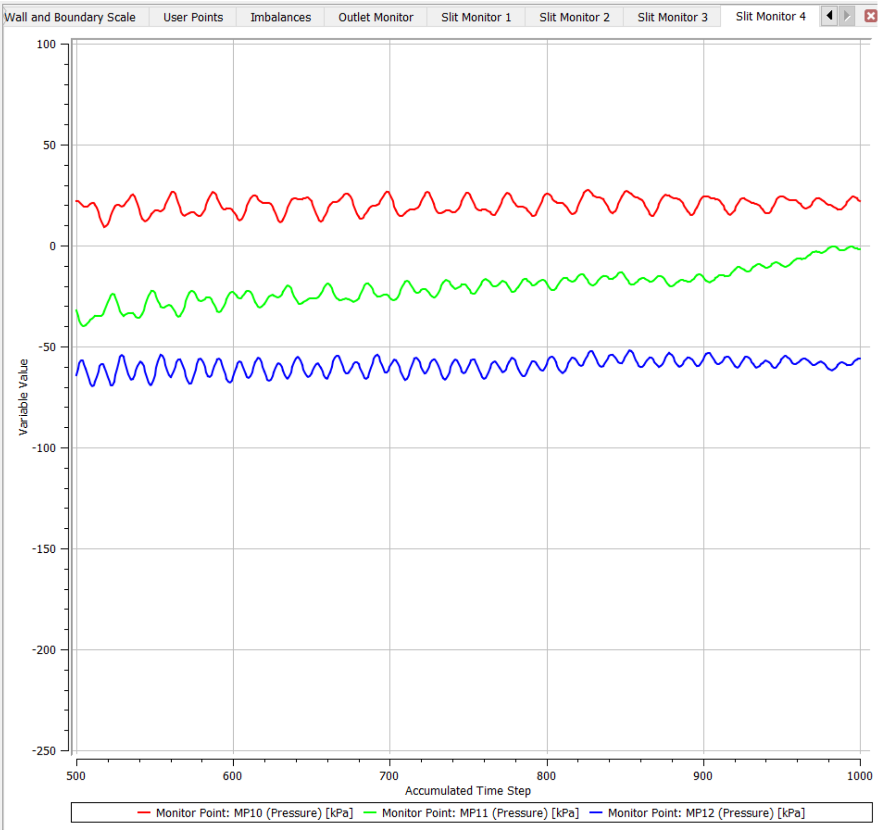

Figure C.77: Slit monitor points 10-12 from steady state initialisation on mesh 6.

C.4.7 Mesh 7

Residuals

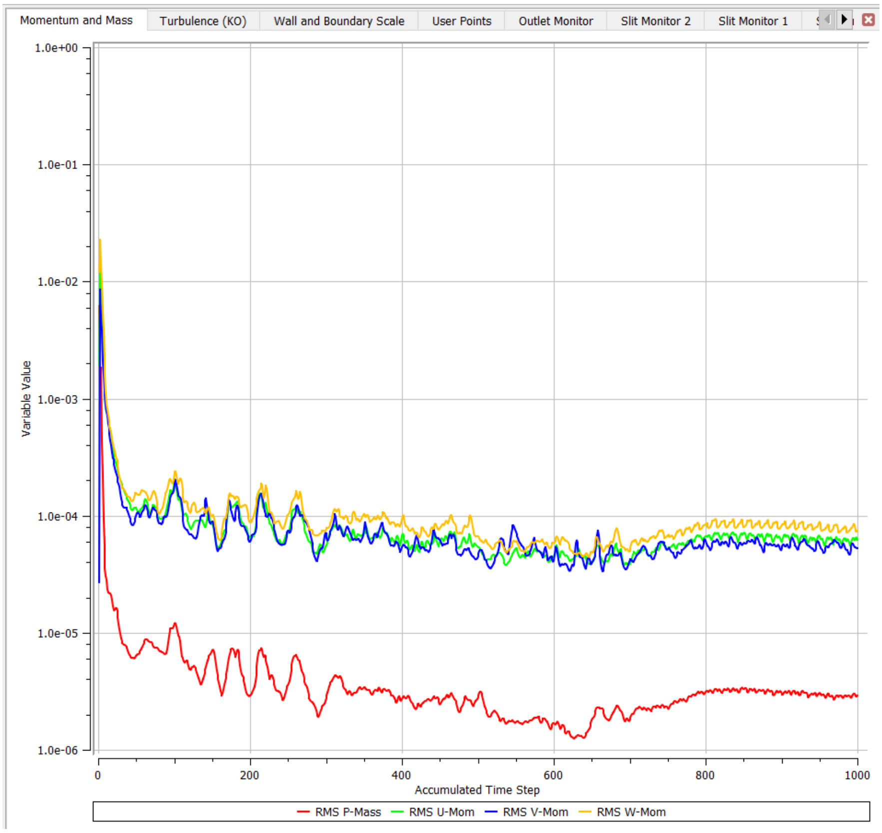

Figure C.78: RMS-residuals from steady state initialisation on mesh 7.

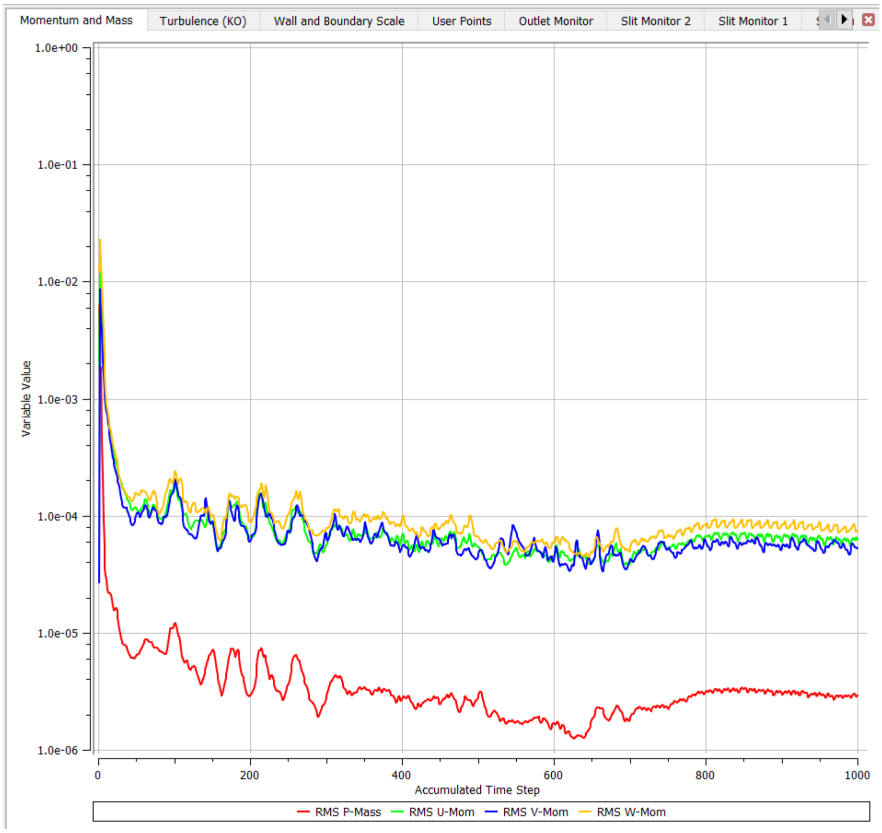

Figure C.79: Max-residuals from steady state initialisation on mesh 7.

Imbalances

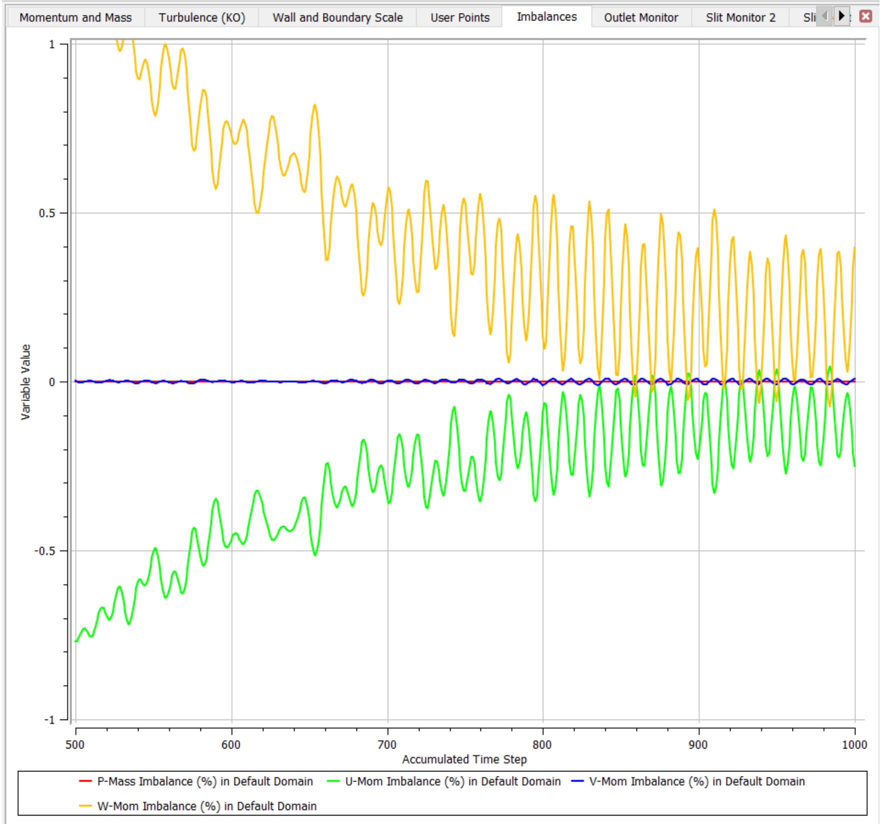

Figure C.80: Imbalances from steady state initialisation on mesh 7.

Monitor Points

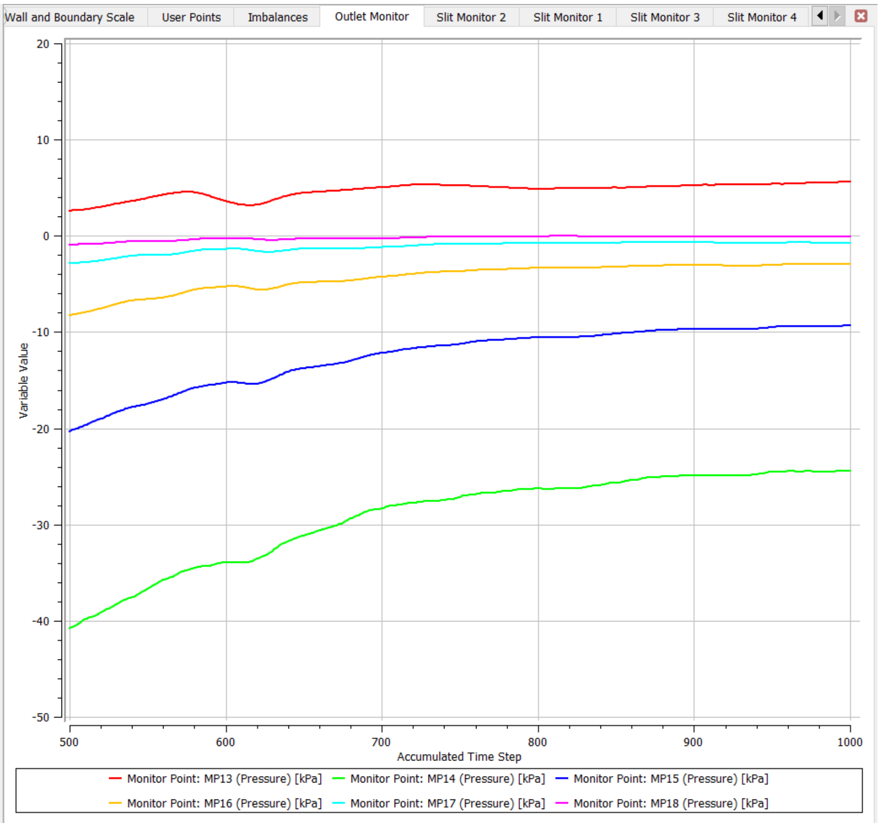

Figure C.81: Outlet monitor points 13-18 from steady state initialisation on mesh 7.

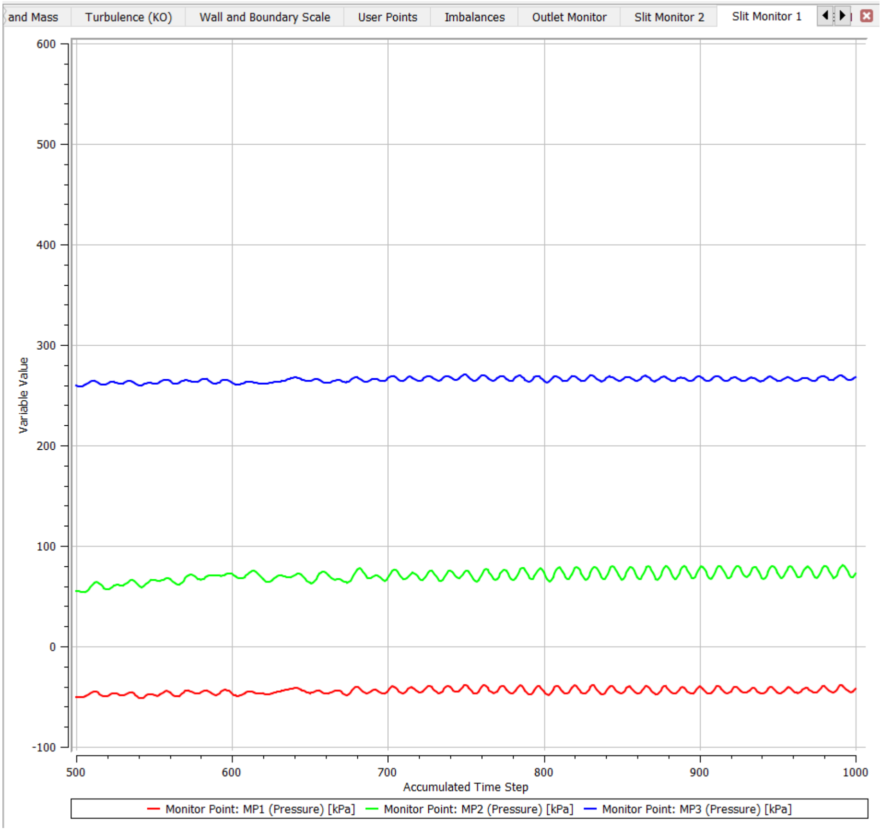

Figure C.82: Slit monitor points 1-3 from steady state initialisation on mesh 7.

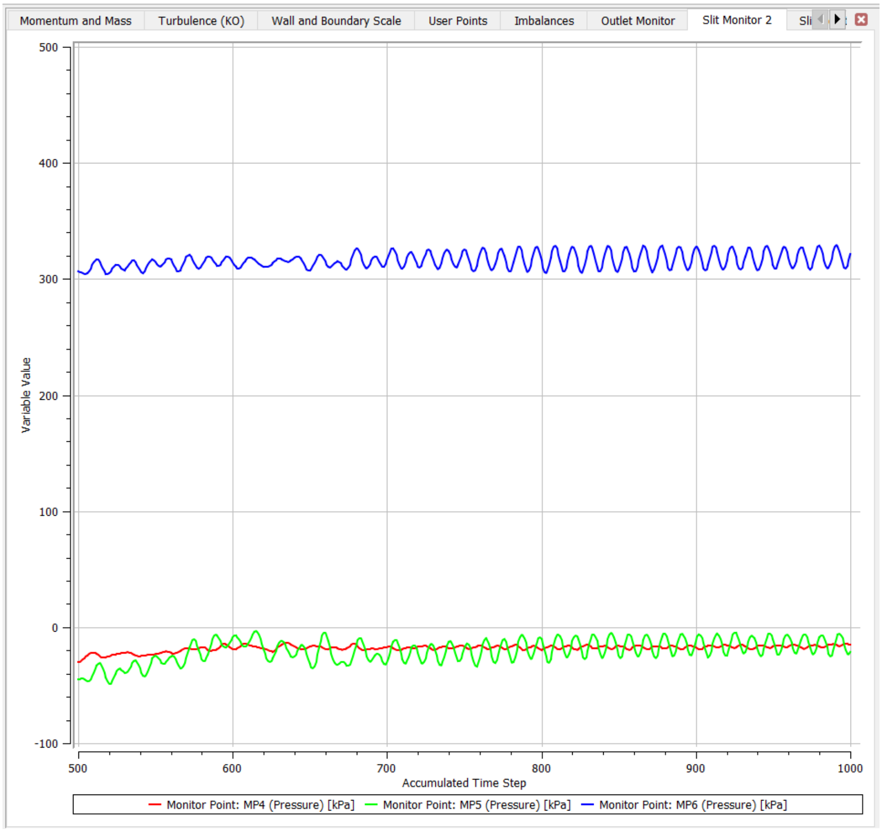

Figure C.83: Slit monitor points 4-6 from steady state initialisation on mesh 7.

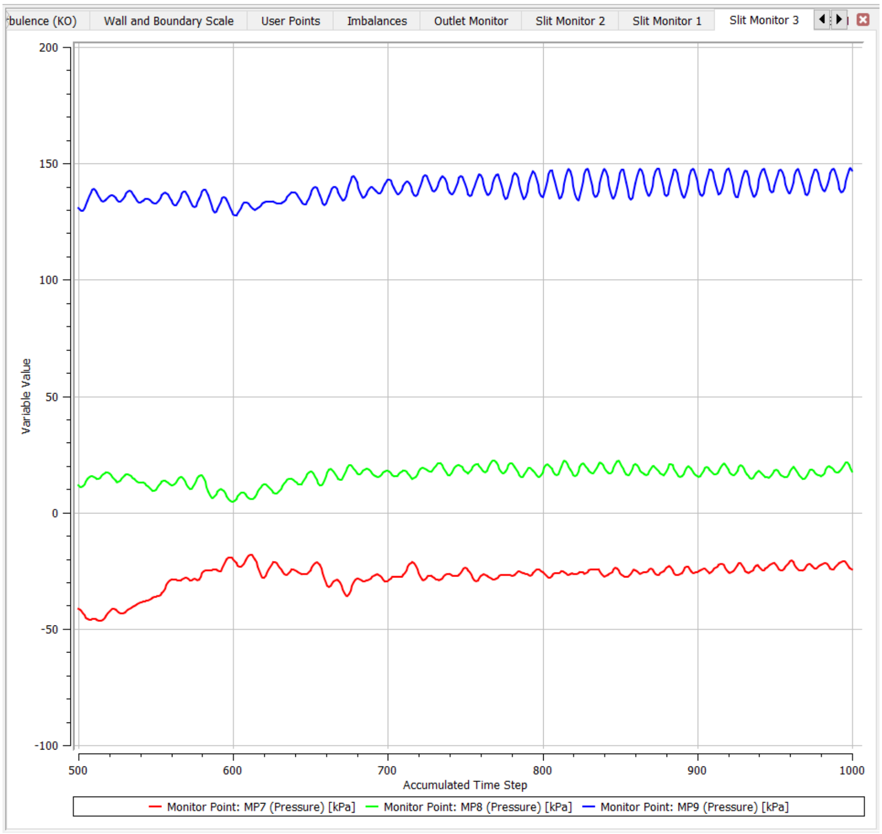

Figure C.84: Slit monitor points 7-9 from steady state initialisation on mesh 7.

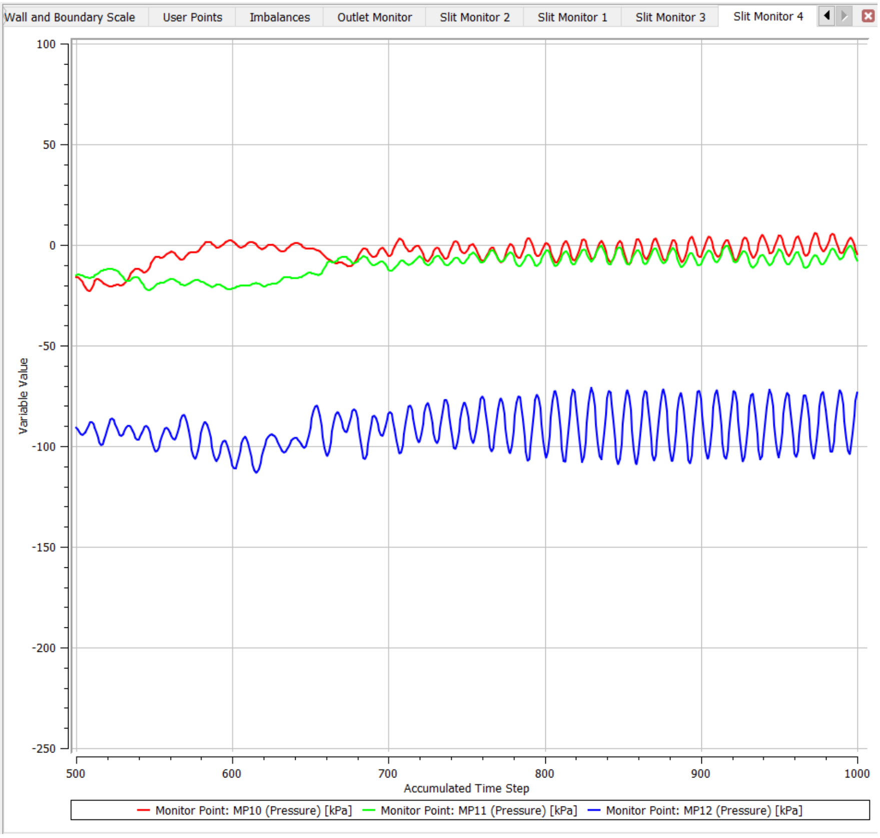

Figure C.85: Slit monitor points 10-12 from steady state initialisation on mesh 7.

C.5 Mesh Quality

Mesh Quality parameters are only presented for Mesh 4 which is used in the simulation. Tet4 is tetrahedral cells, which is used in the free stream of the volume. Hex8 are hexahedral cells with six faces used on the outlet pipe body. Wed6 are cells with five faces which occur in the inflation layer of the region with tetrahedral cells. The subscripts 4,5,6 and 8 represent the number of nodes in the cell. Pyr5 does not appear much in this mesh.

C.5.1 Skewness

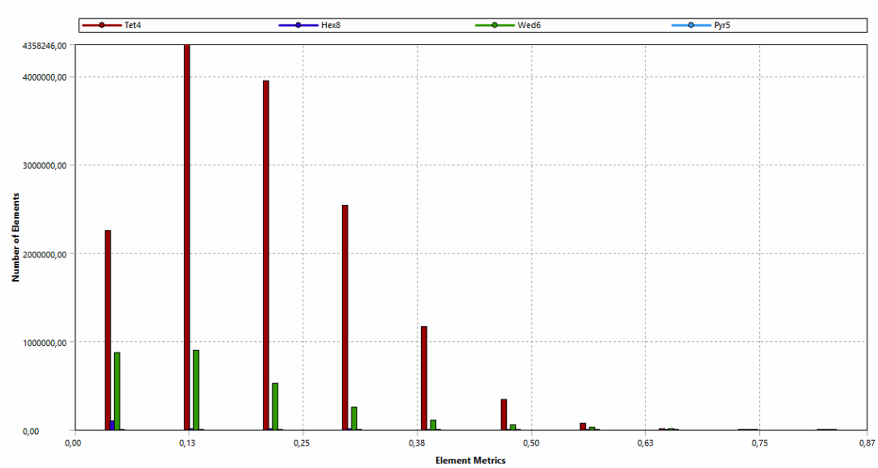

Figure C.86: Skewness values plotted in a bar graph along the x-axis, with number of cells on the y-axis. Data for Mesh 4 measured in ANSYS meshing.

C.5.2 Orthogonal Quality

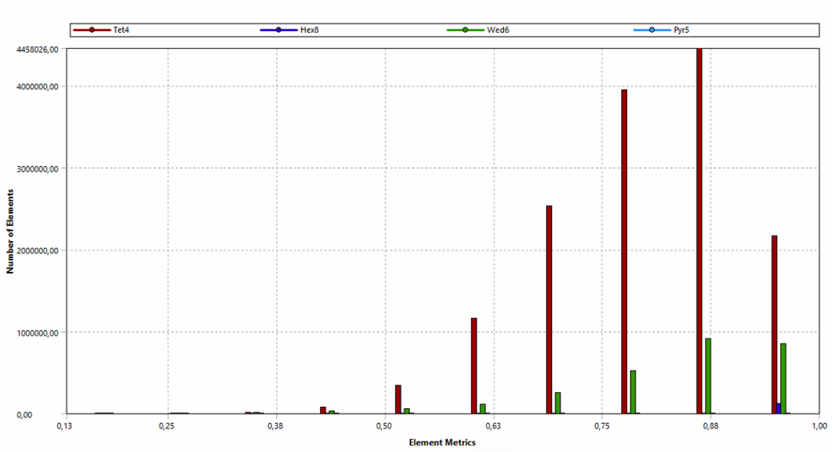

Figure C.87: Orthogonal Quality plotted in a bar graph along the x-axis, with number of cells on the y-axis. Data for Mesh 4 measured in ANSYS meshing.

C.5.3 Aspect Ratio

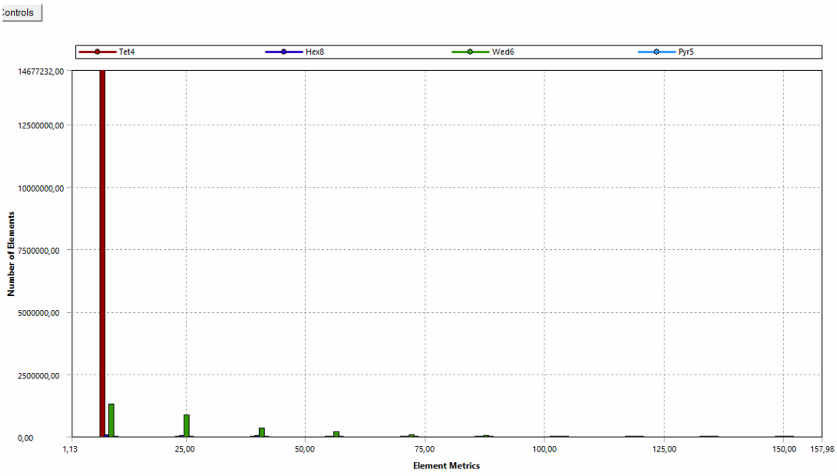

Figure C.88: Aspect Ratio plotted in a bar graph along the x-axis, with number of cells on the y-axis. Data for Mesh 4 measured in ANSYS meshing.

Appendix - D

Measurements from Torpa power plant

D.1 FFT plot

D.1.1 Measurement Point P38

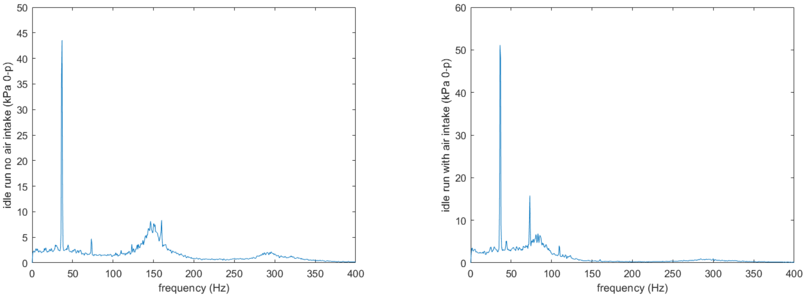

Figure D.1: FFT plots from pressure measurements from P38 on idle runs without and with the use of air intake respectively.

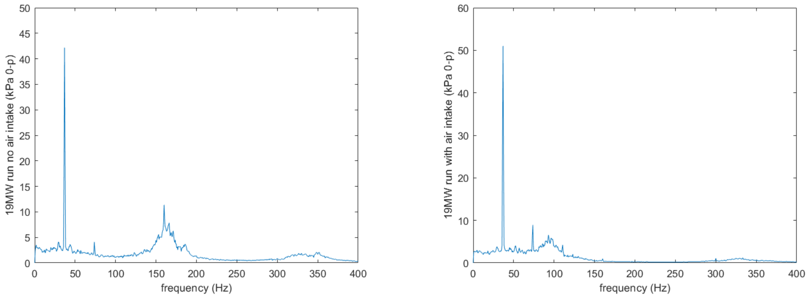

Figure D.2: FFT plots from pressure measurements from P38 on 19MW runs without and with the use of air intake respectively.

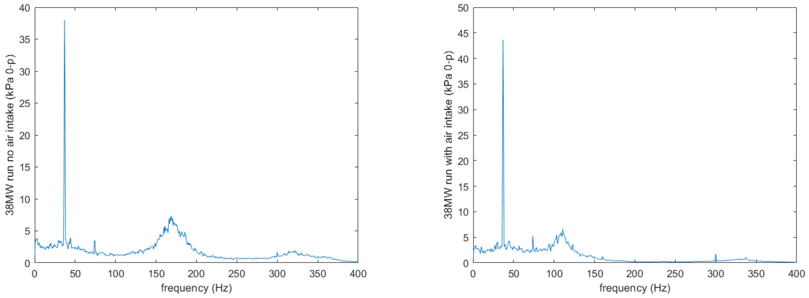

Figure D.3: FFT plots from pressure measurements from P38 on 38MW runs without and with the use of air intake respectively.

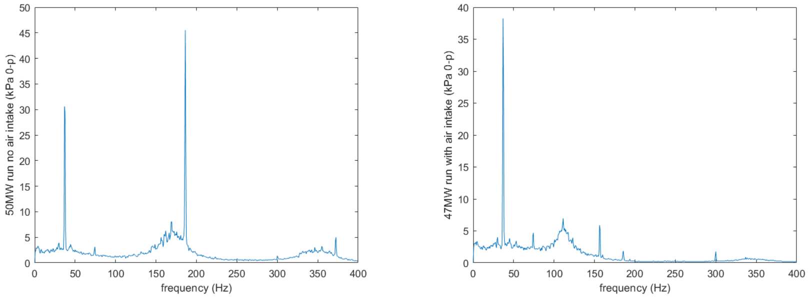

Figure D.4: FFT plots from pressure measurements from P38. From runs on 50 MW without and 47 MW with the use of air intake respectively.

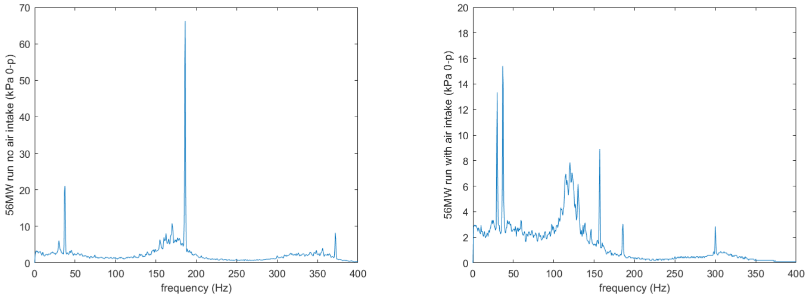

Figure D.5: FFT plots from pressure measurements from P38 on 56MW runs without and with the use of air intake respectively.

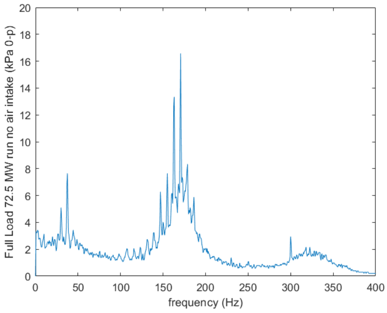

Figure D.6: FFT plots of pressure measurements from P38 on a full load run at 72.5MW without the use of air intake.

D.1.2 Measurement Point P41

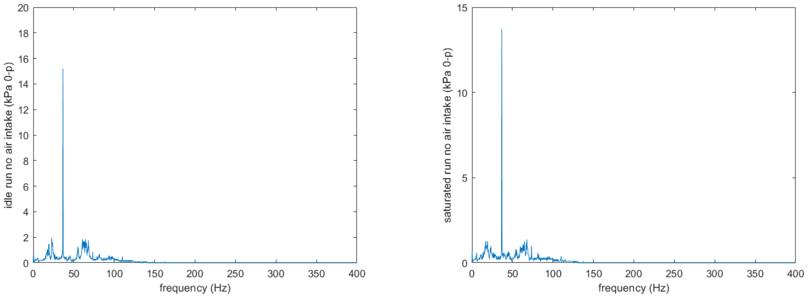

Figure D.7: FFT plots from pressure measurements from P41 on idle and saturated runs respectively without the use of air intake.

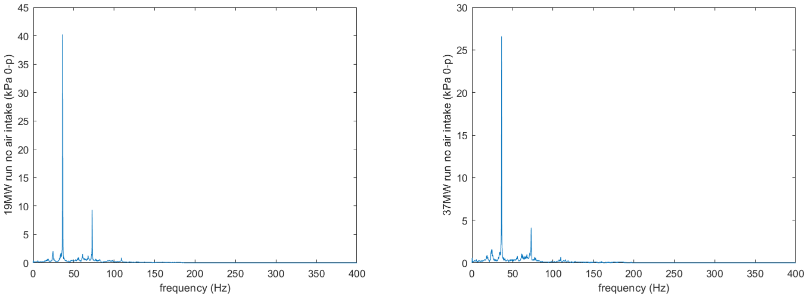

Figure D.8: FFT plots from pressure measurements from P41 on 19MW and 37MW runs respectively without the use of air intake.

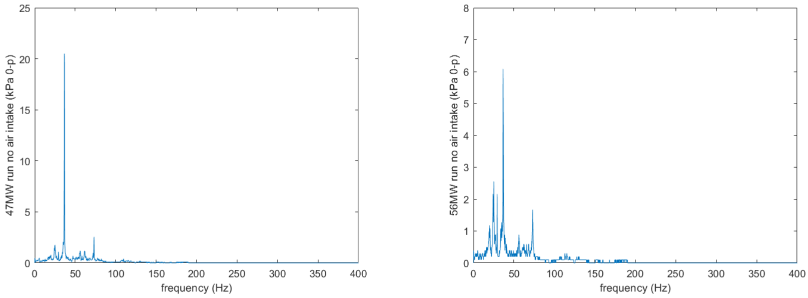

Figure D.9: FFT plots from pressure measurements from P41 on 47MW and 56MW runs respectively without the use of air intake.

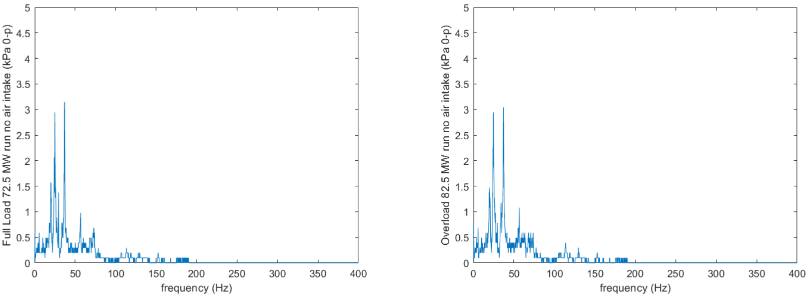

Figure D.10: FFT plots from pressure measurements from P41 on 72MW and 82MW runs respectively without the use of air intake.

Eidsiva Vannkraft AS

Torpa kraftverk
Aggregat 2

Vibrasjonsmåling 2014-01-29

Rapport

2014-03-26 Oppdragsnummer: 5140181

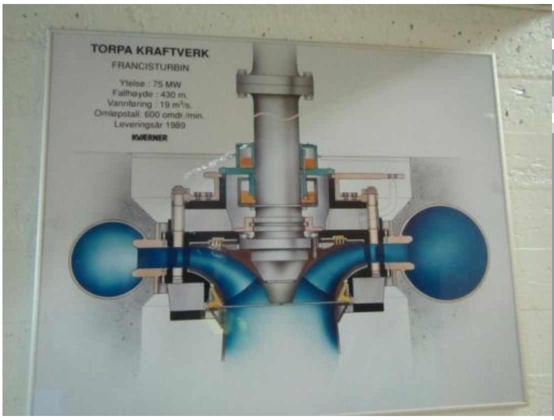

Norconsult

Sammendrag

Oppdrag:	Vibrasjonsmåling med undersøkelse av trykkpulsasjoner
Måledato:	2014-01-29
Forrige måling:	1989-11-22
Måling utført av:	Einar Kobro
Kontakt hos kunde:	Joakim Gundersen

Komponent	Tilstandsvurdering	Karakter
Generator	Tilstanden er tilfredsstillende. Men med tanke på nivåene kombinert med generatorens alder og moderat vibrasjonsnivå ved polpasseringsfrekvensen, bør det planlegges med en grundig generatorinspeksjon i løpet av de nærmeste årene. Dette for å finne om vibrasjonsnivået er en indikasjon på feil under utvikling eller om vibrasjonsnivået er konstruksjonsmessig betinget.	2
Akselstreng/ Lager	Tilstanden er tilfredsstillende. Lageroppretningen er på kanten av det akseptable, og dersom det planlegges stans for utbedring av aggregatet i den nærmeste fremtid bør man samtidig bedre oppretningen.	2
Turbin	Tilstanden er tilfredsstillende. Tilstanden til selve turbinen er god, mens det i spaltevannsarrangementet registreres noe høye trykkpulsasjonsnivåer. Tilstanden er noe bedre enn på Aggregat 1. Ingen tiltak anbefales.	2

Karakterskala: 1. Ingen anmerkninger. 2. Avvik fra nytilstand, men ingen tiltak påkrevet.
3. Planlegge tiltak. 4. Tiltak utføres før videre drift.

0	**2014-03-26**	Rapport	Einar Kobro	Lars Brevig	Einar Kobro
Rev.	Dato	Beskrivelse	Utarbeidet	Fagkontroll	Godkjent

Spaltevanns-arrangement	Tilstanden er tilfredsstillende. Vibrasjonsmålingene med og uten luft på lagerhusene viste ikke tydelige forskjeller. Trykkpulsasjonsnivåene var forskjellige med og uten luftinnslipp, særlig i spaltevannsrøret. Nivået er noe *høyere* på øvre lokk *med* luftinnslipp, men betydelig lavere i spaltevannsrøret når luftinnslipp var på. Trykkbildet på øvre lokk domineres av hydrauliske egenfrekvenser. 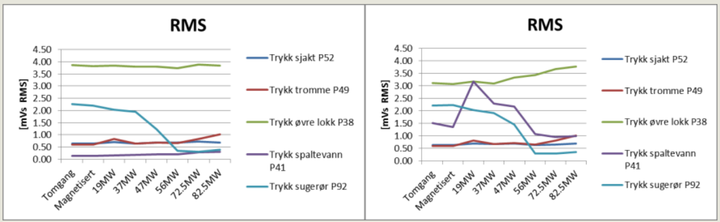 *Trykkpulsasjonsnivå med luftinnslipp (venstre) og uten luftinnslipp (høyre)* Med tanke på levetiden til spaltevannsarrangementet er det viktig at man fortsetter å bruke luftinnslippet.	2

2.4 LASTAVSLAG

Komponent / egenskap	Tilstandsvurdering	Karakter
Turtall	Høyeste registrerte turtall ved 38MW avslag var 665rpm.	-
Trykkstigning	Høyeste målte trykk rett etter avslaget ble målt til 467mvs, mot 455mvs før avslaget. Kombinasjonen av stans av aggregatet samtidig som vannveissvingningene var på topp, medførte det høyeste registrerte trykket (468mvs).	-

3 Anbefalte tiltak

3.1 GENERATOR

Ingen tiltak anbefales nå.

Med tanke på det noe høye vibrasjonsnivået tangentielt i øvre generatorlager, bør det planlegges med en grundig gjennomgang av generatoren i løpet av de nærmeste årene. Denne vil avdekke om den målte amplituden ved polpasseringsfrekvensen er karakteristisk for aggregatet eller en feiltilstand under utvikling.

3.2 AKSELSTRENG / LAGER

Ingen tiltak anbefales nå.

Dersom aggregatet skal demonteres, bør lageroppretting få fokus ved montering av aggregatet.

3.3 TURBIN

Ingen tiltak anbefales.

3.4 LASTAVSLAG

Ingen tiltak anbefales.

A.2 MÅLEOPPSETT

A.2.1 Testprogram

Dato	Klokkeslett	Driftspunkt
28/1-14	1000	Stillstand før
	1023	Oppstart
	1040	Tomgang kald
	1042	Magnetisering
	1044	Magnetisert
	1047	Opplast til full
	1055	Fullast kald
	1154	Fullast varm med luft
	1159	Fullast uten luft
	1203	Overlast uten luft
	1206	Overlast med luft
	1216	56MW med luft
	1218	56MW uten luft
	1224	47MW uten luft
	1226	47MW med luft
	1230	37MW med luft
	1233	37MW uten luft
	1237	19MW uten luft
	1239	19MW med luft
	1243	Tomgang m/spenning m/luft
	1246	Tomgang m/spenning u/luft
	1248	Tomgang u/spenning u/luft
	1251	Tomgang u/spenning m/luft
	1301	38MW Avslag
	1304	Stans
	1321	Stillstand etter

Tabell A. 1 Testprogram

A.2.2 Måleutstyr

Trykk Sjakt og Tromme	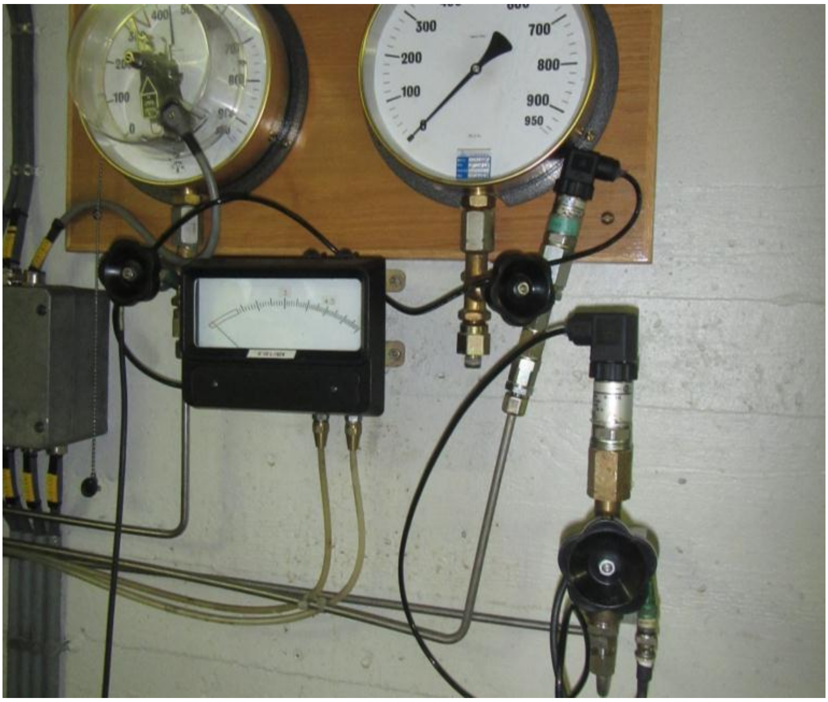
Trykk spaltevann	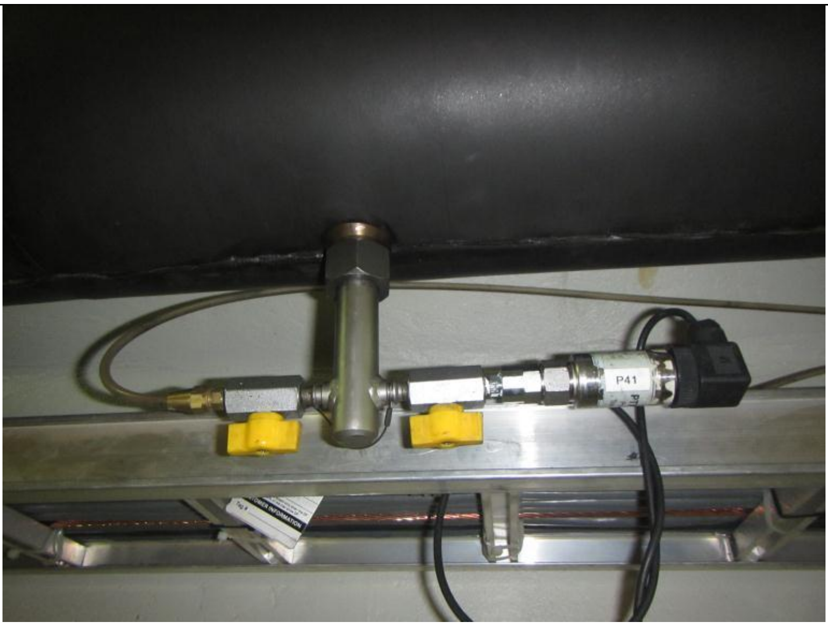

Trykk øvre lokk